# Final Report: Design Investigation of Subsurface Safety Valves for XHPHT

**Document: 07121-1603.FINAL, 3**

# Project Title: Design Investigation of Subsurface Safety Valves for Extreme High Pressure and High Temperature Applications

**Contract Number: 07121-1603c**

**December 13, 2010**

**Principal Investigator: Professor J. Ed Akin, PhD PE**

**Rice University**
**Department of Mechanical Engineering and Materials Science**
**6100 Main Street, MS 321, Houston, TX 77005**
**akin@rice.edu**

## LEGAL NOTICE

**This report was prepared by Rice University as an account of work sponsored by the Research Partnership to Secure Energy for America, RPSEA. Neither RPSEA members of RPSEA, the National Energy Technology Laboratory, the U.S. Department of Energy, nor any person acting on behalf of any of the entities:**

**a. MAKES ANY WARRANTY OR REPRESENTATION, EXPRESS OR IMPLIED WITH RESPECT TO ACCURACY, COMPLETENESS, OR USEFULNESS OF THE INFORMATION CONTAINED IN THIS DOCUMENT, OR THAT THE USE OF ANY INFORMATION, APPARATUS, METHOD, OR PROCESS DISCLOSED IN THIS DOCUMENT MAY NOT INFRINGE PRIVATELY OWNED RIGHTS, OR**

**b. ASSUMES ANY LIABILITY WITH RESPECT TO THE USE OF, OR FOR ANY AND ALL DAMAGES RESULTING FROM THE USE OF, ANY INFORMATION, APPARATUS, METHOD, OR PROCESS DISCLOSED IN THIS DOCUMENT.**

**THIS IS A FINAL REPORT. THE DATA, CALCULATIONS, INFORMATION, CONCLUSIONS, AND/OR RECOMMENDATIONS REPORTED HEREIN ARE THE PROPERTY OF THE U.S. DEPARTMENT OF ENERGY.**

**REFERENCE TO TRADE NAMES OR SPECIFIC COMMERCIAL PRODUCTS, COMMODITIES, OR SERVICES IN THIS REPORT DOES NOT REPRESENT OR CONSTIITUTE AND ENDORSEMENT, RECOMMENDATION, OR FAVORING BY RPSEA OR ITS CONTRACTORS OF THE SPECIFIC COMMERCIAL PRODUCT, COMMODITY, OR SERVICE.**

## ABSTRACT

The Research Partnership to Secure Energy for America (RPSEA), Technical Focus Area 4 – Step-Change Technology sought novel technologies that *may* result in improved ultra-deepwater production systems. Sub-Surface Safety Valves (SSSV) are a technology that must have a step change in capabilities for extreme high pressure, high temperature (XHPHT) discoveries to become safely producible. At the new 30 ksi pressures and high temperatures, say 400 F, an incremental change in current designs will likely not be sufficient. A new approach to the SSSV design process,was completed through a graduate level task design, to help in developing the XHPHT design resources.

This final report presents the results of studying several subjects that influence any SSSV design. The main conclusions were that a "design-by-analysis" approach will be needed for future designs, and that different certified experts will be required for the analysis portion addressing each subject that influences the design. The project team consisted of Professor Ed Akin and two graduate students from the Department of Mechanical Engineering and Materials Science at Rice University.

# Signature

This Final Report was approved by Prof. J. Ed Akin, PhD PE on December 13, 2010.

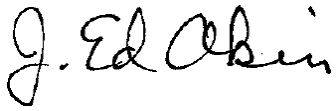

**THIS PAGE INTENTIONALLY LEFT BLANK**

# Contents


Contents 6
List of Figures and Tables 9
Executive Summary 12
Acknowledgement 14
Chapter 1 15
Introduction 15
1.1 Motivation 15
1.2 Report Overview 17
Chapter 2 18
Literature Survey 18
2.1 Beyond Current SSSV Design Standards 18
2.2 ASME Boiler and Pressure Vessel Codes 19
2.3 Failures of Ball Shaped Safety Valves 20
2.4 Current Flapper Valve Technology 21
2.4.1 Operation Mechanism and Life Expectancy 23
2.4.2 Curved-Flapper Design 23
2.4.3 Pressure Self-Equalizing Technology 24
2.4.4 Floating Magnetic Coupler 25
2.5 Investigation on High Strength Materials 26
2.6 Materials Survey Summary 28
Chapter 3 30
Computational Fluid Dynamics 30
3.1 CFD Analysis with ANSYS® CFX v12.0 30
3.1.1 XHPHT Production Fluid Properties 31
3.1.2 Pipeline Hydraulics 32
3.1.3 Shear Stress Transport $\mathbf{k-\omega}$ Turbulence Model 36
3.2 Quasi-Static Fluid Structure Interaction 37
3.2.1 Fluid Domains 38
3.2.2 Spacing and Inflated Boundaries 40
3.2.3 CFD Mesh Facts 41
3.2.4 Results for Flapper Opening Procedure 42

3.3 CFD Analysis of Pressure Self-Equalizing SSSV 47
3.3.1 Fluid Domains 47
3.3.2 Boundary Conditions 47
3.3.3 Mesh Facts 48
3.3.4 Results for Pressure Self-Equalizing Mechanism 50
Chapter 4 51
Water Hammer Analysis 51
4.1 Problem Description 51
4.2 One-Dimensional Water-Hammer Analysis 51
4.3 Water Hammer Results and Discussion 53
Chapter 5 55
Finite Element Stress Analysis 55
5.1 Commercial Software Tools 55
5.2 Linear Elastic Contact Analysis in Ansys® Workbench v12.0 56
5.2.1 FEM Pre-processing 56
(1) Importing Geometry 56
(2) Contact Settings 57
(3) Element Types and Mesh Results 58
(4) Material Selection 60
(5) Static Stress Boundary Conditions 60
(6) Pressure Loadings 60

5.2.2 Pressure Loading Results and Discussion 63
(1) Results for Reopening Process 63
(2) Results for Fully-Closed Situation 67
(3) Contact Analysis Discussion 68
5.3 Parametric Study in SolidWorks 2009 68
5.3.1 Estimation of Impact Angular Acceleration and Velocity 68
5.3.2 FEM Preprocessing for Impact Analysis 70
(1) Geometry and Mesh 70
(2) Boundary Conditions 71
(3) Material Properties 72
(4) Slam Loadings 73
5.3.3 Definition of Key Parametric Dimensions 73

5.3.4 Parametric Study Results 74
5.4 Modified Flapper Results and Discussion 79
Chapter 6 81
Low Cycle Fatigue 81
6.1 Problem Definition 81
6.2 Cyclic Strain History by FEA 81
2.1 Preprocessing and Mesh Facts 82
6.2.2 Material Selection 83
6.2.3 LCF Results and Discussion 83
6.2.4 LCF Analysis by Continuum Damage Mechanics Model 85
6.2.5 LCF Analysis by Strain-life Fatigue Model 90
6.3 LCF Conclusion and Discussions 91
Chapter 7 93
Thermal Stress Analysis 93
7.1 Geometry and Assumptions 93
7.2Material Properties and Thermal Boundary Conditions 94
7.2.1 Material 94
7.2.2 Boundary Conditions 94
7.3 Thermal Results 96
7.3.1 Temperature Results 96
7.3.2 Effective Stress Results 97
7.4 Thermal Study Conclusions 99
Chapter 8 100
Study Conclusions and Recommendations 100
References 104
Appendix – Flapper SSSV Prototype Geometry 107

# List of Figures and Tables

Figure 1.1 Recent oil and gas discoveries in the Gulf of Mexico ..... 15
Figure 2.1 Erosion of Ball and Seat by Drilling Fluid (Bourgoyone 2002) ..... 21
Figure 2.2 Typical SCSSV designs [5] ..... 22
Figure 2.3 Baker Oil Tools Slimline curved flapper design (Baker Oil Tools 2001) ..... 24
Figure 2.4 Baker Oil Tools self-equalizing system (Baker Oil Tools 2009) ..... 25
Figure 2.5 Magnetic-coupler Depth-Star TRSV Halliburton [14] ..... 26

Figure 3.1 CFD flow chart ..... 30
Figure 3.2 Power-law velocity profile as inlet boundary conditions ..... 36
Figure 3.3 Definition of a 35° opening angle ..... 39
Figure 3.4 Basic fluid domain (25 degree open) ..... 39
Figure 3.5 Regions definition (25 degrees open) ..... 40
Figure 3.6 Flapper surface mesh control with constant size of 0.08 in (25 degrees open) ..... 41
Figure 3.7 Inflation prisms seen at the inlet surface (25 degrees open) ..... 42
Figure 3.8 Mesh results for 25-Degree open case ..... 43
Figure 3.9 Pressure contour on up and downstream face for reservoir at 10,000 ft for open angles of 5 through 87 degree ..... 45
Figure 3.10 Area integral of pressure across the surfaces of the flapper ..... 46
Figure 3.11 Fluid domain for a pressure equalizing flapper ..... 48
Figure 3.12 Mesh facts for pressure equalizing passage diameter of 0.25cm ..... 49

Figure 5.1 Imported half geometry model of flapper assembly (15-Degree Open) ..... 56
Figure 5.2 SOLID187 and CONTA174 element illustrations ..... 58
Figure 5.3 Mesh facts of 15-Degree open case ..... 59
Figure 5.4 Mesh facts of fully closed case ..... 59
Figure 5.5 Fixed boundary conditions (35 degree open) ..... 60
Figure 5.6 Symmetric boundary conditions (35 degree open) ..... 61
Figure 5.7 CFX pressure mapping on the flapper (35 degree open) ..... 61
Figure 5.8 CFX pressure mapping on the sleeve tube (fully open) ..... 62
Figure 5.9 Stress and strain plot for different opening angles (Inconel® 718) ..... 64
Figure 5.10 Displacement contour of flapper at fully-closed position ..... 67
Figure 5.11 Flapper valve at 5,000 ft for various reservoir depth ..... 67
Figure 5.12 Free body diagram sketch of a flapper SSSV ..... 69
Figure 5.13 Acceleration extrapolation from quasi-static FSI analysis ..... 70
Figure 5.14 A full flapper geometry and its half size mesh results ..... 71
Figure 5.15 boundary locations of a half flapper model ..... 71
Figure 5.16 Cyclic stress-strin curve of Inconel 718 ..... 72
Figure 5.17 Centrifugal force settings in Solidworks 2009 ..... 73
Figure 5.18 Ups_flap location ..... 74
Figure 5.19 Germetric parameters defined for the parametric study ..... 74
Figure 5.20 Total equivalent strain, plastic strain vs. flapper thickness ..... 75
Figure 5.21 Equivalent stress, stress intensity vs. flapper thickness ..... 75
Figure 5.22 Total equivalent strain, plastic strain vs. flapper inner radius ..... 76

Figure 5.23 Equivalent stress, stress intensity vs. flapper inner radius ..... 76
Figure 5.24 Total equivalent strain, plastic strain vs. flapper outer radius ..... 77
Figure 5.25 Equivalent stress, stress intensity vs. flapper outer radius ..... 77
Figure 5.26 Resultant force on the pin hole of the flapper vs. flapper thickness..... 78
Figure 5.27 Minimum pin diameter vs. flapper thickness ..... 79
Figure 5.28 Stress contour plots for a parametric optimized flapper..... 80

Figure 6.1 Solid mesh for a flapper SSSV ..... 82
Figure 6.2 Equivalent Strain and stress of flapper at closure ..... 83
Figure 6.3 Equivalent Strain of flapper at 35 degree open ..... 84
Figure 6.4 Equivalent strain history of the flapper at various opening angles ..... 85
Figure 6.5 Tensile curve for Inconel 718..... 86
Figure 6.6 Elasto-perfect plastic model for Inconel 718..... 87
Figure 6.7 Accumulated plastic strain and damage vs. cycles..... 88
Figure 6.8 Equivalent and damage equivalent stress vs. cycles ..... 89
Figure 6.9 Strain-life curve of Inconel 718..... 91

Figure 7.1 CAD of a flapper SSSV (mid-plane section view)..... 93
Figure 7.2 A pocket structured chamber for a flapper valve ..... 94
Figure 7.3 Boundary conditions (mid-plane section view)..... 95
Figure 7.4 Boundary conditions (mid-plane section view)..... 97
Figure 7.5 Stress contours of a opened SSSV..... 98
Figure 7.6 Stress contours of a opened SSSV with different pocket structures ..... 98

Figure 8.1 Suggested design-by-analysis process for XHPHT components…….**102**

Table 2.1 Material properties of Aermet..... 27
Table 2.2 Material properties of Hastelloy ..... 27
Table 2.3 Material properties of Inconel..... 27
Table 2.4 Material properties of Duplex stainless steel [18] ..... 28
Table 2.5 Material properties of Titanium alloys [18]..... 28
Table 3.1 RPSEA suggested extreme HP/HT fluid properties ..... 32
Table 3.2 Critical average velocity ..... 33
Table 3.3 Average velocity, Re and friction number estimations..... 34
Table 3.4 Power-law velocity profile in terms of n and maximum velocity ..... 36
Table 3.5 Quasi-static FSI CFD mesh results..... 42
Table 3.6 Maximum value of flapper pressure (psi) - reservoir at 10,000 ft..... 44
Table 3.7 Area integral of flapper pressure (lbf) - reservoir at 10,000 ft ..... 44
Table 3.8 Pressure difference across the flapper before pressure equalizing ..... 48
Table 3.9 Mass flow rate calculated with respect to different passage diameter..... 48
Table 3.10 Mesh facts for CFD study of pressure equalizing flapper ..... **Error! Bookmark not defined.**

Table 3.11 Reduced pressure results from the CFD analysis for a pressure equalizing flapper... 50
Table 4.1 Instantaneous closure water hammer pressure surge ..... 53
Table 4 2 Finite time closure water hammer pressure surge ..... 54
Table 5.1 Contact types in Ansys® Workbench v12.0..... 57
Table 5.2 Contact settings in the static stress analysis of the flapper valve ..... 57
Table 5.3 Mesh facts for the quasi-static stress analysis ..... 58
Table 5.4 Pressure loading for fully closed case..... 62
Table 5.5 Material fatigue properties for Inconel X ..... 72
Table 6.1 Maximum stress and strain during the flapper cyclic loadings ..... 83
Table 6.2 Damage parameter inputs ..... 87
Table 6.3 Low cycle fatigue estimates for SSSV ..... 91
Table 7.1 Thermal properties of Inconel®718..... 94
Table 7.2 Average velocity, Re and friction number estimations..... 95

# Executive Summary

*The Design Investigation on SSSVs for XHPHT application is funded in part by the Research Partnership to Secure Energy for America (RPSEA) grant DC 1603. The report has not been reviewed by RPSEA and approved for publication. The report does not reflect views of RPSEA.*

The Research Partnership to Secure Energy for America (RPSEA), Technical Focus Area 4 – Step-Change Technology seeks novel technologies which *may* result in improved ultra-deepwater production systems. Sub-Surface Safety Valves (SSSV) are a technology that must have a step change in capabilities for extreme high pressure, high temperature (XHPHT) discoveries to become safely producible. Even in the current (*15 ksi* pressure) environments the major producers have concerns about structural safety and fluid structure interactions. At the new *30 ksi* pressures and higher temperatures an incremental change in current designs will likely not be sufficient. New approaches to SSSV design, through a graduate level task design, can only help in developing the XHPHT resources.

This final report presents the results as part of a graduate student project at Rice University, funded in part by the Research Partnership to Secure Energy for America. The project team consisted of Professor Ed Akin and two graduate students from the Department of Mechanical Engineering and Materials Science at Rice University.

There are mainly two stages for this two year project. The first stage is an extensive survey on the current SSSV technologies, the potential improvement of the current industrial standards on SSSV designs are discussed in details; the current advanced SSSV technologies are reviewed; high strength materials that are suitable for XHPHT applications are summarized. We have actively contacted and talked to our RPSEA contacts from the industry. The second stage is the design stage. Since the design of a flapper SSSV is basically an optimization task constrained by very tight spatial limitations, a series of computer models have been conducted to a new design for the XHPHT environment. We have covered the most important design aspects of a flapper SSSV in this report as follows:

(1) *Fluid structure interactions* – FSI is carried out in a quasi-static way. The motion of the flapper valve is divided into several intervals: for each interval, the fluid pressure is obtained from a computational fluid dynamics (CFD) analysis.

(2) *Water hammer analysis* – The water hammer pressure surge is obtained with an 1D model, and is used to analize the impact caused by the flapper when it slams shut.

(3) *Slam shut impact analysis* – An analytic kinematic and kinetics study was used to estimate the angular velocity and angular acceleration at the instant of full perimeter impact. Both were then applied to create body force loads on the flapper, in addition to the fluid closure pressure. A parametric study on the flapper geometry is carried out by the FEA elasto-plastic stress analysis on the slam shut effects.

(4) *Low cycle fatigue* – The low cycle fatigue analysis is carried out by both damage based model and strain-life based model; this part is new to the design of SSSV.

(5) *Thermal stress analysis* – The thermal stresses caused by the temperature difference between the production fluid and the outer sea water is addressed.

The design is conducted in what the ASME Boiler and Pressure Vessel Code calls a design-by-analysis (DBA) fashion. However, it is important to document that each person conducting an analysis is well qualified to do so. This is discussed more in the conclusions section. With the available software at Rice University, computational fluid dynamics and finite element analysis of the temperatures and stress are carried out in *ANSYS CFX v12.0*, *ANSYS WORKBENCH v12.0* and *SolidWorks 2009*.

It has been proven that the critical information on XHPHT fluid properties are hard to obtain; the data used in this project is supplied by our RPSEA contacts. Finding high strength material temperature related properties, especially cyclic stress strain relations is another difficulty we faced in this project, which prevents us from conducting a further thermal analysis. However, as a result of the analysis, the following recommendations are given:

(1) Reference to ASME Boiler and Pressure Vessel Code Sect. VIII for guidelines on elasto-plastic analysis is necessary.

(2) CFD analysis has verified that a pressure self-equalizing mechanism can significantly help reopen the flapper valve when shut by reducing pressure difference by 40% - 80%.

(3) The parametric study shows that the stress level at slam shut impact can be reduced within the elastic range by a 42% increment of the flapper thickness.

(4) Low cycle fatigue analysis should be included in the design guidelines for safety components such as SSSV. The result of this analysis governed some of our designs and required additional parametric geometry revisions.

# Acknowledgement

We express thanks to our RPSEA contacts: Mr. Jim Chitwood for advice as our technical committee contact person, and to Mr. Jefferson Creek for obtaining reservoir fluid properties that were essential for and flow effect studies.

We also thank Mr. Richard Sukup, of Magnolia Global Energy, for several hours of discussions about current SSSV designs and the challenges to be expected in designs intended for XHPHT conditions.

# Chapter 1

# Introduction

*In this Chapter, the motivation for the investigation of subsurface safety valves for extreme high pressure and high temperature applications is been introduced and the project overview is given.*

## 1.1 Motivation

With the ever growing demand for fuel energy and the diminishing in-land resources, the offshore exploration frontier for oil and natural gas has expanded rapidly recently. It has been shown that at least half of the remaining known oil and gas resources are located offshore (Kallaur 2001). As shown in Figure 1.1, huge reserves of oil and gas have been discovered in the ultra–deep water of the Gulf of Mexico (GOM) most recently. Among which, British Petroleum's *35,055 ft*-depth Tiber well (BP 2009) in the GOM is estimated to contain up to three billion barrels of oil. However, Subsurface Safety Valves (SSSV) are a technology that must have a step change in capabilities for the above mentioned extreme high pressure, high temperature (XHPHT) discoveries to become safely producible.

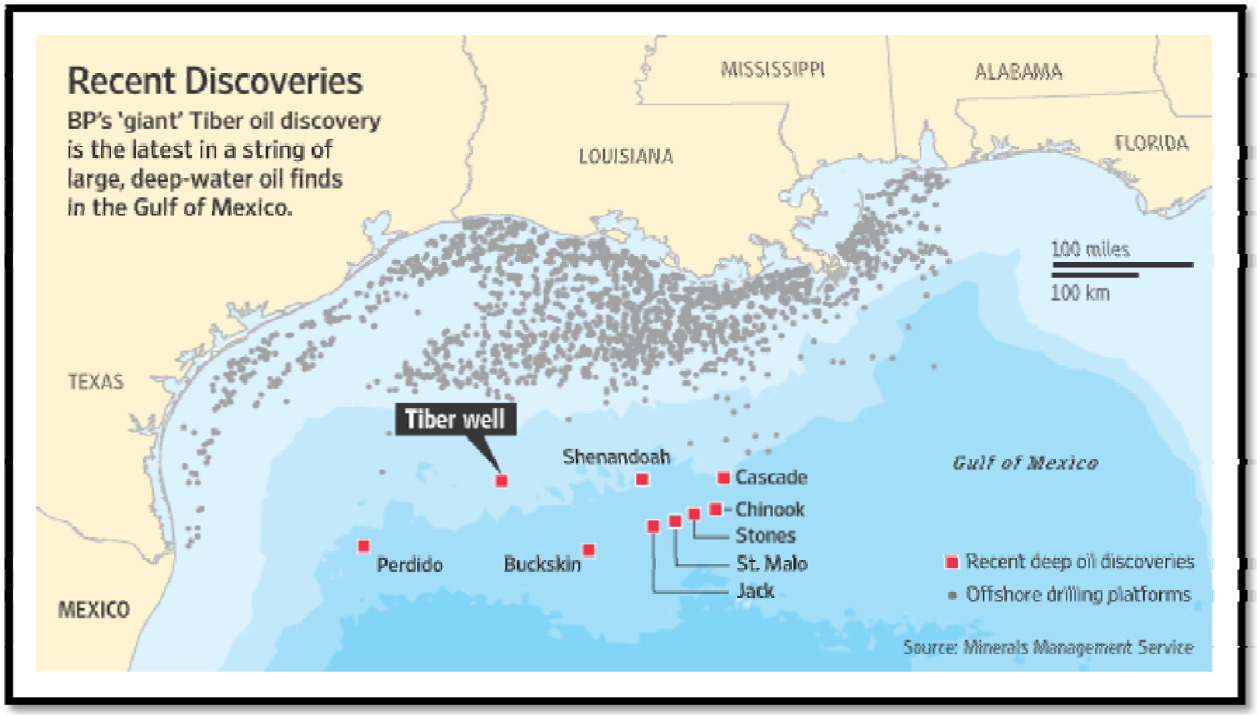


**Figure 1.1 Recent oil and gas discoveries in the Gulf of Mexico (Kallaur 2001)**

A SSSV functions as the fail-safe component for the whole production system, which must shut off the well in emergencies. Historically, subsurface components have a high rate of failure due to severe downhole environments. The Bureau of Ocean Energy Management, Regulation and Enforcement (BOEMRE), formerly US Minerals Management Service (MMS) compiled the failure rate of components (Figure 2) during pressure tests it conducted on the outer continental shelf in 1993-1994. Valves in general had a very high rate of failure. It was also found that the actual testing of (ball type) safety valves lead to their failure due to erosion and other effects.

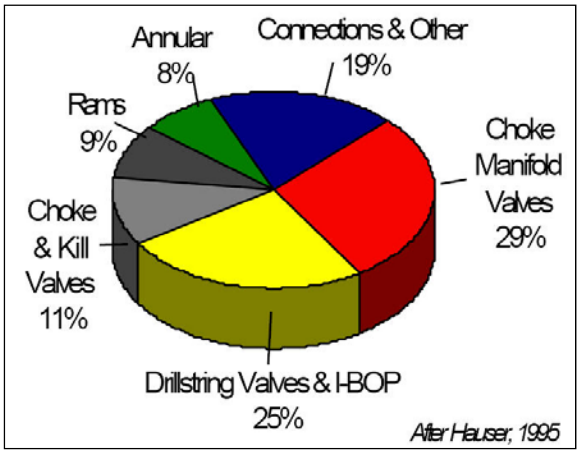


**Figure 1.2 BOEMRE observed component failure rates (Bourgoyne 2002)**

For the extreme high pressure (*30,000 psi*) and high temperature (*450°F*) (Gerner et al. 2002) of the ultra-deep water reservoirs, current design standards for subsurface safety valves are inadequate. The existing performance data of the subsurface safety valves are of little value to refer to for the new design challenges of the subsurface safety valves for XHPHT applications. Incremental design changes are no longer effective. New technologies are difficult to implement because of a lack of performance history. Complex failure modes can still go undetected at the design stage.

Full-scale field testing and validation of XHPHT design concepts are prohibitively expensive, putting an extra burden on the quality of the system modeling. Instead, this project has conducted the SSSV design by an analysis fashion. A comprehensive simulation program were defined for this project to include the following aspects; (1) Dynamic stress analysis; (2) 3D, transient, multi-phase fluid dynamics with compressible flow; (3) Fluid-structure interaction; (4) Correlation to classic water hammer; (5) Heat transfer; (6) Materials science; and (7) Control systems.

This report summarizes the academic design project, *Design Investigation of Subsurface Safety Valves (SSSV) for Extreme High Pressure and High Temperature (XHPHT) Applications*, sponsored by the Research Partnership to Secure Energy for America (RPSEA). Considering

time and resource limitations, the authors have conducted the design investigation and analysis on the following aspects based on the authors' judgment of their importance:

(1) Investigation on high strength materials suitable for XHPHT design applications
(2) Quasi-static fluid -structure interaction for two different valve types under XHPHT environments
(3) Water hammer analysis to evaluate pressure surge impacting on the subsurface safety valve
(4) Parametric studies to lower stress and strain levels on the flapper valve under slam-shut impacts
(5) Low cycle fatigue analysis to evaluate the life cycle span of a flapper valve

## 1.2 Report Overview

The final report is arranged in the following fashion:

In Chapter 2, the limitations of the current SSSV design standards are discussed and possible remedies are pointed out. The background information and literature on current subsurface safety valves are reviewed. Potential high strength materials are surveyed and summarized.

In Chapter 3, the quasi-static fluid structure analysis is first conducted on a flapper shaped subsurface safety valve. A similar study for a hemi-wedge geometry was previously posted on the RPSEA web site. Then, a CFD analysis has been carried out to analysis the pressure equalizing effects of a tiny passage through the flapper.

In Chapter 4, the water hammer problem caused by the sudden closure of the flapper valve is studied using one-dimensional water hammer analysis software.

In Chapter 5, finite element analysis of the stress has been conducted. Elasto-plastic stress analysis is conducted to analyze the impact effects when the flapper slam shuts. The flapper geometry is improved by a parametric study.

In Chapter 6, a low cycle fatigue analysis is conducted on the flapper valve obtained from the parametric study. Both damage based and strain based approaches are implemented and their results are compared.

In Chapter 7, a thermal finite element analysis is also conducted to evaluate the thermal stresses on the subsurface safety valve when it is in the open position.

Finally, in Chapter 8, the summary and recommendations made from this project are given.

# Chapter 2

# Literature Survey

*In this Chapter, an extensive survey has been conducted. The limitation of the current SSSV design standards is pointed out. The erosion of a ball type valve is mentioned. Besides, this chapter will review the current SSSV technologies and potential high strength materials for XHPHT applications.*

## 2.1 Beyond Current SSSV Design Standards

Current API standards and specifications, which are used as universally observed guidelines for the design of subsurface safety valves, only address pressure levels up to *15,000 psi*. They cannot be simply extrapolated to extreme high pressure and high temperature applications. It is not difficult to understand this problem if we review the development of which is the worldwide standard on subsurface safety valve design requirements.

The birth and the development of the API specification 14A were disaster-driven. In the mid-1940s, the subsurface safety valves were first used by Otis Engineering (Kerner et al. 2002) to prevent blowouts in the US inland waters. However, the need for design requirements for the use of subsurface safety valves was not recognized until thirty years later. In 1969, a blowout in an offshore well near Santa Barbara, CA (McCrary et al. 2003) triggered the construction of standards on the subsurface safety valves by American Petroleum Institute (API) task group. In 1974, the US government set up regulations for the mandatory installation of the subsurface safety valve on all the offshore platforms in US federal waters. Later in 1970s, the requirements were incorporated into the API Specification 14A, which was further revised by International Standard Organization (ISO) as a specification accepted as a global standard. API Specification 14A merely specifies the minimum acceptable test requirements for the subsurface safety valve design. However, these minimum requirements in API specifications are based on the expected worst-case downhole environments with an appropriate safety margin. If the subsurface safety valve designed according to the current API specification 14A fails in a real field application, the reason for the failure would be studied by the API task group. Hence the design remedy comes out either as supplemental documents to provide design adequacy or a new edition of API specification 14A is issued.

The development of the API specification 14A also reflects the disagreement among API task group members. The API task group on subsurface safety valves consists of Minerals Management Service (MMS), now BOEMRE, representatives, subsurface safety valve manufactures, and users. For instance, in the API 14A 10th Edition (API 14A 2000), the Minerals Management Services required a 1.5 safety factor applied to the rated working pressure. However, in 2005 when the API 14A 11th Edition (API 14A 2005) was published, the service company and manufacturers believed that the MMS 1.5 safety factor was not practical for

extreme high pressure and high temperature applications, so they abandoned the former MMS safety factor and instead replaced it with an additional safety margin of *5,000 psi* to the rated working pressure. Most recently, in API RP 6HP (API 14A 2007), which is a supplement to the former API specifications addressing practice for equipment with pressure rated over *15,000 psi*, a safety factor of *1.732* is utilized. For high-pressure conditions, a safety factor always gives a higher safety margin than fixed safety margin additions. However, even using a safety factor of *1.732* will not promise a practical design application where downhole pressure may exceed *30,000 psi* with temperature over *450ºF*.

The inconsistency of the safety margin and safety factor definitions makes it evident that the API specifications are not only limited to current knowledge of the downhole conditions, but also to the available testing capabilities. Specifically, the testing equipment may not be able to reach the necessary test requirements for subsurface safety valves. Especially for extreme high pressure and high temperature conditions, the rated pressure could already exceed the current test limits, not to mention the consideration of the safety margin. Therefore, industries have adopted the rule of due diligence: subsurface safety valves are designed and test verified to the limits of their capability. In summary, subsurface safety valves designed according to the current API specifications are likely to be vulnerable. The ASME approach currently seems better from this perspective..

## 2.2 ASME Boiler and Pressure Vessel Codes

As mentioned before, current industrial standards regulating the design of SSSV only covers design aspects for pressure levels up to *15,000 psi*. For XHPHT applications, we can not simply extrapolate them to pressure levels over *30,000 psi*. Therefore, we need to look at additional standards for help. A wide survey of the available standards focusing on pressure vessel and component designs, especially under high-pressure loadings has been conducted. One such standard that pertains is the *ASME Boiler & Pressure Vessel Code (BPVC), Section VIII, Division 2* and *Division 3* (ASME BPVC 2007), which is already required for the construction of pressure vessels intended for an operating pressure over *10,000 psi*. We have concluded that the following concepts from BPVC will benefit the design of a subsurface safety valve for XHPHT applications:

**(1) Two Yield Methods (BPVC Sect. VIII, Div.2, Part 5)**

An elastic-plastic stress analysis is performed in a single loading step, based on a specified stabilized cyclic stress-strain curve representing a cycle. Stress and strain ranges are the direct output from this analysis. This method is performed in the same manner as a monotonic analysis and does not require cycle-to-cycle analysis of unloading and reloading.

**(2) Elastic-Plastic Analysis (BPVC Sect. VIII, Div.3, KD-2)**

If analysis is conducted using numerical methods such as elastic-plastic finite element or finite difference analysis, the material shall be assumed to be ideal elastic, perfectly plastic (non strain-hardening) with a yield strength.

**(3) Shear Loading (BPVC Sect. VIII, Div.3, KD-244)**

The average primary shear stress across a section loaded in pure shear should be limited to 0.4 times the initial yield stress.

**(4) Design Margin**

For an elasto-plastic analysis, an adequate safety margin of at least 1.732 is suggested.

In sum, BPVC has addressed on the plasticity related design problems, i.e., elasto-plasticity, low cycle fatigue, which are missing from the current API standards. However, for fail-safe components, such as subsurface safety valves, plasticity does occur under certain extreme loadings. Therefore, we suggest that the current API standards should include at least the above mentioned aspects from BPVC.

## 2.3 Failures of Ball Shaped Safety Valves

Historically, there are two types of valve geometries available, the ball-type and the flapper-type. Modern subsurface safety valve manufacturers prefer the flapper-type designs because of the multiple failures observed during the operation of ball valves. Details of current flapper valve designs will be introduced later in this Chapter.

Early subsurface safety valves were mostly ball-type safety valves. Compared to flapper-type safety valves, ball-type safety valves are much less reliable because of their rotation mechanism, which means extra components are needed to transform opening force to an opening torque.

Research has been done on the multiple failure modes of the ball-type subsurface safety valves. A. T. Bourgoyone, Jr. (2002) and his team at Louisiana State University (LSU) have done a study on ball type subsurface safety valve in 2002. In their LSU study, it has been pointed out that the main failure of the ball valves to operate as a subsurface safety valve is that it will “lock up” against high flow rates and high differential pressure. The so-called “lock up” phenomenon refers to ball valves’ inability to close due to high closure torque. With an improved trunnion mounted design (Bourgoyone 2002)**,** the opening torque can be reduced and kept constant during its open or closure process. However, a significant erosion problem is inevitable for a ball-type valve since it is always exposed to high-speed flow with mud and sand particles in its open position. Moreover, it is always hard to achieve a perfect alignment of the ball valve and the pipe in practice. A miss-angle alignment could result in erosion not only in the ball valve itself but also to the valve seat. An example of erosion results is shown in Figure 2.1.

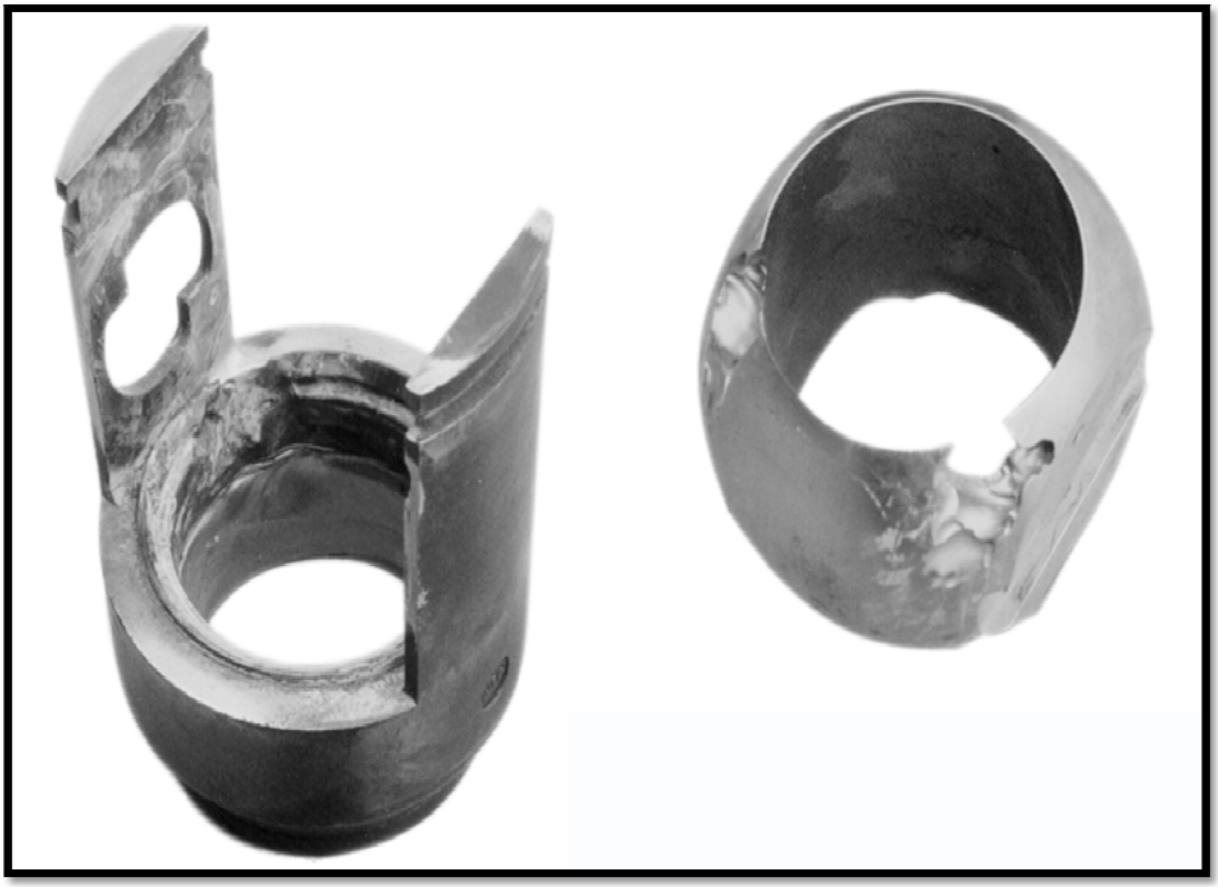

**Figure 2.1 Erosion of Ball and Seat by Drilling Fluid (Bourgoyone 2002)**

Comparatively, flapper-type valve designs are much more reliable with a simpler operation mechanism. The closure of the flapper is an automatic process, and thus no manual alignment or force torque transform is required. Besides, since when the flapper is fully opened, the flapper stays behind the sleeve tubing where no direct interaction between flapper and drilling fluid will occur, erosion will be of much less concern for a flapper design.

## 2.4 Current Flapper Valve Technology

Next, the operation principle of the flapper valve will be introduced. After that, three successful design features of the current flapper valves will also be introduced and their possibility for an XHPHT application will be discussed.

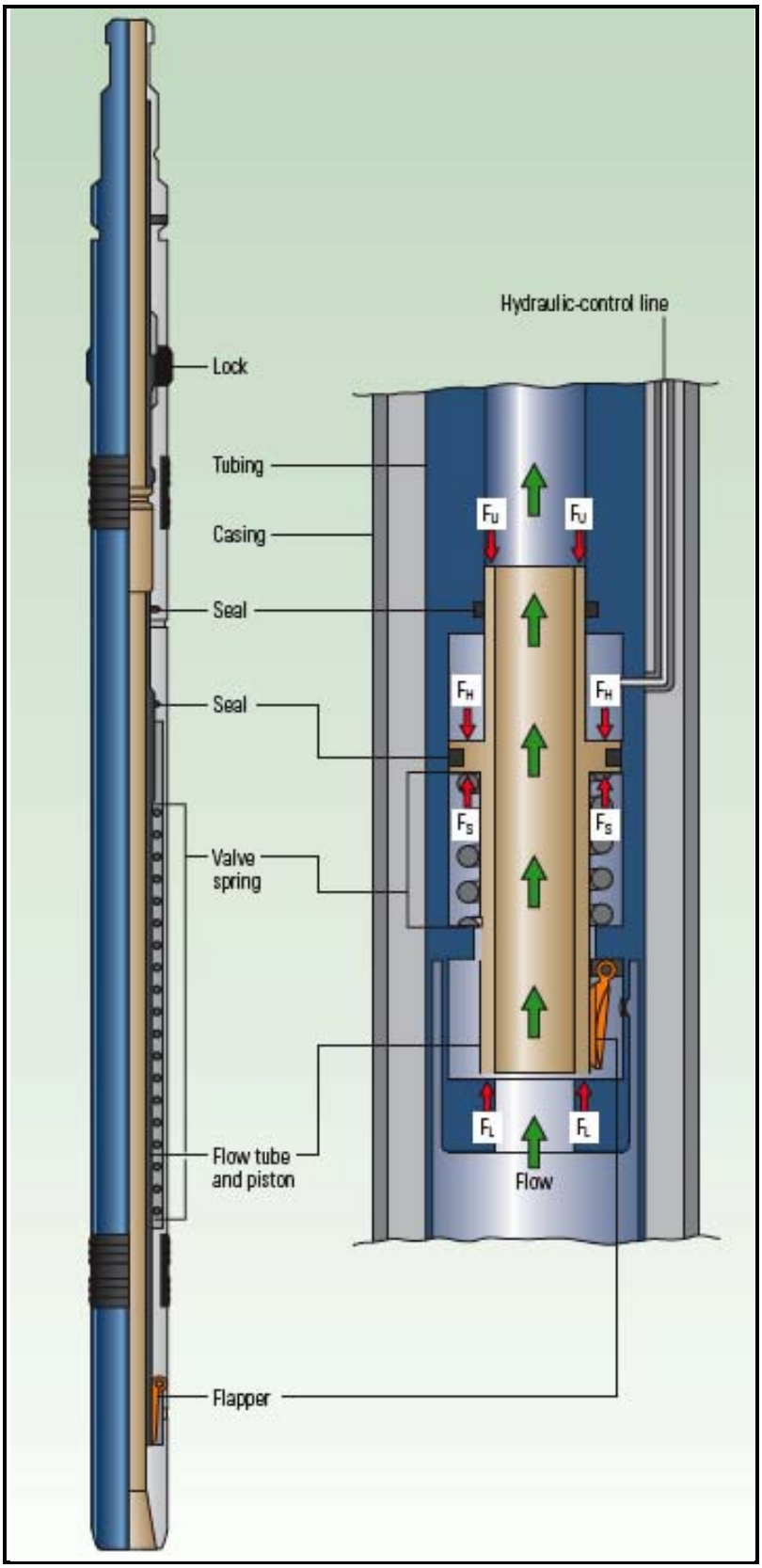


**Figure 2.2 Typical SCSSV designs [5]**

### 2.4.1 Operation Mechanism and Life Expectancy

As shown in Figure 2.2, the typical subsurface safety valve system usually consists of five parts, namely flapper, hydraulic control line, valve spring, sleeve tubing, and outer-tubing. The valve spring is a powerful compressible spring placed coaxially outside the sleeve tube; the sleeve tube is activated by hydraulic pressure exerted onto it through a hydraulic control line, which is controlled at the surface. The hydraulic pressure needs to be large enough to overcome the valve spring resistance and the backside high fluid pressure in order to push the flapper open. When an emergency happens at some upper stage, the hydraulic pressure is lost, the sleeve is retrieved by the valve springs and the fluid pressure from the reservoir side drives the closure of the flapper automatically. To increase the reliability, an additional torsion spring is also included in newer SSSV models to close the flapper against adverse pressure during the closure process. The subsurface safety valve is placed coaxially inside the outer tubing to be connected as a part of the pipe. In short, modern subsurface safety valves are also referred to as surface controlled subsurface safety valves (SCSSV), or in some cases tubing retrievable varieties (TRSCSSV).

The life expectancy of a subsurface safety valve is typically twenty years. During its lifetime, a twice-a-year well test is required by the BOEMRE for wells in Federal lease waters to check the status of the subsurface safety valve. Therefore, the closure and opening process of the subsurface safety valve usually happens during those semiannual tests. Conservatively estimated, a subsurface safety valve should be able to experience one to two hundred open and closure processes during its lifetime. Next, three current successful design features of the flapper valve will be introduced.

### 2.4.2 Curved-Flapper Design

One drawback of the flapper design compared to a ball-type design is its larger outer diameter. The safety valve size is limited by the production pipe and the outer casing. The drilling costs for a larger casing diameter can increase drastically. The inner diameter of the tubing will directly affect the fluid production. Therefore, the flapper design should ideally maximize the flow area while minimizing the outer casing diameter. A curved flapper design is one of the successful endeavors from industrial subsurface safety valve designers to deal with this problem. A slimline curved flapper design from Baker Oil Tools is shown in Figure 2.3. The curved flapper design is nowadays widely adopted by the oil service and manufacturers, including Halliburton, Schlumberger, and Baker Oil Tools.

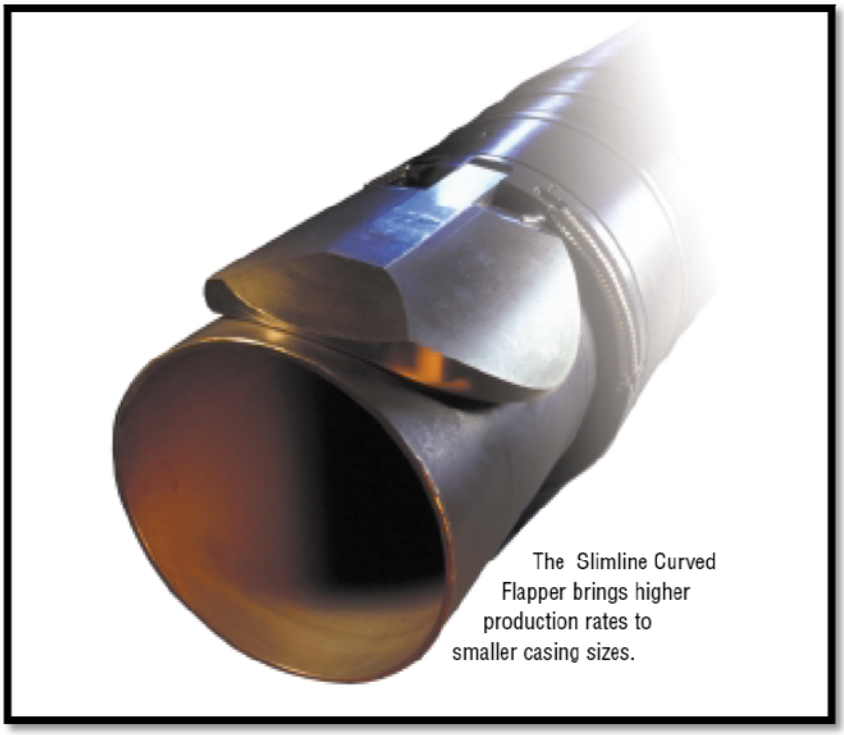


**Figure 2.3 Baker Oil Tools Slimline curved flapper design (Baker Oil Tools 2001)**

## 2.4.3 Pressure Self-Equalizing Technology

A subsurface safety valve will experience around 100 - 200 slam processes during its lifetime. One of the fatal failure modes happening after such a closure of the flapper safety valve is its inability to open again. This failure occurs because of the extreme high pressure built up from the reservoir side, which can be much higher than the maximum hydraulic pressure supplied to open the flapper. One way to solve this problem is to drill open the dead flapper and superimpose a smaller valve to replace it. Although this remedy reduces the production rate of the well, it may be better than killing the whole production string. Another way to solve this problem is by adding a pressure self-equalizing mechanism to the subsurface safety valve. That feature has been widely adopted by various industrial subsurface safety valve designers. Although detailed designs may vary from each other, the underlying ideas are quite similar. One such design is shown in the Figure 2.4. As shown in Figure 2.4, the sleeve tube will first push the poppet to the other side of the flapper. This will create a small channel for the flow to pass through the flapper, which helps to decrease the pressure differential. When the flapper is fully opened, the outer tube will push the both the plunger and the poppet back to their original positions. However, every additional moving part will reduce the reliability of the subsurface safety valve. Possible fluid leakage and functional failure should be considered when including the pressure self-equalizing mechanism. For XHPHT applications, pressure self-equalizing mechanism are suggested, since that is the most effective way to eliminate the pressure lock-up of the flapper that can prevent it from opening.

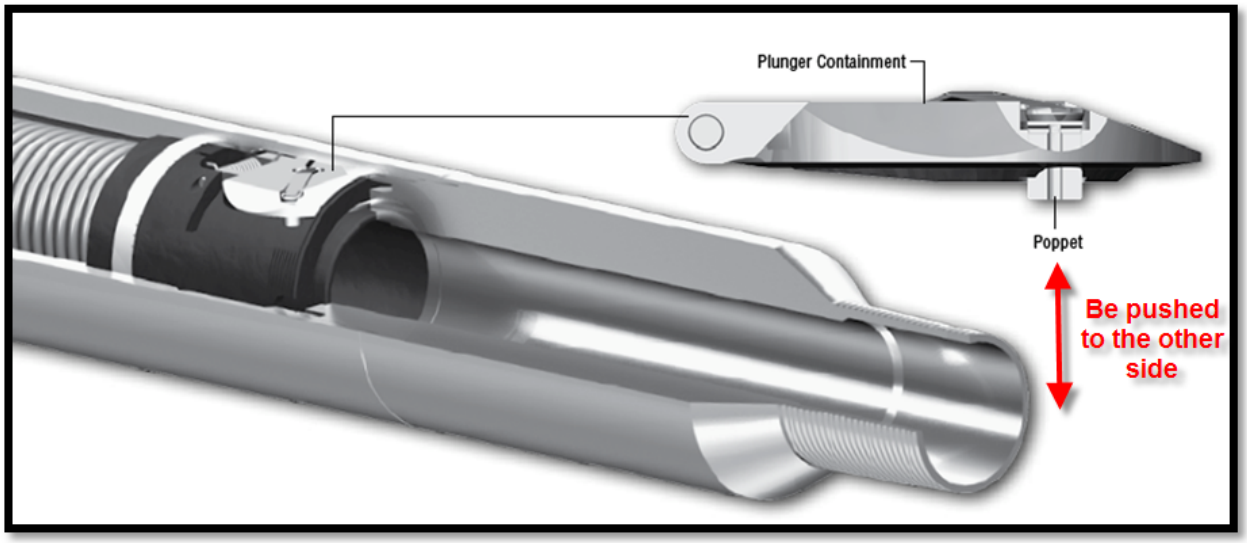


**Figure 2.4 Baker Oil Tools self-equalizing system (Baker Oil Tools 2009)**

### 2.4.4 Floating Magnetic Coupler

As mentioned above, opening a closed flapper requires the hydraulic pressure from the surface control through the control line. The hydraulic pressure is required to be large enough to move the sleeve to overcome the compressed spring and the fluid pressure. Therefore, a magnetic coupler is highly recommended for XHPHT applications (Vizant et al. 2004, Vick et al. 2005). This design was first introduced by Camco (now a division of Schlumberger) in 1960s . (Gerner et al. 2002). The main drawback of hydraulic actuation is its sensitivity to the setting depth and the reservoir pressure. For example, high reservoir pressure leaking into the outer casing has been known to crush control lines and render them useless. To eliminate the dependence of hydraulic control on the setting depth, a new floating magnetic coupler was developed by Halliburton (2008) (LeBoeuf et al. 2008) to isolate the hydraulic control line from the drilling or production fluid. As shown in Figure 2.5, the movement of the flow tube (sleeve tube) is activated by magnetic force instead of by the spring force. A hydraulic control line is built into the outer magnetic metal tube, which isolates it from the drilling environment. Thus, the hydraulic pressure will remain low during the opening process regardless of the setting depth. This change in control mechanisms for the subsurface safety valve is highly recommended for an extreme high pressure and high temperature application. The application of the magnetic coupler design also reduces the chance of valve's "lock up" because of high reservoir pressures. Hence, the reliability of the subsurface safety valve is increased.

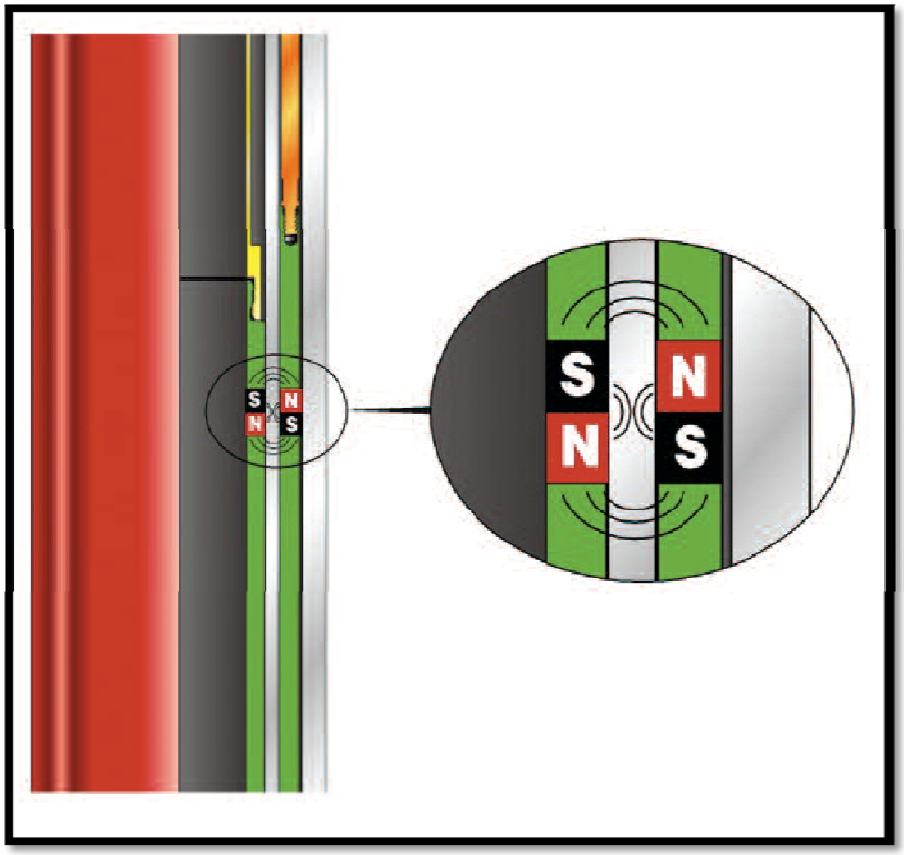


**Figure 2.5 Magnetic-coupler Depth-Star TRSV Halliburton [14]**

## 2.5 Investigation on High Strength Materials

The harsh downhole environments demand the high qualities from the construction material for the subsurface safety valve designs. Two main material concerns for XHPHT applications are:

1) Chemical corrosion resistance in high volume of hydrogen sulfide, polysulfide, and sulfur environments.
2) The maximum strength of the material to resist extreme high stress levels.

To fulfill the above mentioned criteria for material selection, an extensive material search has been carried out in this project. The materials reviews are listed below.

**(1) Aermet® alloy**

Aermet® alloy (Capenter 2009) is an ultra-high strength martensitic steel alloy. Aermet® is the material with the highest strength found in this study. This kind of alloy has an extensive use in aeronautical components, armor, etc., where high strength, high fracture toughness, and exceptional resistance to stress corrosion cracking and fatigue are required. The drawback of the Aermet® alloy is that it is not chemical corrosion resistant, which prevents it from applications in

the oil and gas industry. However, new technologies on corrosion resistant coating treatments of the Aermet® are strongly suggested considering its high strength and possible applications in extreme high pressure and high temperature environments.

**Table 2.1 Material Properties of Aermet**

| | Young's Modulus (ksi) | Yield Strength (psi) | Ultimate Strength (psi) | Density (lb/in³) |
|---|---|---|---|---|
| **AerMet® 340** | 27,900 | 314,000 | 352,000 | 0.284 |
| **AerMet® 310** | 27,900 | 275,000 | 315,000 | 0.288 |
| **Carpenter AerMet® 100 900°F Aged** | 28,200 | 246,000 | 287,000 | 0.285 |

## (2) Corrosion Resistant Alloys (CRA)

The already well-known Corrosion Resistant Alloys (CRA) were first applied in oil and gas industry in 1970s. CRAs are well known for their both corrosion resistant ability and high strength. Hastelloy® and Inconel® are among the most popular CRAs currently.

### I. Hastelloy® Super Alloy

Hastelloy® super alloy is a Nickel-based, high-temperature alloy, which can survive high-temperature and high stress environments with moderate to severe corrosion. The applications of Hastelloy® include pressure vessels of nuclear reactors, chemical reactors, pipes and valves, etc.

**Table 2.2 Material Properties of Hastelloy**

| | Young's Modulus (ksi) | Yield Strength (psi) | Ultimate Strength (psi) | Density (lb/in³) |
|---|---|---|---|---|
| Haynes CABVAL Hastelloy® G-50™ Grade 100 | 27,800 | 125,000 | 110,000 | 0.301 |
| Haynes Hastelloy® D-205 | 29,700 | 104,000 | 142,000 | 0.297 |
| Haynes Hastelloy® alloy N, 1.14 mm sheet, aged 10000 hours at 760°C (1400°F) | 31,800 | 43,700 | 115,000 | 0.32 |

### II. Inconel® Alloy

Inconel is another groups of CRAs with higher strength than Hastelloy. Among Inconel family materials , INCONEL®718 is the one that is most widely used in the oil and gas industry now. INCONEL®718 (Special Metal Co. 2009) is a precipitation-hardenable nickel-chromium alloy with other amounts of iron and niobium.

**Table 2.3 Material Properties of Inconel**

| | Young's Modulus (ksi) | Yield Strength (psi) | Ultimate Strength (psi) | Density (lb/in³) |
|---|---|---|---|---|

| | | | | |
|---|---|---|---|---|
| INCONEL® Alloy 718 | 30,600 | 160,000 | 199,400 | 0.296 |
| INCONEL® Alloy 625 | 30,000 | 110,000 | 128,000 | 0.305 |
| INCONEL® Alloy 600 | 29,878 | 45,000 | 95,000 | 0.306 |

### (3) Other Corrosion Resistant Materials

#### I. Duplex Stainless Steel

Duplex stainless steels are an austenite and ferrite formulated steel with corrosion resistant ability. Duplex stainless steels are about twice as strong as regular austenitic or ferritic stainless steels. Duplex's corrosion resistance depends mostly on its composition just like all other stainless steels. Therefore, Duplex stainless steels have a wide range of corrosion resistance. However, their strength is still comparatively low to the CRAs, and so are their costs.

**Table 2.4 Material Properties of Duplex Stainless Steel (MatWeb 2010)**

| | Young's Modulus (ksi) | Yield Strength (psi) | Ultimate Strength (psi) | Density (lb/in³) |
|---|---|---|---|---|
| Industeel URANUS® 45N+ 22% Cr | 29,000 | 74,000 | 104,000 | 0.282 |
| Carlson 2205 (UNS S32205) | 27,500 | 65,000 | 90,000 | 0.283 |
| Outokumpu 4501 | 29,000 | 76,900 | 117,000 | 0.278 |
| Allegheny Ludlum AL 2205™ | 27,600 | 84,800 | 125,000 | 0.285 |

#### II. Titanium Alloys

Titanium alloys are mostly used in military, aerospace, and medical applications. Titanium alloys are well known for their high tensile strength and toughness (even at extreme temperatures), light weight, and their excellent corrosion resistance abilities. Althoughthe cost of the titanium alloys have dropped significantly in recent years, they are still considered one of the most expensive materials in the world and thus their implementations in the oil and gas industries are quite limited.

**Table 2.5 Material Properties of Titanium Alloys [18]**

| | Young's Modulus (ksi) | Yield Strength (psi) | Ultimate Strength (psi) | Density (lb/in³) |
|---|---|---|---|---|
| Titanium Ti-6Al-2Sn-4Zr-2Mo-0.1Si | 17,100 | 152,000 | 161,000 | 0.164 |
| Titanium Ti-10V-2Fe-3Al (Ti 10-2-3) Solution Treated 850°C | 16,000 | 135,000 | 145,000 | 0.168 |
| Titanium Ti-6Al-2Sn-4Zr-2Mo (Ti-6-2-4-2) | 16,510 | 125,000 | 136,000 | 0.164 |

## 2.6 Materials Survey Summary

In conclusion, the design work of subsurface safety valve for extreme high pressure (*30,000 psi*) and high temperature (*450°F*) applications is a challenging task. It clearly will require very high strength materials.

The idea of using ball valves should be abandoned because of their intrinsic failure modes related with the rotational mechanism. The hemi-wedge geometry, discussed elsewhere in this report, has a much lower closing torque and good metal-to-metal seals so it may merit additional future study. In contrast to a classic ball valve, the flapper-type subsurface safety valve seems to be a much more robust design. The pipe flow cross-section can be enlarged by a curved flapper design. The lockup failure during reopening process due to high reservoir pressure and low hydraulic pressure is solved by the application of pressure self-equalizing design and magnetic coupling.

However, the reliability of current flapper valve designs under an extreme high pressure and high temperature application is still not assured. Therefore, seeking a new design approach for the flapper valve is necessary to fail-safe in XHPHT environments.

# Chapter 3

# Computational Fluid Dynamics

*In this Chapter, a computational fluid dynamics model is first set up, and then a quasi-static fluid structure analysis has been conducted to model the flapper valve opening process. After that, a CFD analysis has been conducted to evaluate the pressure self-equalizing mechanism.*

## 3.1 CFD Analysis with ANSYS® CFX v12.0

The computational fluid dynamics software used for this project is Ansys® CFX v12.0. The fluid pressure results from Ansys® CFX v12.0 can be easily transferred into Ansys® Workbench for a further static stress analysis.

Ansys® CFX v12.0 has a complete analysis system consisting of pre-process, solving and post-process modules. Moreover, with the help of the ANSYS® Workbench v12.0, which has a good interface with other Computer Aided Design (CAD) software (i.e. SolidWorks), one could build up CAD geometry in SolidWorks and then easily transfer it to a fluid domain in ANSYS® and mesh the domain with CFX-mesh generator. Then the boundary conditions, turbulence models, and fluid properties are defined in CFX-pre. After the CFD problem is fully defined, it is handed to the CFX-solver for a solution. After the solution is converged, the corresponding pressure and velocity plots are obtained in CFX-post. The flow chart for the computational fluid dynamics analysis is shown in Figure 3.1.

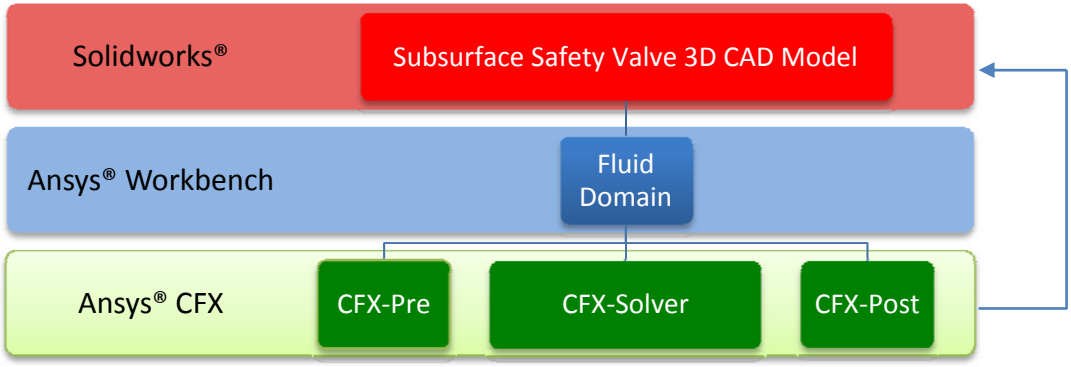


**Figure 3.1 CFD flow chart**

Solving fluid governing equations analytically for practical problems without over simplification are almost impossible. Numerical approaches therefore are applied to transform the governing equations into algebraic equations for approximate solutions. Such a numerical discretization method utilized by CFX is called the finite volume method (FVM). The FVM is one of the most

commonly used numerical methods in CFD. One of the most important advantages of the FVM is that the conservation of quantities (i.e., mass, momentum, and energy) is assured for the results regardless of the quality of mesh. Suppose $Q$ is the quantity of interest, $\Omega$ is the finite volume, $F$ is the flux on the finite volume boundary $\Gamma$. For each finite volume, the following conservation is satisfied as in (del Coz Diaz et al. 2007)

$$\frac{\partial}{\partial t}\int_{\Omega} \boldsymbol{Q d\Omega} + \oint_{\Gamma} \boldsymbol{F d\Gamma} = \mathbf{0}\ . \tag{3.1}$$

The idea of FVM is to descretize the fluid domain into different meshes, and then the meshes are used to construct control volumes or finite volumes. The unknown variables are located at the center of each finite volume and the interpolation functions are applied between variables. Differential governing equations are integrated over the control volume to get the final discretized equations to solve.

### 3.1.1 XHPHT Production Fluid Properties

In order to conduct CFD analysis on subsurface safety valves in extreme high pressure (*30,000 psi*) and high temperature (*450°F*) conditions, an intensive search for the corresponding reservoir fluid properties under such conditions was required. However, it has proved to be extremely difficult to obtain the correct fluid properties. It took several months to be able to obtain data for the single sample reservoir reported below. Such data are very expensive to obtain and operating companies tend to consider them proprietary. It was originally expected that this design investigation would utilize properties from a few different fields to establish a range of pressure loadings from the fluid-structure interaction. That was not possible. Perhaps the government should require the establishment of a public database for such properties data as part of the field leasing requirements. Otherwise, the SSSV designs will have a large range of uncertainty.

Since viscosity is the vital property for the quasi-static flow simulation, it is most desirable to obtain viscosity at the aimed design pressure and temperature. Otherwise, with the knowledge of gas solubility and bubble point pressure, proper interpolation with the empirical formulations (Ahmed 2006) should be conducted to obtain densities and viscosity at the design pressure and temperature. There are numerous relationships correlating dead oil viscosities and temperatures (Bergman et al. 2009); none of them includes pressure factors although fluid viscosities depend heavily both on temperature and pressure. Recently, Schmidt (2005) has studied density and viscosity behavior of crude oil and natural gas liquid with changes in temperature and pressure. However, the highest pressure studied was under *5,801 psi* (*400 Bar*), which is much lower than the investigation design pressure. Moreover, crude oil properties can be significantly different depending on different geographical locations and molecular fractions. Their study of North Sea fluid properties should not be generalized.

Though empirical estimates of viscosities have proven to be unavailable, experimental measurements of extreme HP/HT viscosities seems to be successful. A new extreme HP/HT viscometer has been developed by William Gusler et al. (2007) and claimed to be capable of accurate measurements of drilling fluid viscosities up to *600°F* and *40,000 psig*. Considering the high cost and time inefficiency, obtaining experimental measurements is not practical for this design investigation project.

Besides viscosity, gas solubility, and bubble point pressure, other critical properties that need to be known are the crude oil density and compressibility at extreme HP/HT conditions. Compressibility is important for the water hammer analysis. It will be discussed later in the water hammer Chapter.

After examining the current empirical and experimental methods for obtaining extreme high pressure and high temperature fluid properties, none of them seems to be applicable to the current design range. That is, numerical investigations of the curve-fitted empirical equations showed them to be not self consistent when extrapolated to higher temperatures and/or pressures. With the help of our RPSEA project contacts, Chevron has offered us the following suggestions on fluid properties. These properties have been used in the computational fluid dynamics simulations. They are listed in Table 3.1.

**Table 3.1 RPSEA Suggested Extreme HP/HT Fluid Properties**

| | |
|---|---|
| **Dynamic Viscosity** | *1.0 cp* at *30,000 psia* and *450 °F* |
| **Density** | *0.792 g/ml* ( *49.47 lb/ft*$^3$) at *30,000 psia* and *450 °F* |
| **Gas Solubility** | *530 SCF/STB* |
| **Bubble Point Pressure** | *3,100 psia* at *450°F* |
| **Compressibility** | *4.11E-06 psi*$^{-1}$ at *30,000 psia*<br>*2.25E-05 psi*$^{-1}$ at *4,000 psia* and *450°F* |

## 3.1.2 Pipeline Hydraulics

With the proper fluid properties, the next step is to develop the correct production pipeline fluid velocity profiles for the quasi-static computational fluid dynamics analysis.

### (1) Pipeline Reynolds Number

Typically, there are three types of flow in a pipeline- laminar, transitional, and turbulent. The velocity profile of a pipeline flow at each pipeline cross-section can be different depending on its type. The velocity profile of a laminar flow is parabolic while the profile of a turbulent flow is more like a trapezoidal shape. These three pipeline flows can be categorized with a

dimensionless number, Reynolds number. In a circular pipe for Newtonian fluids, Reynolds number is usually defined as

$$\boldsymbol{Re} = \frac{\rho V_{avg} D}{\mu} = \frac{V_{avg} D}{\gamma} \tag{3.2}$$

Where is the average velocity is $V_{avg}$ at a circular pipe cross-section of a diameter $D$, $\gamma = \mu/\rho$ is the kinematic viscosity of the fluid. One thing to mention here is that in a real pipe flow case, whether a flow is laminar or turbulent also depends on other factors including pipe surface roughness, pipe vibration, and flow fluctuations as well as fluid or slurry characteristics. However, Reynolds number can offer us a reasonable estimate of the flow types. Usually the Reynolds number of laminar flow is below *2,300*, the Reynolds number of transitional flow is between *2,300* and *4,000*, and the Reynolds number for turbulent flows is over *4,000*.

Considering the fluid properties suggested by RPSEA, the kinematic viscosity for an extreme HP/HT crude oil is $\gamma = 1.0\ cp$. Assuming a constant pipe diameter $D = 3.5\ in$, the critical average velocity for distinguishing flow types can be obtained from (4.1) as follows,

**Table 3.2 Critical average velocity**

| *Re* | *2,300* | *4,000* |
|---|---|---|
| $V_c$ | *0.107 ft/s* | *0.186 ft/s* |

### (2) Pipeline Energy Equation

After define the pipeline Reynolds number, the average velocity of the crude oil at the pipeline cross-section is calculated. Both energy and mass conservation need to be fulfilled for a pipe flow. According to Bernoulli's equation, the energy equation for one-dimensional inviscid flow is constant at any point during the pipeline. A viscous dissipation term is added to account for the head loss caused by the friction force between the pipe walls and the crude oil. Assuming the subsurface safety valve is placed in a vertical pipeline connecting the deep reservoir to the sea level platform, the mass conservation ensures a constant flow rate. Therefore $V_{avg}$ is constant at all pipe cross-sections. As a result, the total energy equation for the steady, incompressible viscous oil flow in a drilling pipe is expressed as,

$$\frac{P_1}{\rho g} = \frac{P_2}{\rho g} + (z_1 - z_2) + h_f = \frac{P_2}{\rho g} + L + H_f \tag{3.3}$$

In (3.3), because the production pipe is vertically placed in the outer casing, the distance L between cross-section 1 and cross-section 2 is the vertical elevation $\Delta z = z_1 - z_2$. $H_f$ is the head loss counted for the friction dissipation from cross-section 1 to cross-section 2 in a pipeline. The head loss is a function of the friction factor *f*, flow distance *L,* pipe diameter *D,* and the average kinematic energy $V_{avg}^2/2g$,

$$H_f = f\left(\frac{L}{D}\right)\left(\frac{V_{avg}^2}{2g}\right) \tag{3.4}$$

The next step is to determine the friction factor *f* for the vertical production pipe flow. It can be obtained by the assumption that the flow in the drilling pipe is fully developed (steady state) turbulent flow. The friction factor for the flow depends on the Reynolds number and relative roughness, which is expressed in Cengel and Cimbala (2004) in an implicit form:

$$\frac{1}{\sqrt{f}} = -0.2log\left(\frac{\varepsilon/D}{3.7} + \frac{2.51}{Re\sqrt{f}}\right) \tag{3.5}$$

Lester (1994) gives an approximate explicit form of Colebrook's equation. It achieves friction factors within *2%* error to the implicit form. In this calculation, this explicit form is used to ensure a simple and practical estimation

$$\frac{1}{\sqrt{f}} := -1.8log\left[\frac{6.9}{Re} + \left(\frac{\varepsilon/D}{3.7}\right)^{1.11}\right] \tag{3.6}$$

A typical roughness for a pipeline is very small. Assuming the drilling pipe is smooth, $\varepsilon = 0$, the approximation function for friction factor is only factor the of Reynolds number,

$$\frac{1}{\sqrt{f}} := -1.8log\left(\frac{6.9}{Re}\right) \tag{3.7}$$

So far, the Reynolds number (3.2), energy equation (3.3), and the fiction factor (3.7) have been defined for a steady turbulent flow in a vertically placed smooth pipeline. For further calculation to obtain the three quantities mentioned above, suitable assumptions are made about the extreme HP/HT reservoirs. Three hypothetical reservoirs have been found at depths of *10,000 ft*, *20,000 ft,* and *30,000 ft* deep from the sea level. The reservoir pressure is assumed to be *30,000 psi* regardless of the depths, which is a good assumption about extreme high-pressure conditions. The crude oil flows from the depth of reservoir with reservoir pressure to the sea level with atmosphere pressure. Thus, in (3.3), $P_1 = P_{RESERV}$ = *30,000 psi* and $P_2 = P_{ATM}$ = *14.696 psi* and *L* equals the depth of the reservoir.

With these assumptions, average velocity, Reynolds number and friction number were obtained from equations (3.2), (3.3) and (3.7), respectively. An iterative method is applied with the help of Microsoft Excel to obtain the correct average velocity, Reynolds number, and friction number. The results have been shown in Table 3.3. The Reynolds number obtained indicates a turbulent pipe flow.

**Table 3.3 Average velocity, Re and friction number estimations**

| Reservoir Depth | Vavg (ft/s) | Re | Friction No. |
|---|---|---|---|
| *10,000* | *120.892* | *2,594,467* | *0.00993* |
| *20,000* | *76.953* | *1,651,497* | *0.01067* |
| *30,000* | *56.53* | *1,213,187* | *0.01122* |

### (3) Power-law Turbulence Model

A suitable velocity profile will be needed for the inlet boundary conditions of the computational fluid dynamics analysis. Now that the average velocity has been achieved, the next step is to obtain the velocity profile, as well as the maximum velocity. By definition, the average velocity at a circular cross-section is expressed (in Cengel and Cimbala 2004) as

$$\boldsymbol{V_{avg}} = \frac{\int_A \rho u(r) dA}{\rho A} = \frac{\int_0^{D/2} \rho u(r) 2\pi r dr}{\rho \pi R^2} = \frac{8}{D^2}\int_0^{D/2} u(r) r dr \qquad (3.8)$$

Since the Reynolds number indicates a turbulent flow in the pipe, a power-law velocity profile is used to simulate turbulent flow velocity. Power-law velocity gives a relatively good representation of the shape of the turbulent flow in pipes and is easy to apply in commercial codes,

$$\boldsymbol{u(r) = u_{max}\left(1 - \frac{r}{R}\right)^{\frac{1}{n}}} \qquad (3.9)$$

Where, *n* depends on the friction factor *f*. Usually, when *f*<0.1, *n* can be obtained as follows

$$\boldsymbol{n = \frac{1}{\sqrt{f}}} \qquad (3.10)$$

Therefore, the average velocity $u_{avg}$ can be expressed as a function of *n,* and the maximum velocity $u_{max}$ from (3.8) as follows

$$\boldsymbol{u_{avg} = \frac{2n^2}{(1+n)(1+2n)} u_{max}} \quad . \qquad (3.11)$$

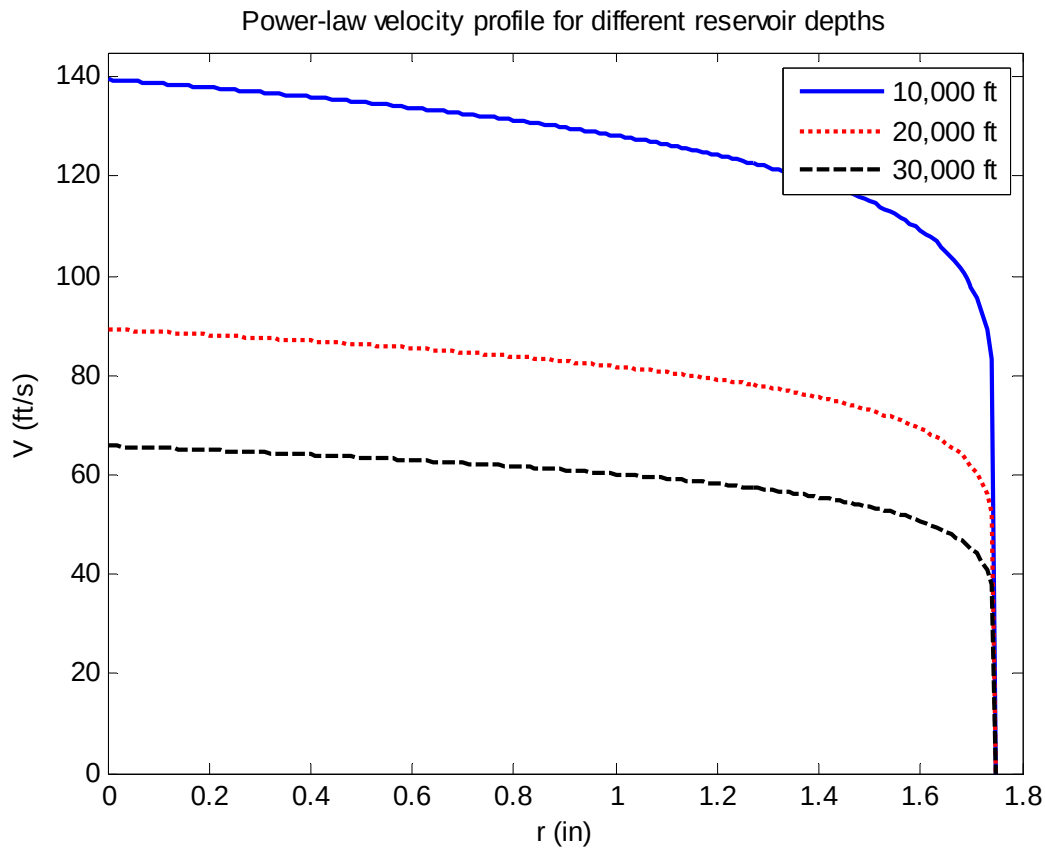


**Figure 3.2 Power-law velocity profile as inlet boundary conditions**

It has been shown in Figure 3.2, the average velocity is close to the maximum velocity in case of turbulence and for deeper reservoirs, the maximum velocity decreases and the velocity profile becomes more flat. The power-law velocity can be expressed using n and the maximum velocity calculated as in Table 3.4.

**Table 3.4 Power-law Velocity Profile in Terms of *n* and Maximum Velocity**

| Reservoir Depth (ft) | *n* | Vmax(ft/s) |
|---|---|---|
| *10,000* | *10.035* | *139.562* |
| *20,000* | *9.682* | *89.285* |
| *30,000* | *9.441* | *65.829* |

### 3.1.3 Shear Stress Transport $k-\omega$ Turbulence Model

From the high Reynolds number calculated from the last section, highly turbulent flows are expected from the CFD results. Therefore, a suitable turbulence model needs to be selected for CFX to ensure an accurate numerical result. Among all the turbulence models available from CFX, a shear stress transport (SST) model is applied with an automatic wall treatment.

Shear stress transport $k-\omega$ model is a two-equation eddy-viscosity model. Two-equation models are currently the most popular turbulence models available. Two-equation models like

$k-\varepsilon$ model and $k-\omega$ model are currently industry standard models, where the turbulent kinematic energy is $k$. $\varepsilon$ is the turbulent dissipation and $\omega$ is the specific dissipation. Menter (1993, 1994) combined and modified these two models together in 1993 to obtain the new shear stress transport turbulence model. In the SST turbulence model, the $k-\varepsilon$ model is used in the inner region to take advantage of its comparatively simplicity so as to achieve better numerical stability while $k-\omega$ model is used in the outer or free-stream region because it is independent of the free-stream turbulence. Besides, a modification to the eddy viscosity emphasizes the cause of the adverse pressure gradient flows as the transport shear stress. The SST $k-\omega$ model has proven to be well performed in situations of adverse pressure gradients and separating flow (Sharma 1974, Wilcox 1988). This relates to the CFD analysis of the flapper where adverse pressure gradients and flow separations are expected from the downstream side of the flapper.

CFX also suggests using an automatic wall treatment with the SST turbulence model (Ansys 2009) to achieve better accuracy, which is the default option in CFX Specifically in the CFD analysis of the pipe and valve system, accurate dealing with the boundary layer near pipe wall becomes very important. Automatic wall treatment will switch from a low-Reynolds number formulation to wall functions based on the grid spacing while the accuracy of low-Reynolds number formulation depends heavily on how the near wall resolution is refined.

## 3.2 Quasi-Static Fluid Structure Interaction

The changing pressure of the fluid field through the subsurface safety valve during its closing and reopening process is critical to the design of the valve. A quantitative evaluation of the fluid pressure acting on the flapper surface should be obtained for further stress analysis. The physical properties of the reservoir fluid such as density and viscosity under extreme high pressure and high temperature conditions are necessary for the computational fluid dynamics study. Careful pipeline hydraulics derivation of the velocity boundary conditions has been conducted based on ultra-deep reservoir assumptions.

Full fluid-structure-interaction (FSI) is desired to evaluate the fluid pressure and velocity variation during valve's rotational motion. However, for this project a full FSI will be too time consuming and beyond the software and hardware capability available for this project. More specifically, a full FSI is prohibitive for this project for the following three main reasons:

(1) Hardware Limitation - All the computations conducted are through the PC machines in the CAD laboratory at the Mechanical Engineering and Materials Science Department, Rice University. The machine memory does not allow the software to create fine meshes.

(2) Software Licensing - The software available for computational fluid dynamics in this project is the ANSYS CFX v12.0 educational version. We were not allowed to use the parallel version due to contractual limitations.
(3) Full FSI function with large mesh deformation is not active.

(4) Project Time Range - The authors try to address as many important aspects as possible for improving the current SSSV designs; therefore, full FSI is not realistic for the current contractual time frame.

Therefore, this project conducts the FSI in a quasi-static fashion. A set of quasi-static computational fluid dynamics analysis have been conducted in Ansys® CFX v12.0 to analyze the flow velocity and pressure field change during the opening process of the flapper. A total nine cases of different opening angles (5°, 15°, 25°, 35°, 45°, 55°, 65°, 75°, 85°) have been simulated. The opening angles are defined as in Figure 3.3.

### 3.2.1 Fluid Domains

The fluid domain in CFX has been built into three main cylinders, the inlet cylinder, the central cylinder, and the outlet cylinder. The radius of the central cylinder is the maximum outer radius (parametric dimension name FlapMax_OD) of the flapper valve design. The length of the central cylinder is *6 in*. The inlet cylinder has a length of *7 in*. The outlet cylinder has the same length of the sleeve tube as *7 in*. Both cylinders have the same diameter of *3.5 in* (the design diameter for the flow passage). The flapper at different closure angles has been cut from the central cylinder through Boolean operations. Unnecessary details of the SSSV assembly, such as fillet features and the torsion spring, have been omitted in order to improve mesh qualities and avoid extra numerical difficulties. The fluid domain for one closure case is shown in Figure 3.4,

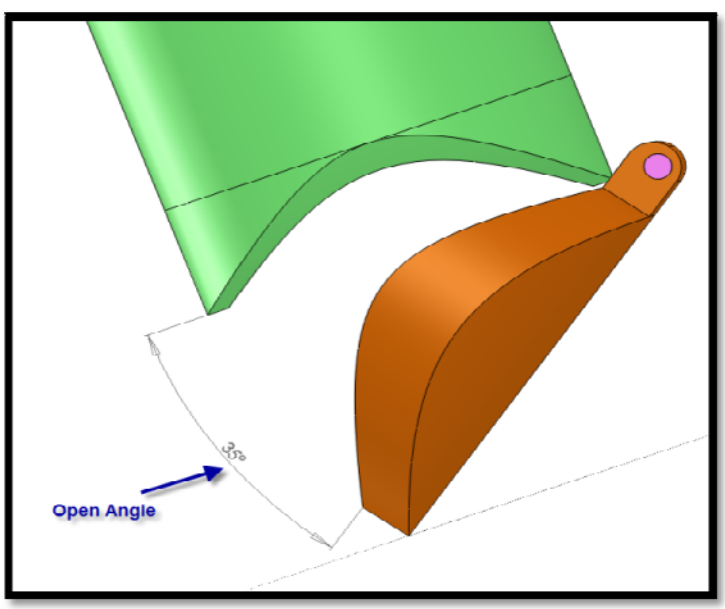

**Figure 3.3 Definition of a 35° opening angle**

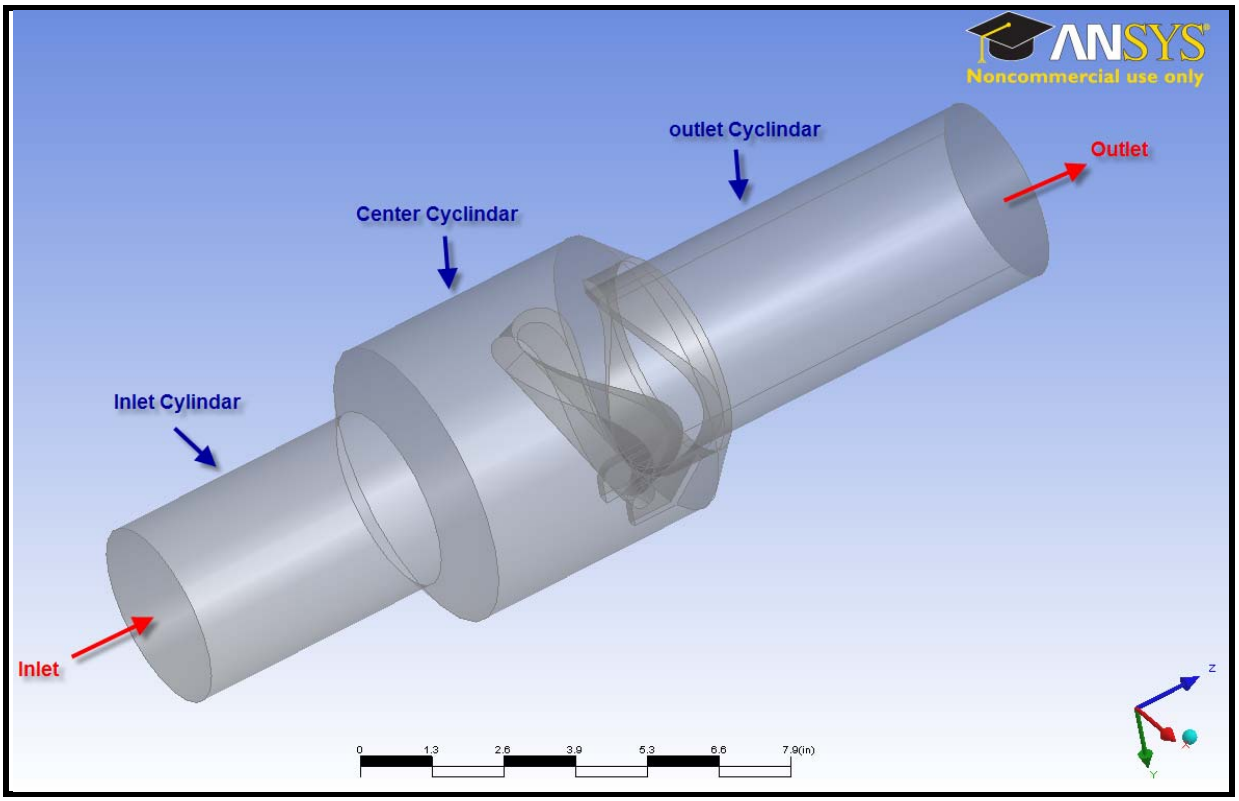


**Figure 3.4 Basic fluid domain (25 degree open)**

The surfaces of the default fluid domain need to be defined to specify the locations where further feature settings can be applied in CFX-Pre. For the SSSV fluid domain, a total of seventeen surface regions have been defined in a symmetric way as in Figure 3.5. Specifically, eleven regions for the outer surface of the fluid domain (named: inlet, outlet, intube, tubeups, tubemid, tubedns, slvl, slvr, slvmthl, slvmthr, and default regions). Six regions are for the surface of the

flapper (and are named flap_upsl, flap_upsr, flap_dnsl, flap_dnsr, flap_sdl, and flap_sdr).

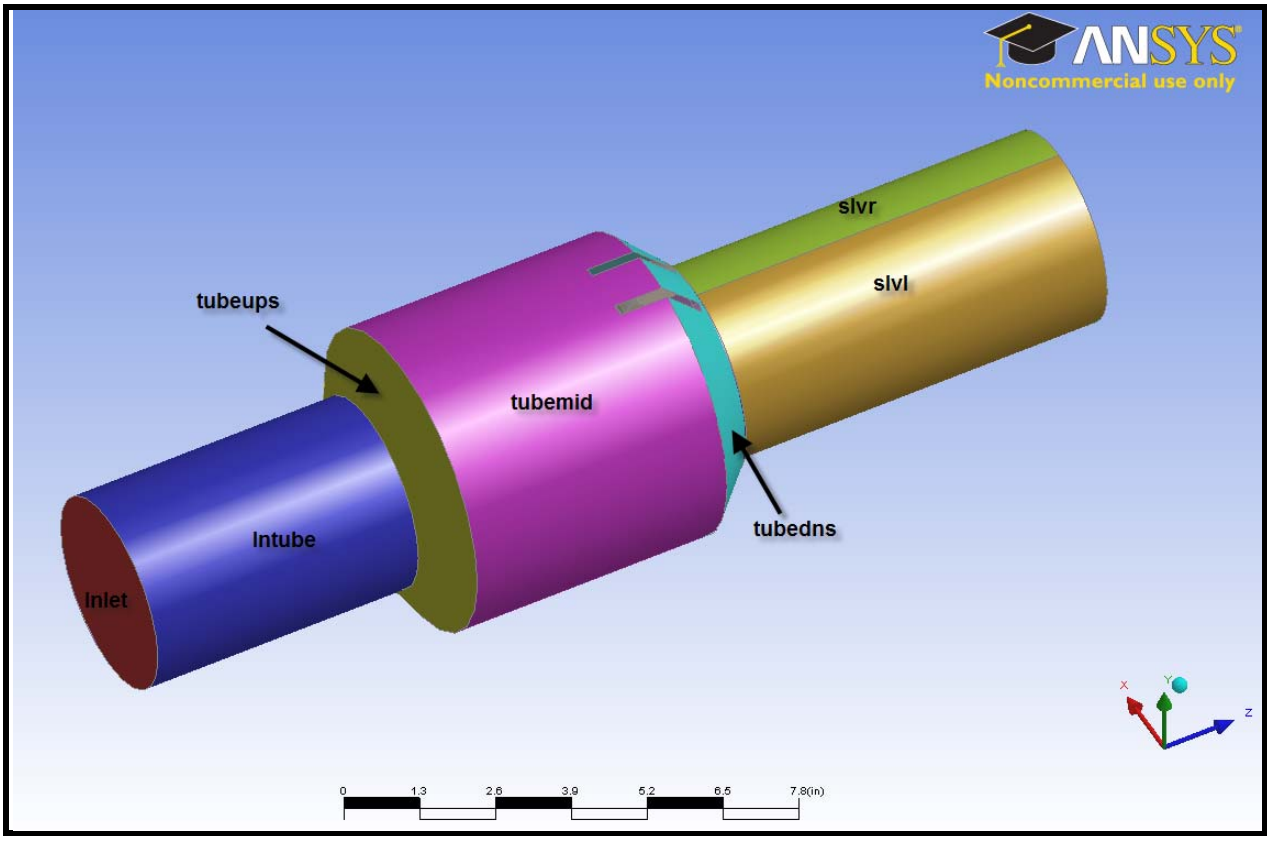


**Figure 3.5 Regions definition (25 degrees open)**

## 3.2.2 Spacing and Inflated Boundaries

For the flapper subsurface safety valve design, adverse pressure gradient is expected around the flapper as well as in the boundary layer separation. A refined mesh is needed on the surface of the flapper and its neighborhood. A surface mesh control is added to the surface of the flapper (named: Flap_upsl, Flap_upsr, Flap_dnsl, Flap_dnsr, Flap_sdl, and Flap_sdr) with a constant mesh size of *0.01 in* (Figure 3.6). The mesh expansion factor is set to be *1.5* and influence radius of *0.3 in*. The flow situation is also expected to vary distinctly where the flow cross-section expands or shrinks. Therefore, edge size control is also applied to the two intersection circles between central and the inlet cylinder, central and outlet cylinders, respectively. The mesh expansion factor is set at *1.5* with an influence radius of *0.3 in*. The meshes at boundary layers also need to be addressed. CFX offers an inflation feature. Utilizing the default 2D regions, inflation features are applied to the cylinder surfaces of the three main cylinder domains. The maximum depth of the inflated boundary is set to be *0.2 in* with an expansion factor of *1.5* for five layers of meshes (Figure 3.7). The expansion factors allow the elements to be very small at the wall (or other feature), and yet allow the size of neighboring elements increase without adversely affecting the accuracy of the solution.

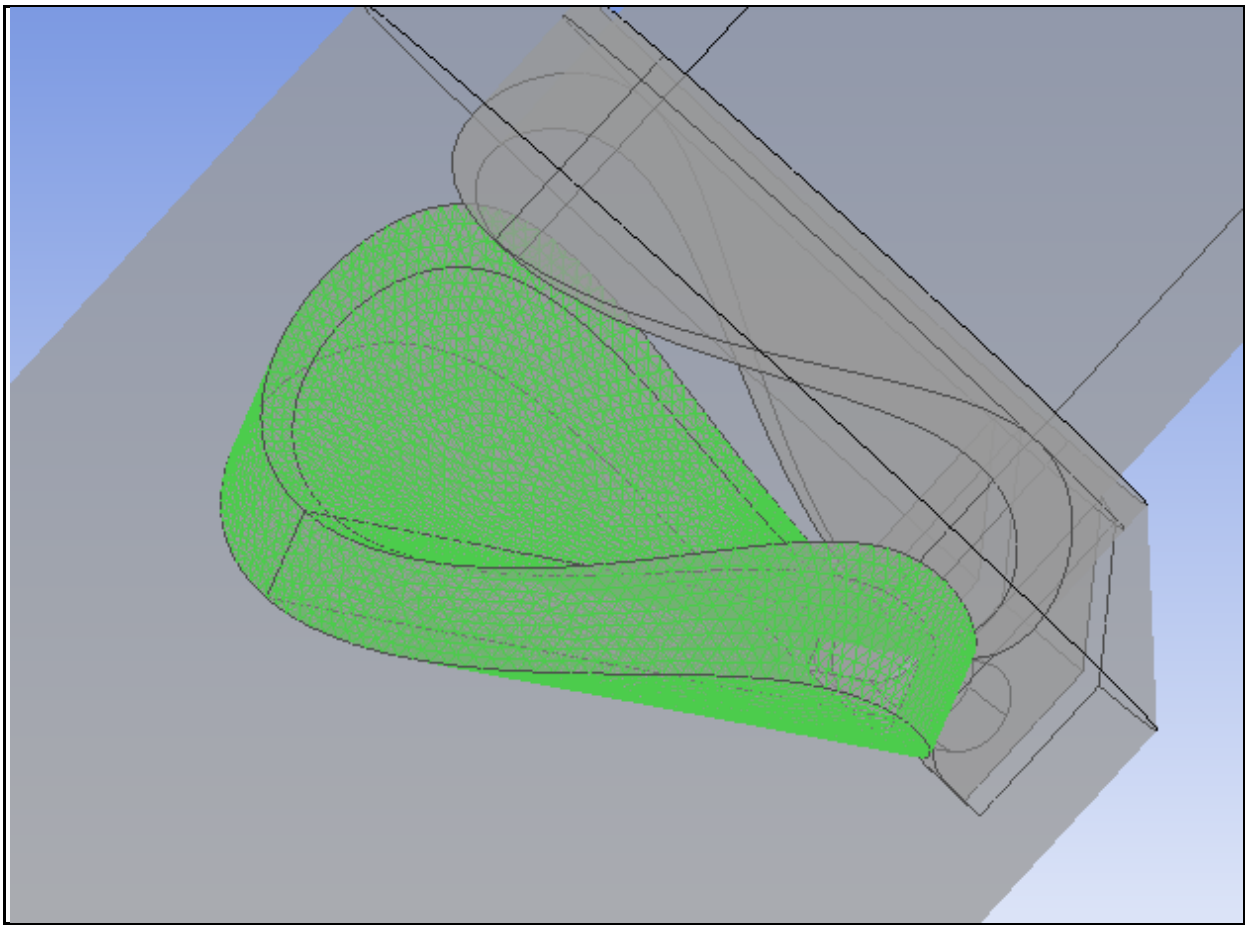

**Figure 3.6 Flapper surface mesh control with constant size of 0.08 in (25 degrees open)**

### 3.2.3 CFD Mesh Facts

Totally, nine cases have been successfully meshed and the mesh summary is shown in Table 3.5. Total node numbers are controlled from *223,080* to *386,661*, which is within the *512,000* node limits according to the available computer memory capabilities. One of the mesh results for *25-degree* open case is shown in Figure 3.8. The total nodes shown in Figure 4.8 are *380,312* and the total elements shown are *2,000,670*. The mesh consists of tetrahedral, pyramid, and prism elements. Beside the region where surface control is applied, meshes around shape edges in the fluid domain are also refined.

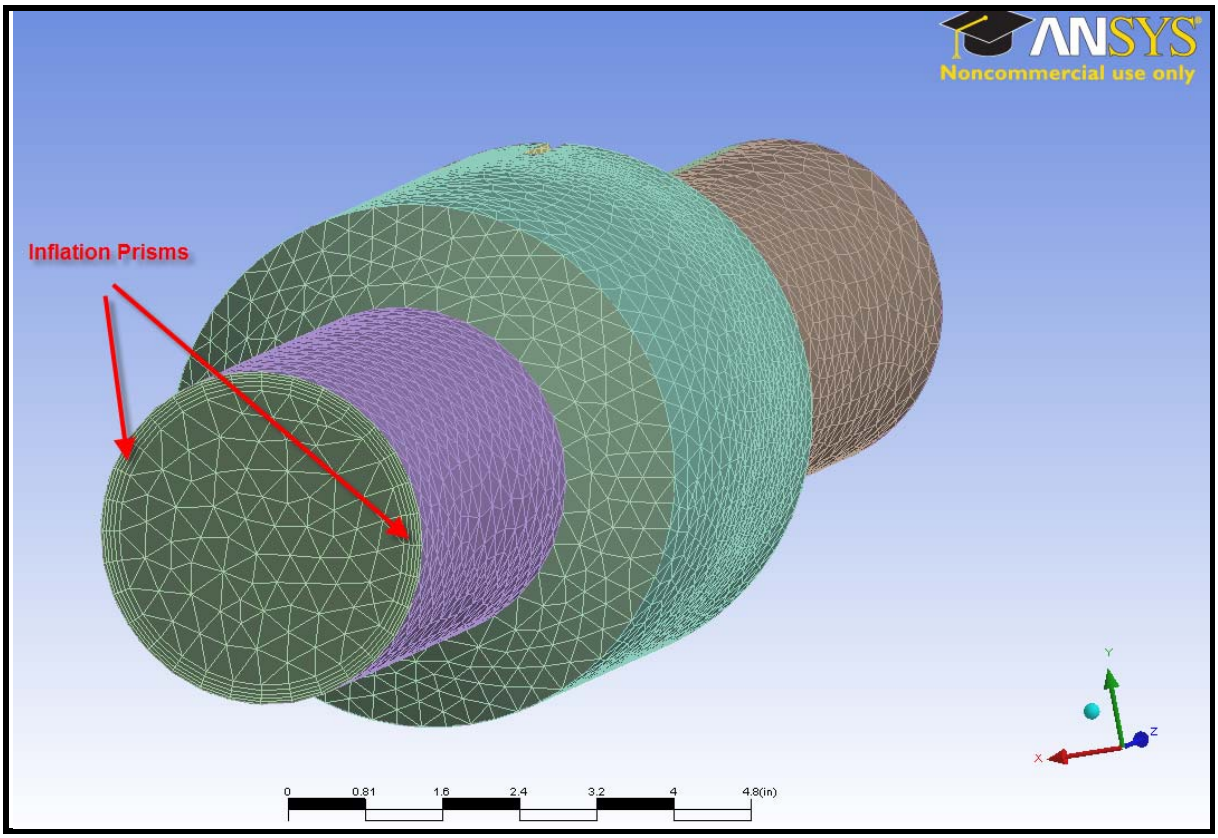


**Figure 3.7 Inflation prisms seen at the inlet surface (25 degrees open)**

**Table 3.5 Quasi-static FSI CFD Mesh Results**

| CFD Mesh Results | 5º | 15 º | 25 º | 35 º | 45 º |
|---|---|---|---|---|---|
| Total # Nodes | 260,886 | 297,189 | 380,312 | 206,453 | 228,492 |
| Total # tetrahedra | 1,223,283 | 1,425,163 | 1,930,091 | 1,035,897 | 1,160,960 |
| Total # Pyramids | 1,294 | 565 | 399 | 507 | 404 |
| Total # prisms | 77,236 | 81,988 | 70,180 | 44,294 | 44,991 |
| Total # elements | 1,301,813 | 1,507,716 | 2,000,670 | 1,080,698 | 1,206,355 |

| CFD Mesh Results | 55 º | 65 º | 75 º | 85 º (open) |
|---|---|---|---|---|
| Total # Nodes | 223,080 | 295,871 | 294,543 | 386,661 |
| Total # tetrahedra | 1,132,529 | 1,473,595 | 1,452,188 | 1,700,016 |
| Total # Pyramids | 382 | 336 | 353 | 1,078 |
| Total # prisms | 44,356 | 66,417 | 70,354 | 135,863 |
| Total # elements | 1,177,267 | 1,540,348 | 1,522,892 | 1,836,957 |

## 3.2.4 Results for Flapper Opening Procedure

The CFD analysis conducted in CFX can be treated as a quasi-static way because the flapper opening process is a difficult and slow process. The simulation results show that for extreme

high pressure (*30,000 psi*) and high temperature (*450°F*) applications, the worst case happens at the beginning of the opening process.

As shown in Table 3.6, assuming a *30,000 psi* reservoir at *10,000 ft* deep and the flapper at a *5-degree* open position, the maximum differential pressure obtained from the front and flapper surfaces (flap_ups and flap_dns) could reach *168 psi*. When the flapper continues to open, the maximum pressure difference decreases slowly. However, because of the increase of region for the flow, the area where maximum pressure acts also decreases in sizes, which if observed in Figure 3.9. The pressure contour plots of the flapper surface show a fast decrease of the red area during the valve opening process.

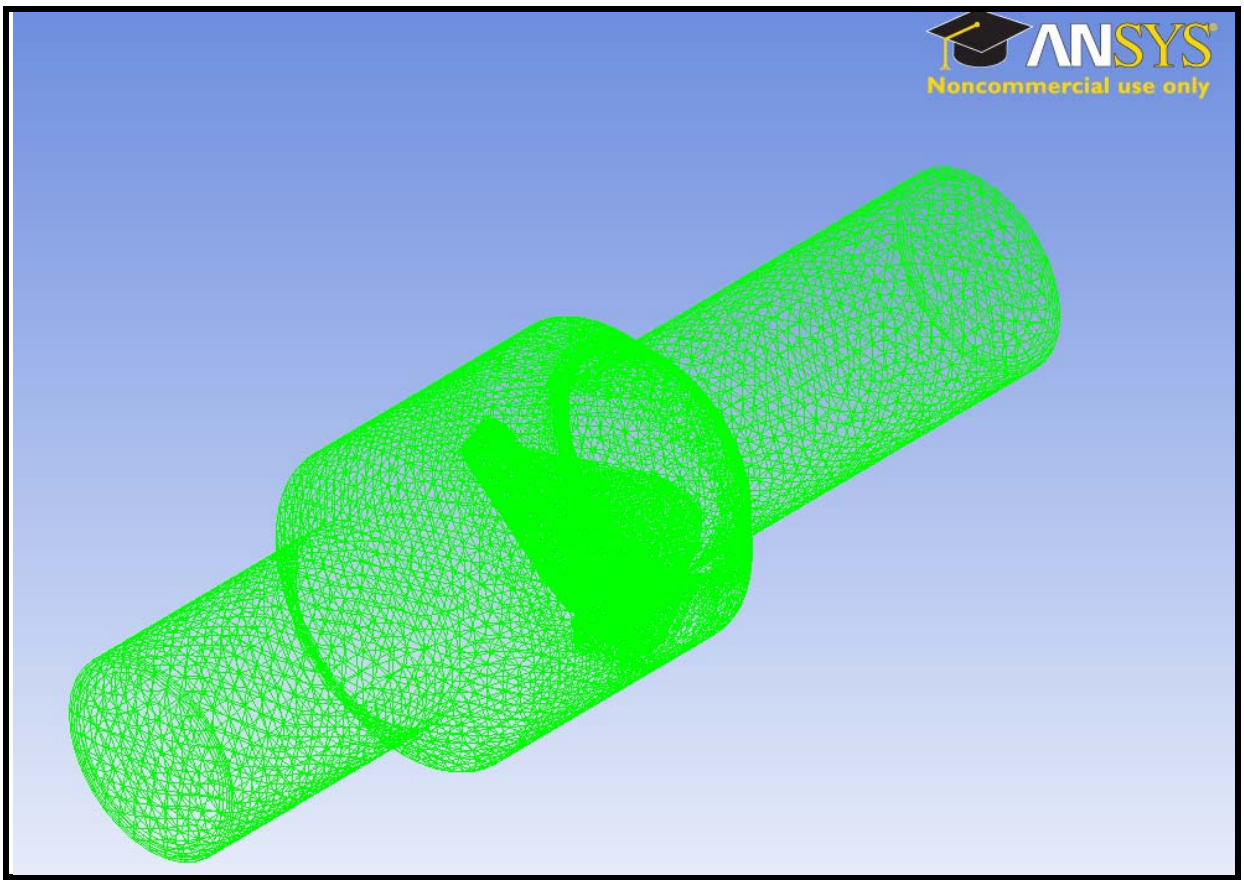


**Figure 3.8 Mesh results for 25-degree open case**

Table 3.7 shows the resistant force change verses the opening degrees of the flapper for reservoirs at *10,000 ft* deep. The resistant force caused by the fluid pressure is calculated by taking the integral of the pressure over the flapper surface. As shown in Table 3.7, the resistant force caused by the fluid pressure is up to *60,407* $lb_f$. Moreover, the resistant force drops dramatically with the further opening process of the flapper for the reason mentioned in the last paragraph. Figure 3.10 shows the resistant force change over the opening process of the flapper

with different reservoir depths. Assuming the same reservoir pressure, typically, the deeper the reservoir, the lower the maximum resistant force is.

At the fully opening (*85-degree* opening case) position, the pressure difference across the flapper front and back face is *-0.1 psi* as shown in Table 3.7. The minus sign shows that the pressure on the inner surface (flap_dns) is larger than on the outer surface (flap_ups). This indicates a pressure against the closure of the flapper exists on certain areas on the flapper. The further integral of the pressure on the flapper surface at fully-opened position shows that the force acting on the flapper is *-17 lbf* as in Table 3.7. Therefore, for a further design, the fail-safe torsion spring on the flapper to activate the closure of the flapper should be included.

In summary, the fluid pressure distribution on the flapper is obtained for further finite element analysis. During the opening process of the flapper, the beginning motion of the flapper will be extreme difficult for a high resistant force caused by the fluid. The flapper has a big chance to "lock up". The high differential pressure across the flapper's front and back face can be extremely high, as calculated from this CFD simulation. If the actuation hydraulic pressures cannot overcome such a high resistant pressure from the reservoir side, the flapper will not be opened and thus "lock up". For further design work, a reliable pressure self-equalizing mechanism or other assistant features, such as magnetic coupling, should be considered to assist or replace the hydraulic actuation. A fail-safe torsion spring should also be included in the design to deal with closure-resistant pressure disturbance.

**Table 3.6 Maximum value of flapper pressure (psi) - reservoir at 10,000 ft**

| Opening angle | 5 º | 15 º | 25 º | 35 º | 45 º | 55 º | 65 º | 75 º | 85 º |
|---|---|---|---|---|---|---|---|---|---|
| Flapupsl (upstream face) | 5145.6 | 820.2 | 395.7 | 281.7 | 239.6 | 203.2 | 147.7 | 73.6 | 23.7 |
| Flapdnsl (downstream face) | 4976.9 | 745.2 | 279.9 | 134.7 | 105.6 | 104.5 | 114.1 | 70.0 | 23.8 |
| Max Differential Pressure | 168.7 | 75.1 | 115.7 | 147.0 | 134.1 | 98.7 | 33.7 | 3.6 | -0.1 |

**Table 3.7 Area integral of flapper pressure (lbf) - reservoir at 10,000 ft**

| Opening Angle | 5 º | 15 º | 25 º | 35 º | 45 º | 55 º | 65 º | 75 º | 85 º |
|---|---|---|---|---|---|---|---|---|---|
| flapupsl | 32180.9 | 4,742.2 | 2,096.6 | 1,331.1 | 1,007.9 | 807.9 | 650.9 | 325.2 | 150.1 |
| flapdnsl | 1977.1 | 623.9 | 522.5 | 388.1 | 330.6 | 289.2 | 268.5 | 161.5 | 159.5 |
| Force Difference* | 60407.7 | 8,236.7 | 3,148.1 | 1,885.9 | 1,354.6 | 1,037.6 | 765.1 | 327.3 | -17.0 |

* Force Difference = (flapupsl-flapdnsl)*2

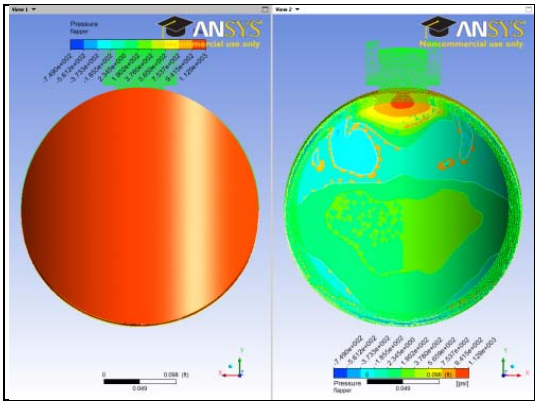

**(a) 5 degree**

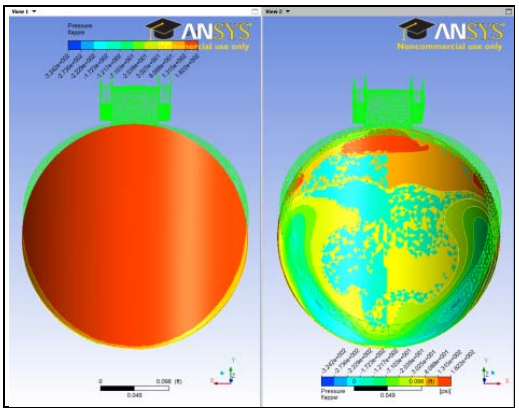

**(b) 15 degree**

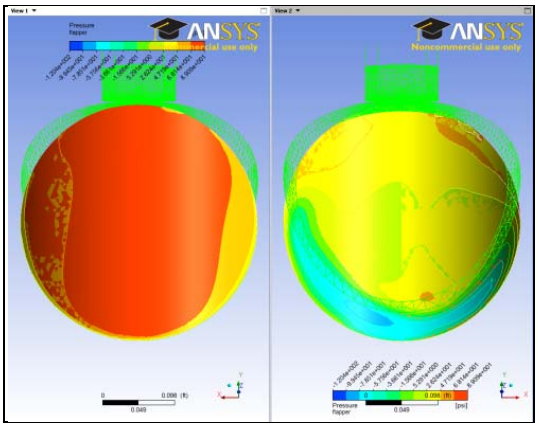

**(c) 25 degree**

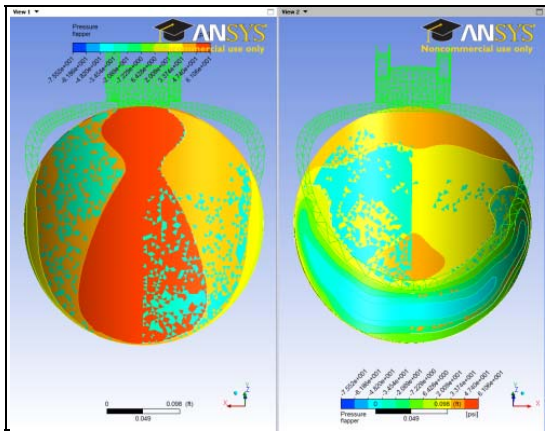

**(d) 35 degree**

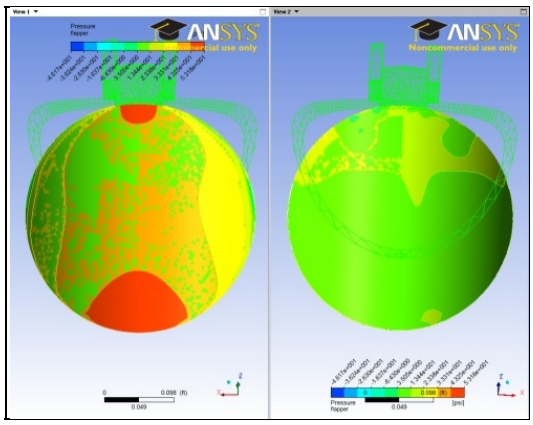

**(e) 45 degree**

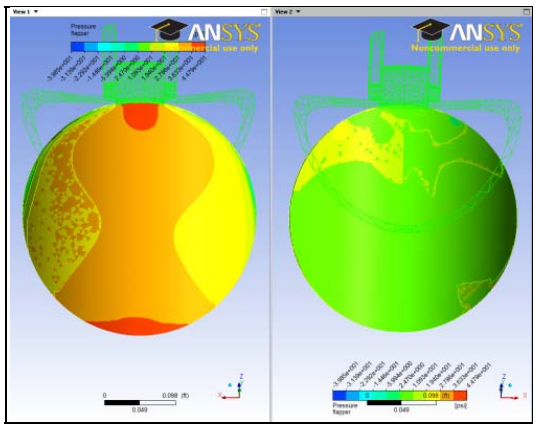

**(f) 55 degree**

**Figure 3.9 Pressure contour on up and downstream faces for reservoir at 10,000 ft**

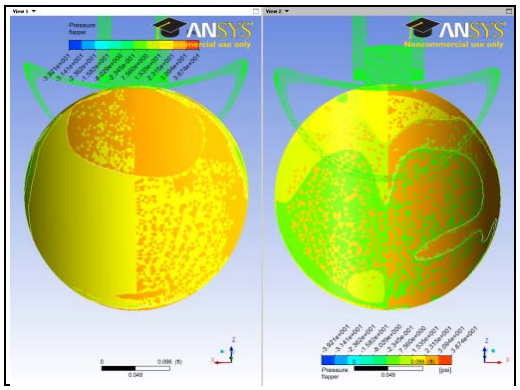

(g) 65 degree

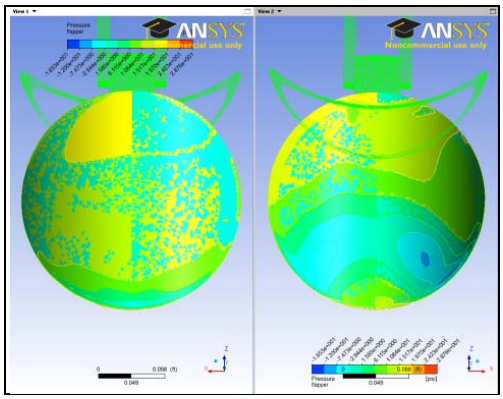

(h) 75 degree

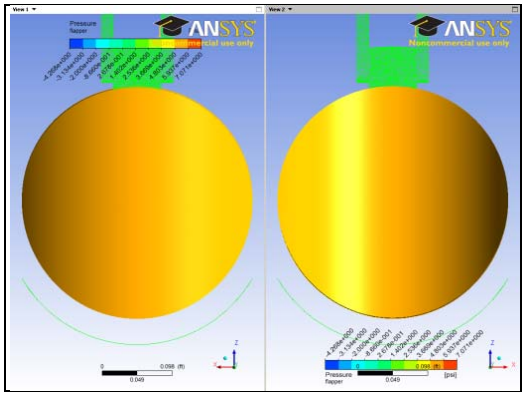

(i) 87 degree (Open)

**Figure 3.9 Pressure contour on up and downstream faces for reservoir at 10,000 ft (continued)**

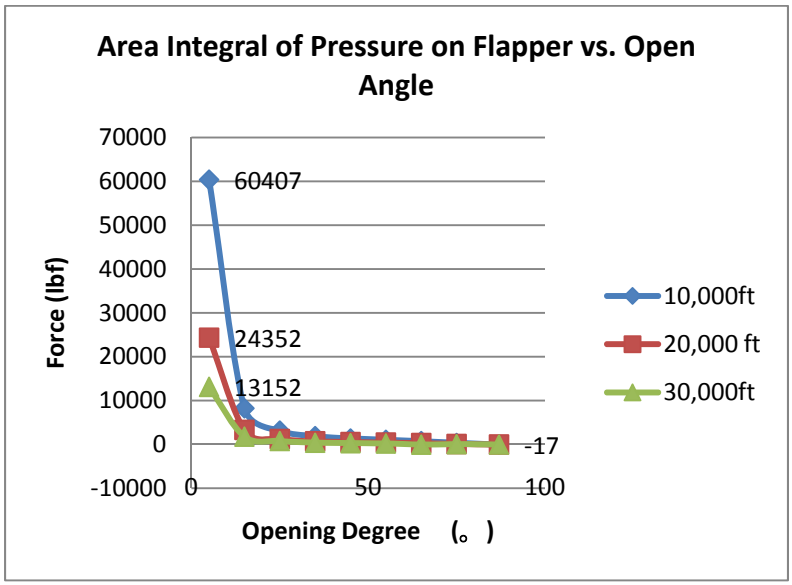


**Figure 3.10 Area integral of pressure across the surfaces of the flapper**

## 3.3 CFD Analysis of Pressure Self-Equalizing SSSV

The quasi-static fluid structure analysis results of a flapper valve reopening process have shown that the reopening after a slam-shut of the flapper will be very difficult. Especially in XHPHT environments, extreme high pressure differences across the flapper can easily cause the overloading of the hydraulic actuator and thus "locking" the valve. Therefore, a pressure relief mechanism should be added onto the flapper to reduce that high pressure difference. The underlining idea of this mechanism is to create a relative small channel through the flapper and let a small amount of fluid flowing through it; thus, the pressure difference across the flapper will decrease dramatically.

In this project, a CFD study has been conducted to evaluate the pressure relief effects with respect to the size of the pressure equalizing channel, or the diameter ***d*** of the channel, through the flapper. The assumptions of the fluid properties and turbulence models are all the same as those for the quasi-static analysis (Eq.3.2 – Eq.3.7), the pipeline hydraulics model is used to obtain the boundary conditions for this study. The reservoir is assumed to be a *30,000 psi* reservoir at *30,000 ft* deep and the flapper SSSV is placed *2,000 ft* below sea level. The diameter of the production pipe is *3.5 in*.

### 3.3.1 Fluid Domains

It is reasonable to assume that the fluid pressure from the reservoir side remains constant while a cylindrical channel has been created through the flapper. The downstream side pressure will increase and thus the pressure difference across the flapper is decreased. Also, utilizing the symmetry of the pipe flow, the fluid domain is obtained and shown as follows. Figure 3.11 shows a fluid domain with a cylindrical channel with diameter *d = 0.2cm (0.08 in)*, the fluid domain consists of two parts, the channel through the flapper and the downstream fluid domain. The flapper thickness is *0.6 in, and* so is the length of the channel. The diameter of the downstream fluid domain is *3.5 in*. The length of the downstream domain is *30 in*.

### 3.3.2 Boundary Conditions

Assuming the reservoir is at 30,000 ft deep and the flapper valve is set at 2,000 ft deep, from (3.3), the static pressures on both sides of the flapper before pressure equalizing are listed in Table 3.8. In order to give the correct boundary conditions for the CFD analysis, the inlet mass flow rates are calculated from the pressures in Table 3.8 and the pipeline hydraulic models introduced in Section 3.1 (Eq.3.2, Eq.3.3, and Eq.3.7) with respect to different channel diameters. The results are listed in Table 3.9. The mass flow rates are applied as an inlet boundary condition for each case, and the outlet boundary conditions are set with a zero average static pressure.

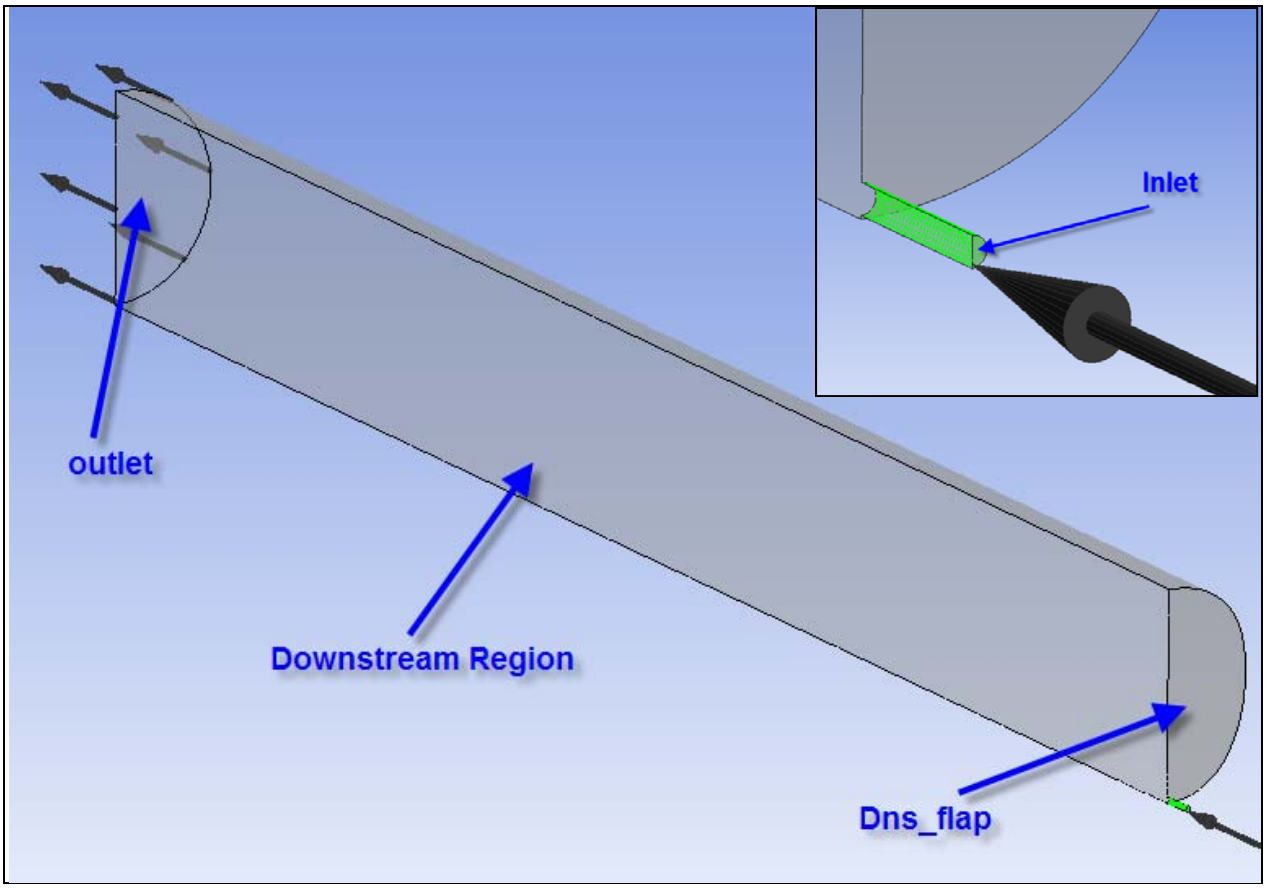


**Figure 3.11 Fluid domain for a pressure equalizing flapper**

**Table 3.8 Pressure Difference Across the Flapper Before Pressure Equalizing**

| Upstream (Reservoir) side | Downstream side | Original Pressure Difference |
|---|---|---|
| *20,380 psi* | *687 psi* | *19,693 psi* |

**Table 3.9 Mass flow rate calculated with respect to different passage diameter**

| Passage Diameter *cm (in)* | Re | friction No. | Mass Flow Rate* *lbm/s* |
|---|---|---|---|
| *0.05(0.02)* | *5.73E+04* | *0.0201* | *0.025* |
| *0.1(0.04)* | *1.80E+05* | *0.01582* | *0.154* |
| *0.15(0.06)* | *3.57E+05* | *0.01389* | *0.463* |
| *0.2(0.08)* | *5.68E+05* | *0.0127* | *0.974* |
| *0.25(0.10)* | *8.29E+05* | *0.01196* | *1.794* |

* Mass flow rate for half area of the channel

## 3.3.3 Mesh Facts

For different channel diameters shown in Table 3.9, a total of five fluid domains have been meshed and analyzed. Figure 3.12 shows mesh results for the case where a through-valve passage with a diameter of *0.1cm (0.04in)* is created. Highly refined mesh is achieved near the inlet of the tiny inlet channel. Table 3.10 shows the mesh facts for all the five cases.

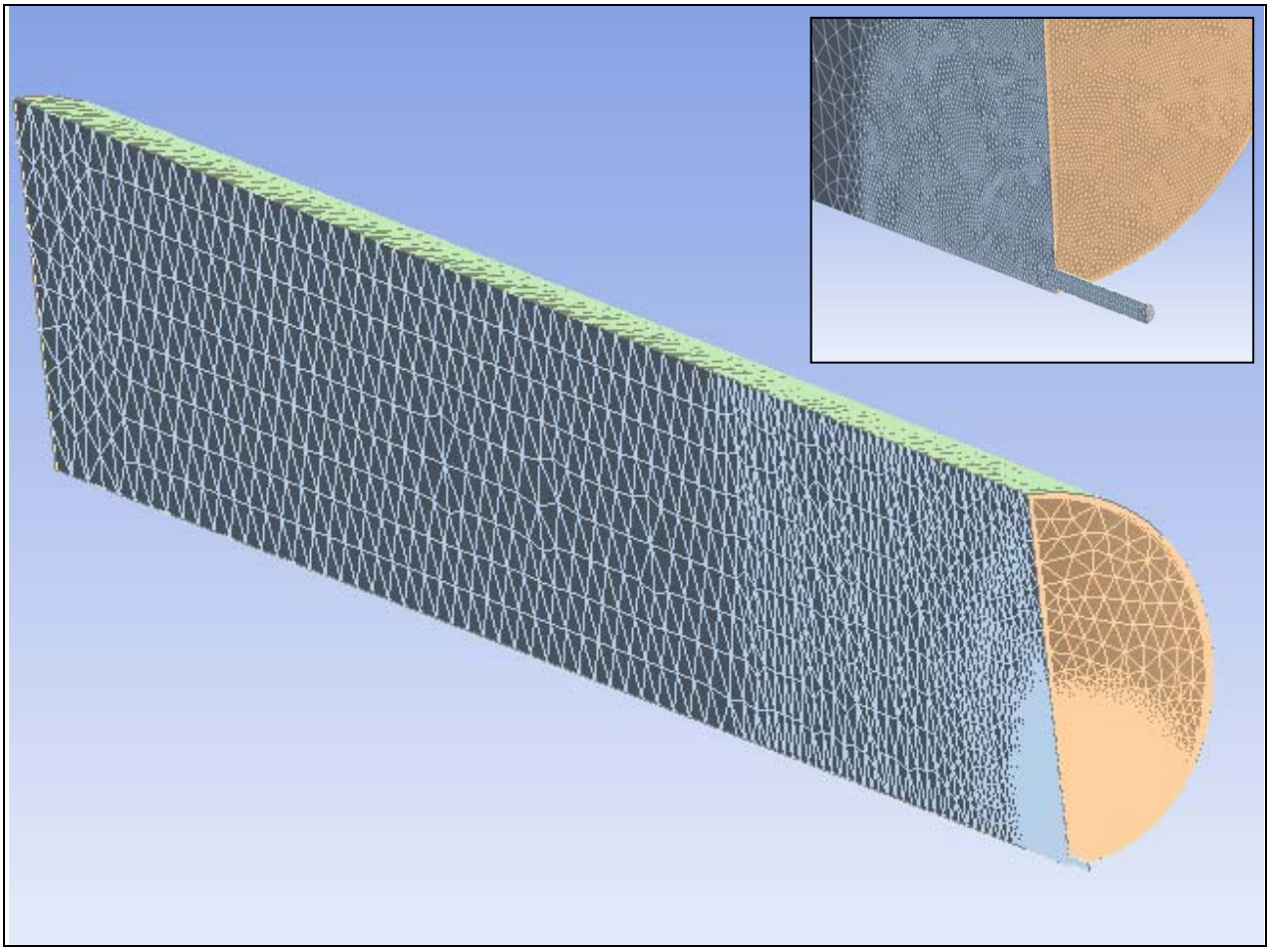

**Figure 3.12 Mesh facts for pressure equalizing passage diameter of 0.25cm**

**Table 3.10 Mesh Facts for CFD Study of Pressure Equalizing Flapper**

| **CFD Mesh Results** | ***0.05 cm*** | ***0.1cm*** | ***0.15cm*** | ***0.2 cm*** | ***0.25 cm*** |
|---|---|---|---|---|---|
| **Total # Nodes** | *83,884* | *285,798* | *287,896* | *287,287* | *286,734* |
| **Total # tetrahedra** | *294,709* | *1,328,486* | *1,331,999* | *1,330,721* | *1,329,342* |
| **Total # Pyramids** | *209* | *316* | *477* | *365* | *324* |
| **Total # prisms** | *57,921* | *100,165* | *103,027* | *102,381* | *102,088* |
| **Total # elements** | *352,839* | *1,428,967* | *1,435,503* | *1,433,467* | *1,431,754* |

### 3.3.4 Results for Pressure Self-Equalizing Mechanism

The CFD results have been post-processed to obtain the total pressure on both the *Dns_flap* and the *Inlet* regions, as shown in Figure 3.11. The pressure equalizing results are summarized in Table 3.11 as follows. With the help of a pressure self-equalizing mechanism, the CFD analysis has shown that the pressure difference across the flapper can be reduced significantly. With the assumptions that the reservoir is at *30,000 ft* deep with a pressure of *30,000 psi*, the SSSV stays at *2,000 ft* deep within a *3.5in* production pipe. The results show that reduction factor can reach from around *44%* to *80%*. The maximum pressure equalizing effects happens when the diameter of the passage is in the range of *0.04 in (0.1cm)*.

**Table 3.11 Reduced Pressure Results from the CFD Analysis for a Pressure Equalizing Flapper**

| Passage Diameter | Total Pressure | | Equalized Pressure Difference | Reduction Factor* |
|---|---|---|---|---|
| | Inlet | Dns _Flap | | |
| *cm (in)* | *psi* | *psi* | *psi* | |
| *0.05(0.02)* | *8,826* | *0.07* | *8825.93* | *55%* |
| *0.1(0.04)* | *4,003* | *1.58* | *4001.42* | *80%* |
| *0.15(0.06)* | *5,716* | *47* | *5669* | *71%* |
| *0.2(0.08)* | *8,308* | *-4.9* | *8312.9* | *58%* |
| *0.25(0.10)* | *10,980* | *-12* | *10992* | *44%* |

* 1- Equalized Pressure Difference/ Original Pressure Difference in Table 3.8

# Chapter 4

# Water Hammer Analysis

*In this Chapter, the pressure surge caused by a sudden closure of the flapper has been analyzed with one-dimensional water hammer equations.*

## 4.1 Problem Description

Water hammer is known as the pressure transients caused by the sudden closing or opening of the valve in a pipeline. The sudden closure of the valve can result in huge pressure peak, while the sudden opening of the valve can cause extreme low pressure. Both water hammer phenomena can cause damage to the pipe as well as the valve. In a production string, a subsurface safety valve (SSSV) functions as a fail-safe component. It will shut off the pipe when the actuator, usually powered by a spring, raises the upper tubular sleeve in emergencies. It is also required to test the SSSV twice a year during its twenty-year operation lifetime. The closing process of a SSSV completes within a tenth of a second according to our RPSEA contacts. This sudden closure of the SSSV could cause the flapper to fail to seal off the pipe, e.g. by plastic deformation, rupture etc. The pressure surge also contributes to impact the valve and pipe system causing a low cycle fatigue problem. In this Chapter, the water hammer problem of the SSSV will be studied using one-dimensional water hammer model. Different materials will be tested. Two assumptions about the closure of the SSSV are made, instantaneous closure and closure over a finite time period. The calculation is done with an online water hammer calculator developed by LMNO Engineering, Research and Software Ltd. (2009). REF

## 4.2 One-Dimensional Water-Hammer Analysis

The designed diameter of the SSSV for the production string is the smallest diameter permitted by the industry, which is *3.5 in*. The length of the production string from ultra deep reservoir to the installation location of the SSSV is at least *2,000 ft* by the former assumptions (i.e. reservoir at *10,000 ft* depth and SSSV at *8,000 ft* depth). Since the diameter of the pipe compared to the length of the pipe is very small, it is reasonable to adopt a one-dimensional water hammer model for the SSSV case. The flow in the one-dimensional water hammer model is assumed to be essentially axial along the pipe. The radial fluxes of mass, momentum and energy are negligible compared to their axial counterparts.

For one-dimensional water hammer analysis, two different types of equations will be applied depending on whether the flow is treated as steady or unsteady, or in terms of the time it takes to

close the SSSV in the production pipe. If the valve is closed instantaneously, then flow is assumed steady. If the time period of the valve closure process is not negligible, the flow will be treated as unsteady flow. Hwang and Houghtalen (1996) found that if the valve closure time is less than $2L/c$, where $c$ is the fluid wave speed, instantaneous model could be adopted. Otherwise, time variable cannot be ignored.

**(1) Instantaneous Closure ($t \leq 2L/c$)**

Instantaneous closure water hammer can be solved with the fundamental equation for transient flow problems, which was developed by Joukowsky (Ghidaoui et al. 2005) as follows,

$$\Delta \boldsymbol{P} = \boldsymbol{\rho c \Delta V} \tag{4.1}$$

Where $c$ is the wave speed, $\rho$ is the fluid density, $V$ is the cross-sectional average velocity and $P$ is the piezometric pressure. Joukowsky's fundamental equation is based on several assumptions of the flow condition. It assumes a one-dimensional steady flow, filling the whole pipe. The flow is incompressible and frictionless. The flow velocity drops to zero instantaneously as the closure of the valve. The negative sign will be added if the pressure surge travels upstream (i.e., the tubular side connects the reservoir). The fundamental equations only consider the upstream effects of the water hammer; the downstream side is not included. The wave speed $c$ can be obtained as follows,

$$\boldsymbol{c} = \sqrt{\frac{\boldsymbol{E}}{\boldsymbol{\rho}}} \tag{4.2}$$

Where $E$ is the equivalent elastic modulus calculated as follows,

$$\frac{\mathbf{1}}{\boldsymbol{E}} = \frac{\mathbf{1}}{\boldsymbol{E_f}} + \frac{\boldsymbol{D}}{\boldsymbol{wE_p}} \tag{4.3}$$

The first term on the right-hand side reflects the elasticity modulus $E_f$ of the fluid. $E_f$ is the reciprocal of fluid compressibility. The second term reflects the elasticity contribution of the pipe. It comes from the thin-walled pipe assumption. $E_p$ is the pipe elasticity modulus, $D$ is the inside diameter of the pipe, and $w$ is the pipe wall thickness.

**(2) Finite Time Closure ($t > 2L/c$)**

Compared to instantaneous closure, finite time closure is a little more complicated since the time variable is included. However, the general idea is the same. The conservation laws across the pressure surge should be fulfilled. Typically, a control volume is assumed to include the pressure surge, then the mass and momentum conservation laws are applied on the control volume. The resulting equations are as follows for one-demensional flow (Bergant 2006),

$$\frac{\partial \boldsymbol{P}}{\partial \boldsymbol{t}} + \boldsymbol{\rho c^2} \frac{\partial \boldsymbol{V}}{\partial \boldsymbol{x}} = \mathbf{0} \tag{4.4}$$

$$\frac{\partial \boldsymbol{V}}{\partial \boldsymbol{t}} + \frac{\mathbf{1}}{\boldsymbol{\rho}} \frac{\partial \boldsymbol{P}}{\partial \boldsymbol{x}} + \frac{\mathbf{4}}{\boldsymbol{\rho D}} \boldsymbol{\tau_w} = \mathbf{0} \tag{4.5}$$

where $\tau_w$ is the shear stress on the pipe wall. These equations assume quasi-steady wall conditions, which uses the shear stress expression from steady problems for an unsteady problem. The shear stress $\tau_w$ can be approximated in the Darcy-Weisbach equation as follows,

$$\boldsymbol{\tau_w = \frac{\rho f(t)|V(t)|V(t)}{8}} \tag{4.6}$$

Where $f(t)$ is the Darcy-Weisbach friction factor. Substitute (4.6) into (4.5), the final momentum equation is as follows,

$$\boldsymbol{\frac{\partial V}{\partial t} + \frac{1}{\rho}\frac{\partial P}{\partial x} + \frac{f|V|V}{2D} = 0} \tag{4.7}$$

Therefore, (4.4) and (4.7) consist of the governing equations for the one-dimensional water hammer problem where finite time closure of the valve is assumed.

## 4.3 Water Hammer Results and Discussion

The closure process of subsurface safety valve can be really quick, usually within a tenth of a second. Water hammer pressure surge is calculated for both cases, i.e., instantaneous closure and finite time valve closure, for comparison. The calculation is conducted numerically with finite difference techniques.

### (1) Results for Instantaneous Closure

The setting depth of the subsurface safety valve does not affect the water hammer estimation in this case. The velocity change is estimated using the maximum velocity for each reservoir depth as assumed in Chapter 3. Three structural materials have been used as the pipe material. Table 4.1 shows the pressure surge calculated from the LMNO calculator (LMNO Ltd. 2009) for instantaneous valve closure pressure.

**Table 4.1 Instantaneous Closure Water Hammer Pressure Surge**

| Instantaneous Closure Water Hammer Pressure (psi) | | Reservoir Depths and Maximum Velocity Vmax | | |
|---|---|---|---|---|
| | | 10,000' Vmax = 139.6 ft/s | 20,000' Vmax = 89.3ft/s | 30,000' Vmax = 65.8ft/s |
| Pipe Material | Inconel® 718 (Ep = 30,600 ksi) | 2,965.82 | 1,897.70 | 1,398.91 |
| | Duplex Stainless Steel (Ep = 29,000 ksi) | 2,961.60 | 1895.18 | 1,397.06 |
| | Aermet® 340 (Ep = 27,900 ksi ) | 2,958.91 | 1893.28 | 1,395.65 |

Under the same reservoir pressure assumption, the water hammer pressure surge decreases with the increasing depth of the reservoir. The water hammer pressure surge also will decrease for a more flexible pipe material (with lower elasticity modulus). The maximum water hammer pressure surge found was when the reservoir is at *10,000 ft* depth with a pipe built from Inconel® 718. The highest pressure surge is *2,965.82 psi* as shown in the table.

### (2) Results for Finite Time Closure

The finite time closure water hammer pressure calculation is also based on the reservoir depths and subsurface safety valve depths assumed in Chapter 4. The time for the closure is assumed to be *0.1 s*. Inconel® 718 is selected for the pipe material. Therefore, the water hammer pressures are calculated as in Table 4.2.

**Table 4 2 Finite Time Closure Water Hammer Pressure Surge**

| Finite Time Closure Water Hammer Pressure (psi) | | Reservoir Depths & Flow Rate Q | | |
|---|---|---|---|---|
| | | 10,000' Q = 8.077 $ft^3/s$ | 20,000' Q = 5.139 $ft^3/s$ | 30,000' Q = 3.775 $ft^3/s$ |
| SSSV Depth (ft) | 2,000 | 907.13 | 687.08 | 687.08 |
| | 5,000 | 1,937.75 | 1,717.70 | 1,717.70 |
| | 8,000 | 2,968.37 | 2,748.32 | 2,748.30 |

### (3) Pressure Surge Discussion

The pressure surge calculated from the LMNO calculator for finite time closure model is generally smaller than the instantaneous closure results. Therefore, the results from the instantaneous closure cases are the worst-case scenario estimation for water hammer pressure surge. To look at worst case scenarios, the pressure surge calculated from the instantaneous closure results will be adopted and applied as an pressure loading for the elasto-plastic impact analysis. That is, the water hammer study is judged to be less accurate than the three-dimensional CFD results for peak pressure transients.

# Chapter 5

# Finite Element Stress Analysis

*In this Chapter, the finite element analysis of the stresses is conducted based on the fluid pressure distribution obtained from the quasi-static FSI analysis. The impact at the slam-shut of the flapper is addressed and a parametric study to optimize the flapper shape is followed.*

## 5.1 Commercial Software Tools

This project is conducted with what the ASME BPVC describes as a design-by-analysis fashion. Therefore, suitable numerical simulations need to be built. Among all the most used numerical methods in the realm of engineering design, the finite element method (FEM) (Akin 1994) or finite element analysis (FEA) has incomparable advantages with respect to representing complex geometry. Finite element analysis approximates the solution of interest by first breaking up a complex structure or geometry into small sub-domains with regulated shapes, or the so-called elements. Each element is connected to each other with shared nodes. Then the governing equations or the integral form of the governing equations are solved for the nodal values, the solution within any element can be obtained by interpolation of its consisting nodal valves.

In this study, the finite element analysis for the stresses of the subsurface safety valve is carried out by using both *Ansys® Workbench v 12.0* (2009) and *SolidWorks 2009* (Akin 2010).

A preliminary linear elastic contact analysis is first carried out with Ansys® Workbench. The CAD models used in finite element analysis are identical to those used in the computational fluid dynamics before. Therefore, fluid pressures could be further mapped accurately onto the corresponding flapper surfaces as pressure loadings. The stress results indicate a plastic deformation occurs on the flapper.

Therefore, a nonlinear elasto-plastic FEM analysis is then carried out in SolidWorks. The flapper geometry is modified and a follow-up parametric study to lower the stress and strain level has been conducted in SolidWorks.

*SolidWorks* is the 3D CAD software used for CAD modeling for this project. *SolidWorks* also has its own analysis component called SolidWorks Simulation, which is a powerful design tool with both linear and nonlinear FEA analysis capabilities.

## 5.2 Linear Elastic Contact Analysis in Ansys® Workbench v12.0

### 5.2.1 FEM Pre-processing

#### (1) Importing Geometry

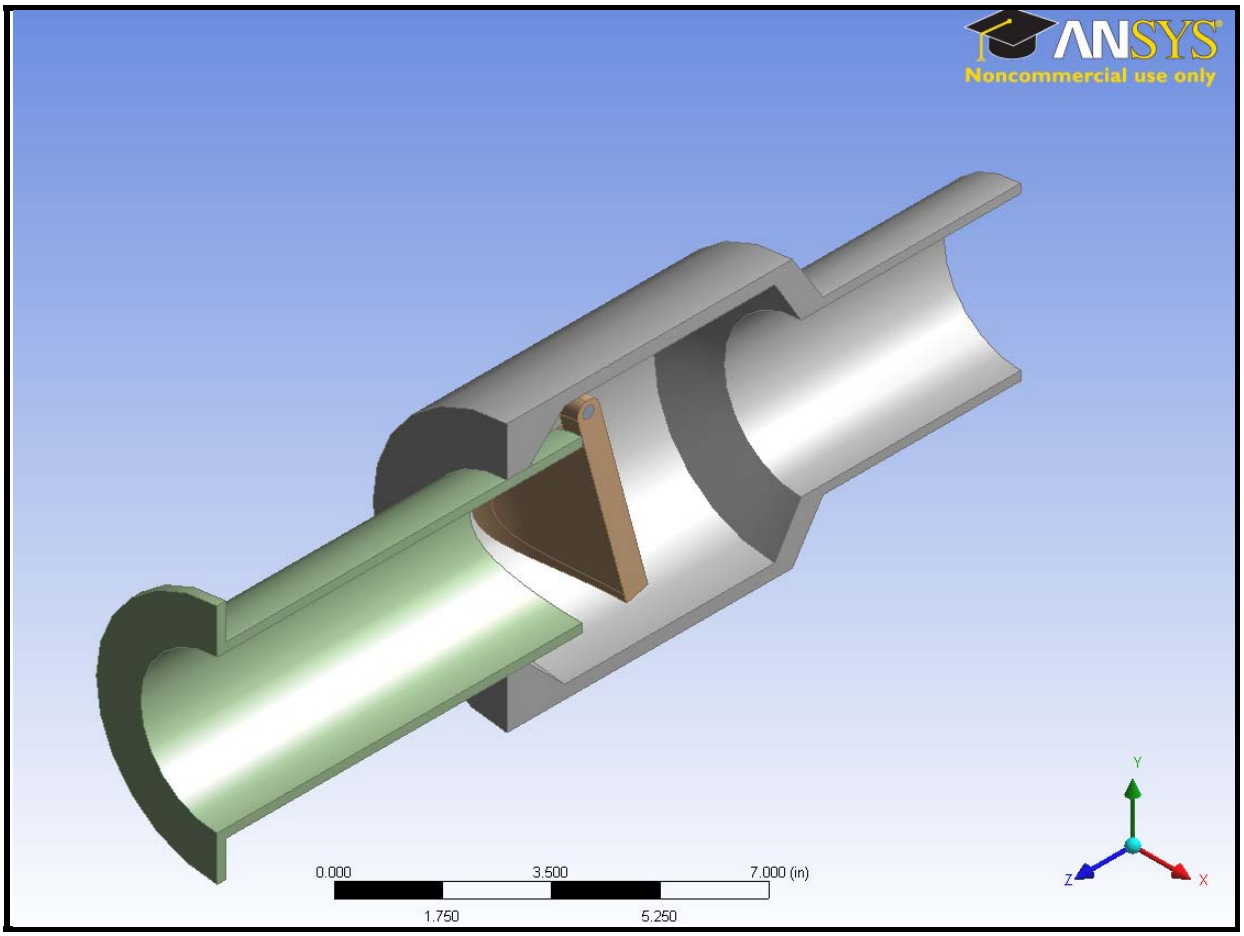


**Figure 5.1 Imported half geometry model of flapper assembly (15-degree Open)**

In Figure 5.1, it is seen that four main parts of the flapper assembly have been imported successfully, namely, the flapper, hinge-pin, sleeve tube and the flapper chamber. The flapper chamber has been treated as a rigid body for two reasons. First, the main focus of this FEA study is the stress and strain response of the flapper and sleeve tube, especially around the contact region between sleeve tube and the flapper. The deformation and the stress level of the flapper chamber are of less concern compared to that. Second, the educational edition of Ansys® Workbench v12.0 in use has an upper limit on node numbers; rigid body treatment of the flapper chamber could save nodes for a refined mesh at the contact region between sleeve tube and the flapper.

## (2) Contact Settings

The contact regions between each flapper valve component are automatically detected by Ansys® Workbench when the CAD model is imported. There are five contact types available in the Workbench for face, node and edge contacts: bonded, no separation, frictionless, rough, and frictional. The differences of the five contact types are summarized in Table 6.1. For this quasi-static stress analysis, only bonded and no separations types are used.

**Table 5.1 Contact Types in Ansys® Workbench v12.0**

| Contact Types | Properties |
|---|---|
| Bonded | No sliding and separation, glue together |
| No Separation | No separation, but small frictionless sliding allowed |
| Frictionless | Free sliding, separation happens when contact pressure equals zero |
| Rough | Perfect frictional contact, no sliding, separation happens when contact pressure equals zero |
| Frictional | Frictional factor required, sliding happens after shear stress up to a certain magnitude |

The underlying formulation methods for solving contact problems in Workbench v12.0 are available in four main kinds, such as Augmented Lagrange, Pure Penalty, Multi-point Constraint (MPC) and Normal Lagrange. For this study, contacts are either edge-to-surface or surface-to-surface contacts. The contact effects between sleeve tube and flapper need to be accurately evaluated while no-penetration condition should be satisfied. Therefore, MPC is first not suitable for this study where the contact based results will be zero, such as contact pressure. For pure penalty methods, the no penetration condition is satisfied by setting contact stiffness matrix to be infinite large, which can not be fully satisfied with numerical solutions, thus is less accurate. The Augmented Lagrangian method is actually a penalty method with penetration control. Thus, no-penetration condition is hardly satisfied using Augmented Lagrangian method. For this study, the normal Lagrangian method is used to solve for the contact problem. The Normal Lagrangian method satisfies the no-penetration condition without dealing the contact stiffness matrix. A Lagrangian multiplier is used on the normal direction between contact surfaces and a penalty method is used in the tangential direction. Thus no-penetration condition should be strictly satisfied. The contact settings for this finite element analysis are set as follows,

**Table 5.2 Contact Settings in the Static Stress Analysis of the Flapper Valve**

| Contact Sets | Contact Types | Formulations |
|---|---|---|
| Flapper and Sleeve Tube | Bonded/No Penetration | Normal Lagrangian |
| Flapper and Hinge-pin | No Penetration | Normal Lagrangian |
| Flapper and Chamber | No Penetration | Normal Lagrangian |
| Hinge-pin and Chamber | No Penetration | Normal Lagrangian |
| Sleeve Tube and Chamber | No Penetration | Normal Lagrangian |

## (3) Element Types and Mesh Results

For this quasi-static stress analysis, two types of elements are needed- solid body elements and contact surface elements. The body elements used in Workbench is SOLID187 [30], a three-dimensional (3D) 10-node tetrahedral structural element. This type of quadratic elements can promise a well-shaped mesh on even the most complicated geometries. For the contact regions, Workbench uses CONTA174 (ANSYS Workbench 2009), a 3D 8-node surface-to-surface contact element. A CONTA 174 located between the surface of a solid element or shell element and shares the same geometric characteristics of the connected element faces. Mesh controls of the contact areas between sleeve tube and flapper, flapper and hinge-pin have been made to achieve a highly refined mesh resolution there. The mesh results are listed in Table 5.3, the total number of the nodes for each case is controlled under 30,000, because of the node limitation of the non-commercial Workbench. One of the mesh results for the case of *15-degree* open angle is shown in Figure 5.3. There the sleeve tube contacts the flapper at the inner center part close to the hinge-pin, highly refined meshes with an element size around *0.1 in* are achieved. The hinge-pin is the second place that requires a refined mesh. Mesh control is set to be *0.05 in*. For the other cases, mesh results are quite similar. Details are omitted to avoid redundancy. Figure 6.4 shows the mesh results for the fully closed case, the sleeve tube is connected to the flapper in this case; therefore, the refined meshes are at the sealing circle around the edge of the flapper, and the mesh at the hinge-pin is also refined in this case, with a 0.05 in mesh control as in other cases.

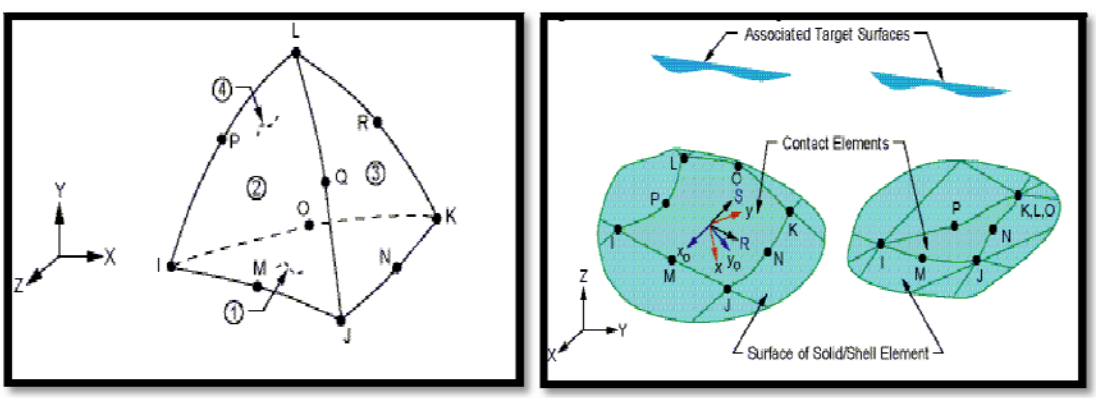


**Figure 5.2 SOLID187 and CONTA174 element illustrations**

**Table 5.3 Mesh facts for the quasi-static stress analysis**

| **Open Angle** | **5 º** | **15 º** | **25 º** | **35 º** | **45 º** |
|---|---|---|---|---|---|
| Nodes | 20,634 | 12,451 | 20,471 | 20,936 | 18,280 |
| Elements | 10,848 | 5,572 | 11,763 | 12,060 | 10,337 |
| **Open Angle** | **55 º** | **65 º** | **75 º** | **Fully Open** | **Fully Closed** |
| Nodes | 18,739 | 25,760 | 20,583 | 9,644 | 22,748 |
| Elements | 10,666 | 14,138 | 117,565 | 4,585 | 11,978 |

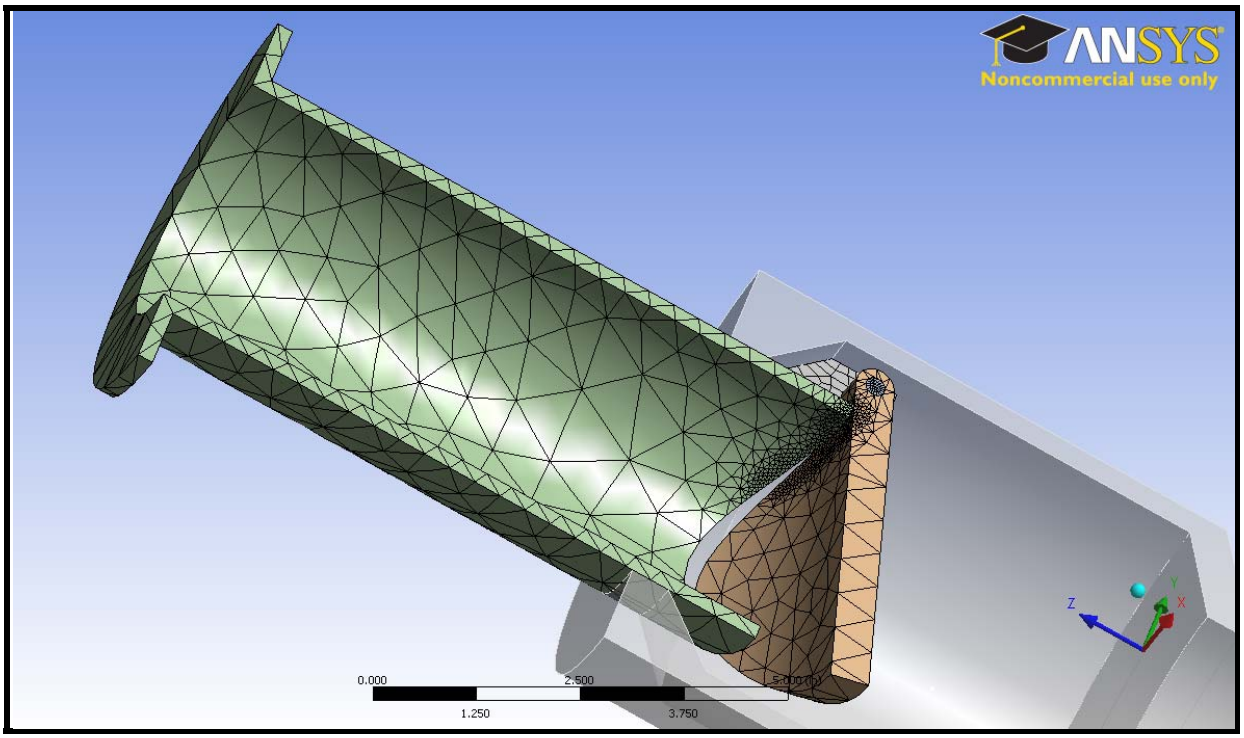


**Figure 5.3 Mesh viewof 15-degree open case**

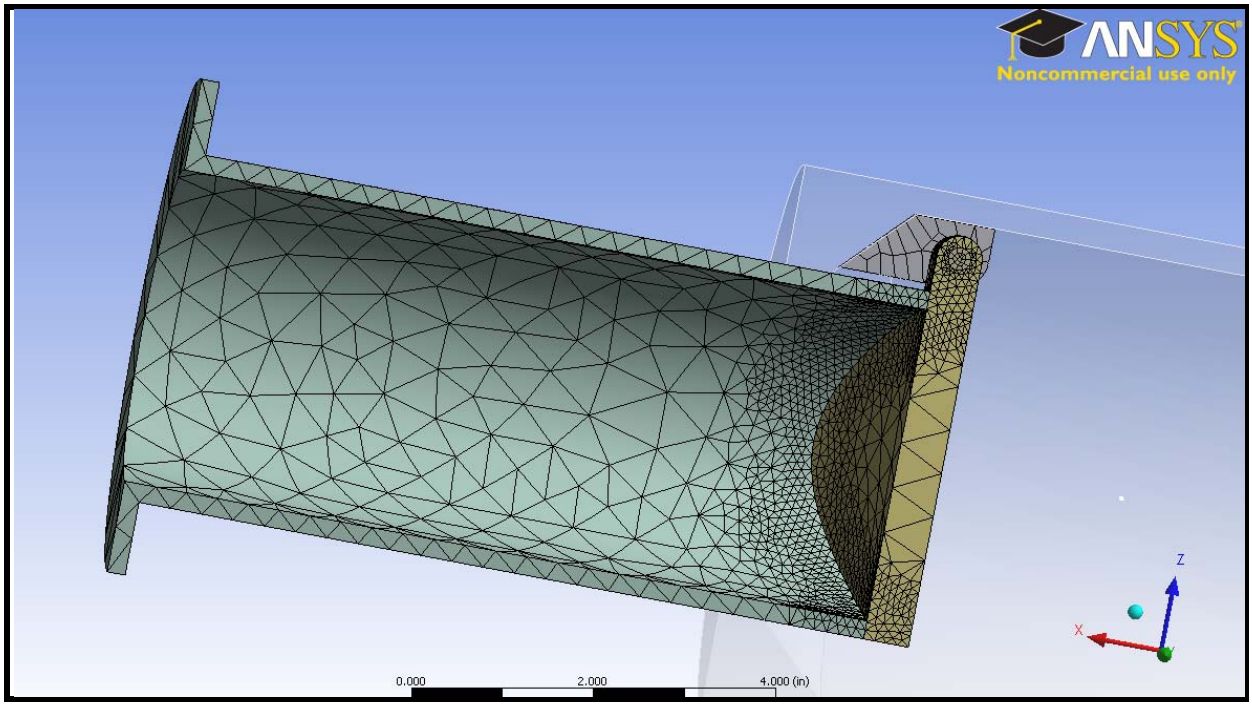


**Figure 5.4 Mesh view of fully closed case**

## (4) Material Selection

Without consideration of the cost of the material, INCONEL®718 is selected for this study both for its popularity in oil and gas industry and also its available mechanical properties. For comparison, duplex stainless steel and Aermet® alloy are also selected for the contact analysis.

## (5) Static Stress Boundary Conditions

Two types of boundary conditions are set for the static stress analysis- symmetric conditions and fixed boundary conditions. The boundary conditions for the *35-degree* open case are set as in Figure 5.5. They are applied on the top of the sleeve tube and two ends of the flapper chamber. The symmetric boundary conditions for the same case are set as in Figure 5.6. The normal displacements of the symmetric faces are set to zero.

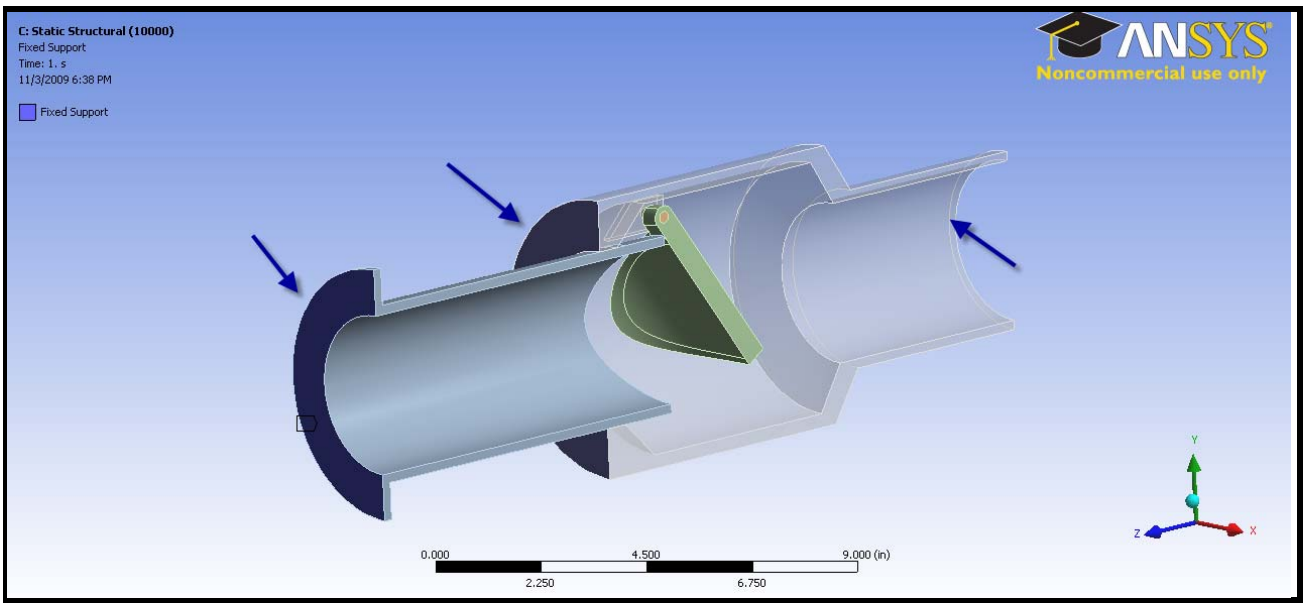


**Figure 5.5 Fixed boundary conditions (35 degree open)**

## (6) Pressure Loadings

The fluid pressure results obtained from the *Ansys® CFX v12.0* can be mapped into Workbench as imported pressure loading for the static stress analysis. For all nine opening flapper angles, the pressure acting on the flapper is imported onto three faces (named flapupsl, flapdnsl, and flapsdl). One of the mapping results for a *35-degree* open case is shown in Figure 5.7. The peak pressure imported is *269 psi* compared to a value of *282 psi*. For the case where the flapper is fully opened, additional pressure mappings onto the sleeve tube are conducted. The pressure mapping results projected onto the sleeve tube is shown in Figure 5.8. The peak pressure imported is *5 psi* compared to a value of *33 psi*.

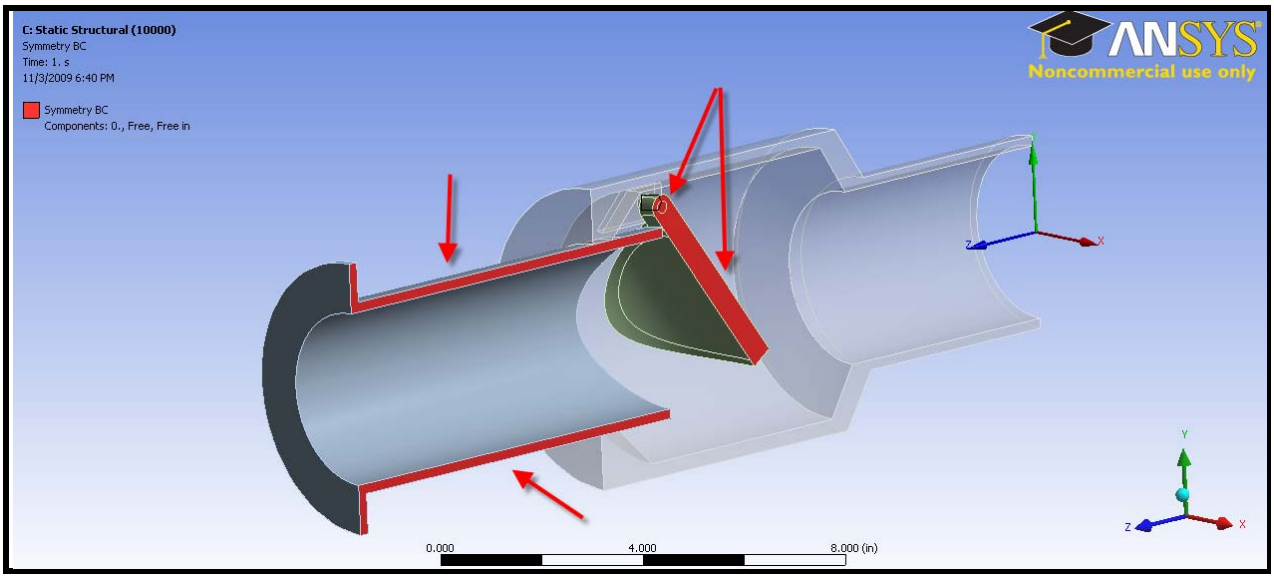


**Figure 5.6 Symmetric boundary conditions (35 degree open)**

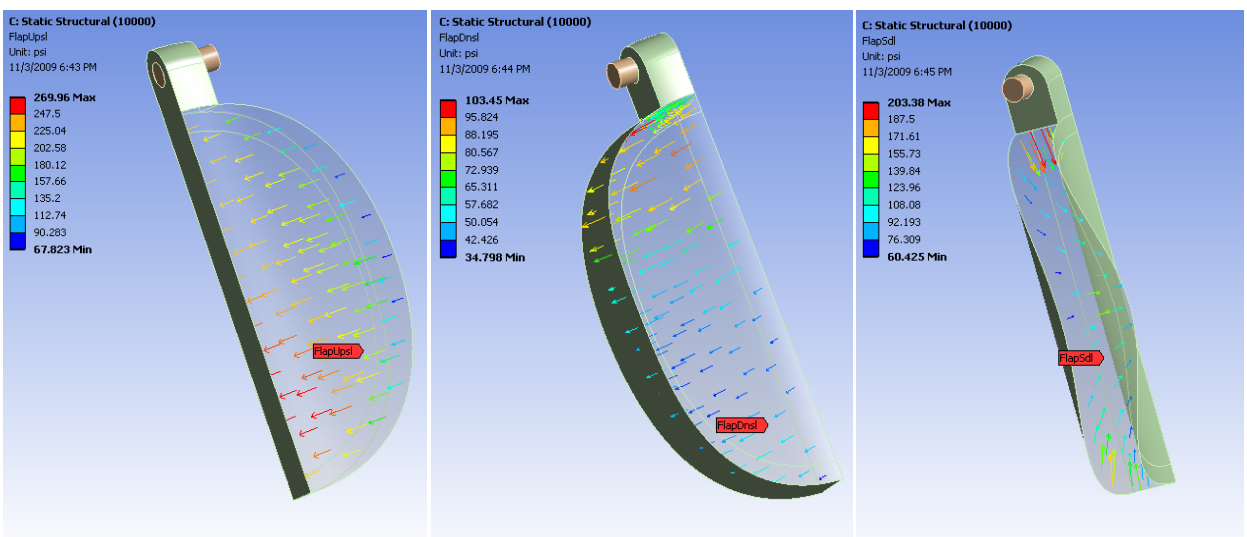


**(a) Flapupsl** **(b) FlapDnsl** **(c) FlapSdl**

**Figure 5.7 CFX pressure mapping on the flapper (35 degree open)**

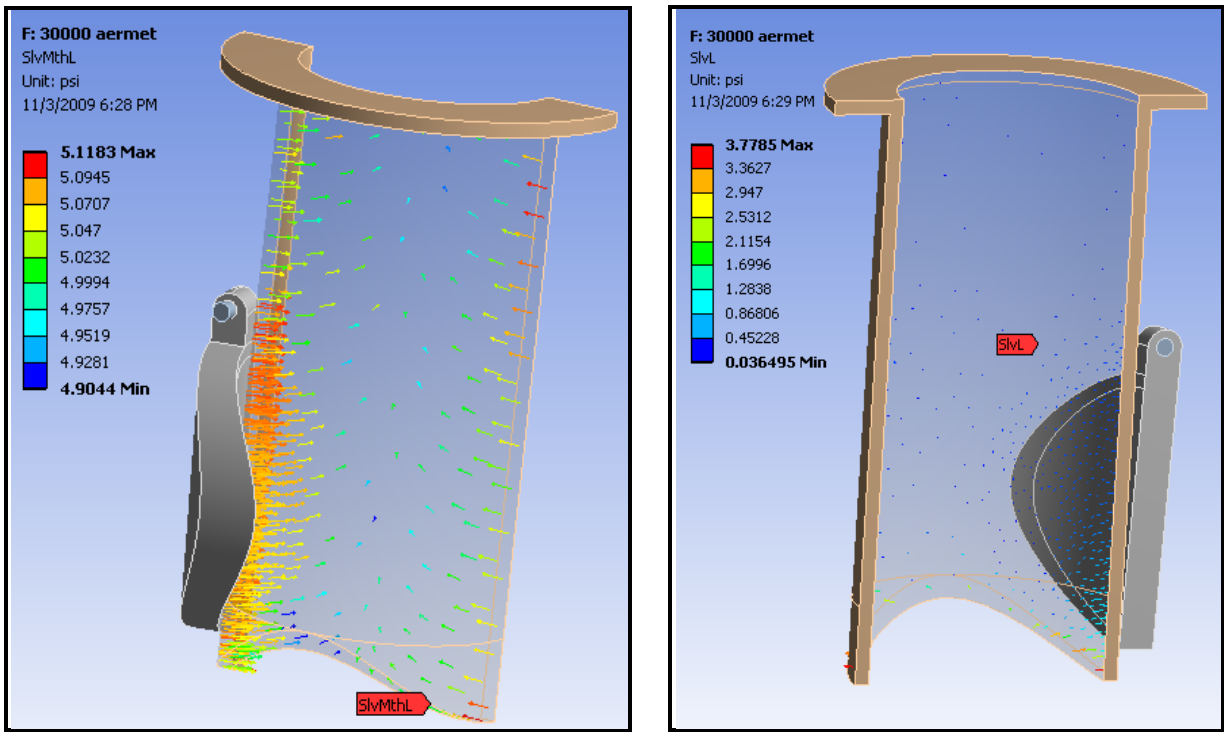


**(a) Slvmthl** **(b) slvl**

**Figure 5.8 CFX pressure mapping on the sleeve tube (fully open)**

For the fully closed case, the maximum loading happens at the closure point of the flapper. The flapper needs to seal against the hydrostatic pressure of the crude oil from both sides, the pressure surge caused by the water hammer and the impact caused by the motion of the flapper. For the hydrostatic pressure, assumptions have been made on three installation depths of the subsurface safety valve; at *2,000 ft*, *5,000 ft,* and *8,000 ft*. A *3,000 psi* water hammer pressure surge is added to the reservoir side of the flapper valve. Considering the results from Chapter 5, *3,000 psi* should serve as a good estimation of pressure surge. Another rotation velocity of *3.14 rad/s* is also applied to the flapper assuming the flapper rotates *90 degree* to shut off the well in *0.1 s* with a constant angular acceleration. The pressure loadings combining hydrostatic and water hammer pressures are shown in Table 5.4,

**Table 5.4 Pressure Loading for Fully Closed Case**

| Pressure loadings for fully closed case | | | | |
|---|---|---|---|---|
| **flap_ups (Upstream side)*** | | | | **flap_dns (Downstream side)** |
| **Depth of SSSV (ft)** | **Reservoir Depth (ft)** | | | |
| | ***10,000*** | ***20,000*** | ***30,000*** | |
| ***2,000*** | *30,251* | *26,816* | *23,380* | *687* |
| ***5,000*** | *31,282* | *27,846* | *24,411* | *1,717* |
| ***8,000*** | *32,312* | *28,877* | *25,442* | *2,748* |
| ***Water Hammer Pressure = 3,000 psi, Reservoir pressure = 30,000 psi** | | | | |

### 5.2.2 Pressure Loading Results and Discussion

After the finite element analysis, stress, strain, and displacement contours are obtained for both opening process and fully closed case.

**(1) Results for Reopening Process**

For the opening process, the sleeve tube needs to push the flapper open. The loading on the flapper is very high due to the high pressure of the fluid. The contact force between the flapper and the upper sleeve tube exceeds the yield stress already. Localized plastic deformations around the contact area are observed for the flapper and hinge-pin. A set of stress and strain contour plots over the opening process of the flapper is shown in Figure 6.9. The left figures are stress contour plots and the right ones are the strain plots. The red color shows the area where the stress is greater than the yield point (*160,000 psi*) of the material used and strain is over *0.05*. From Figure 5.9 (a) to (i), the transform of the high stress and strain area from the flapper to the hinge-pin at the initial stage of the opening process is observed to be caused by the movement of the contact point between sleeve tube and flapper. After a certain opening angle (i.e., *15 degree*), high stress and strain areas are only observed where stress concentration is expected, specifically, at the contact point between the sleeve tube and the flapper.

Under the assumption for the extreme high pressure and high temperature conditions, all three materials failed for a stress level over their yield stresses, which mean plastic deformation occured. Therefore, we need to revise the geometry of the flapper and conduct elasto-plastic analysis to lower the stresses and strains on the flapper.

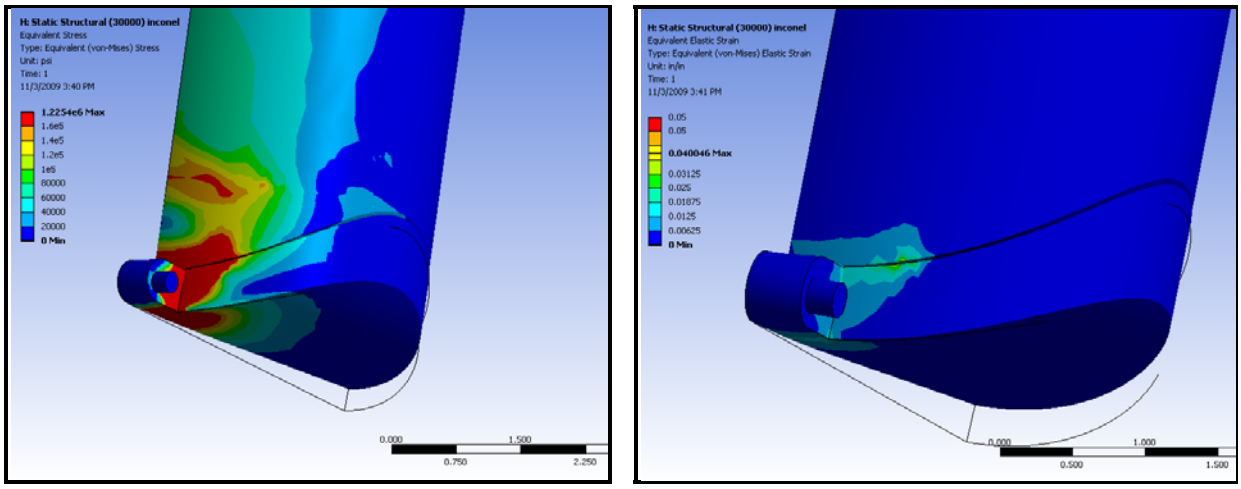


**(a) 5 degree open**

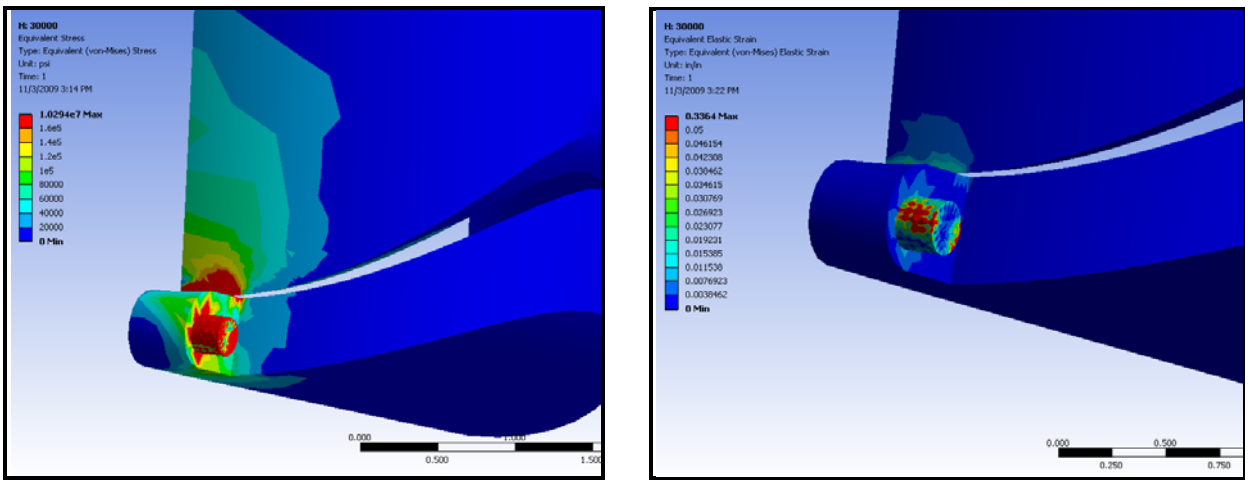


**(b) 15 degree open**

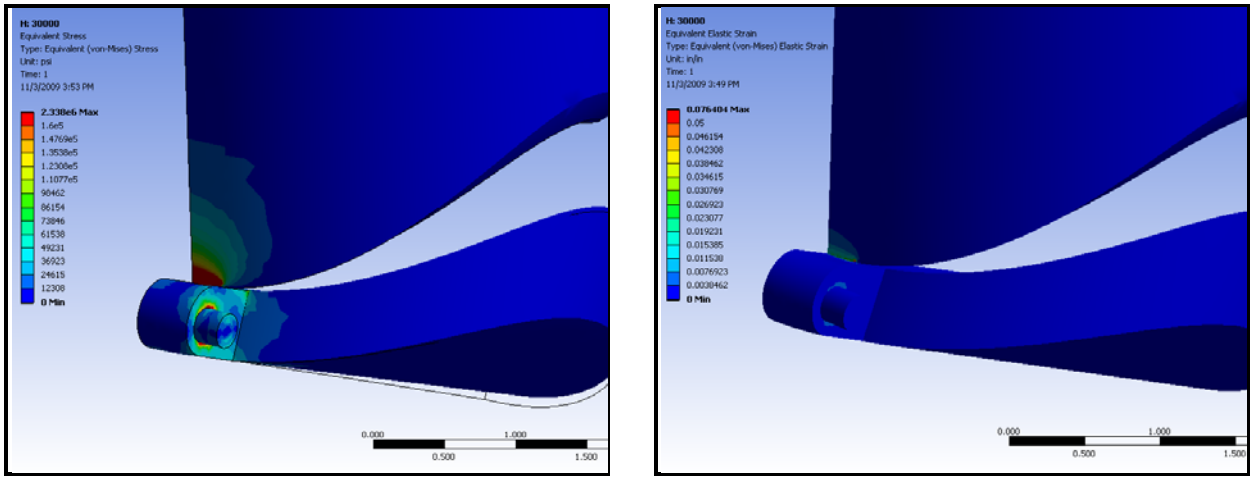


**(c) 25 degree open**

**Figure 5.9 Stress and strain plot for different opening angles (Inconel® 718)**

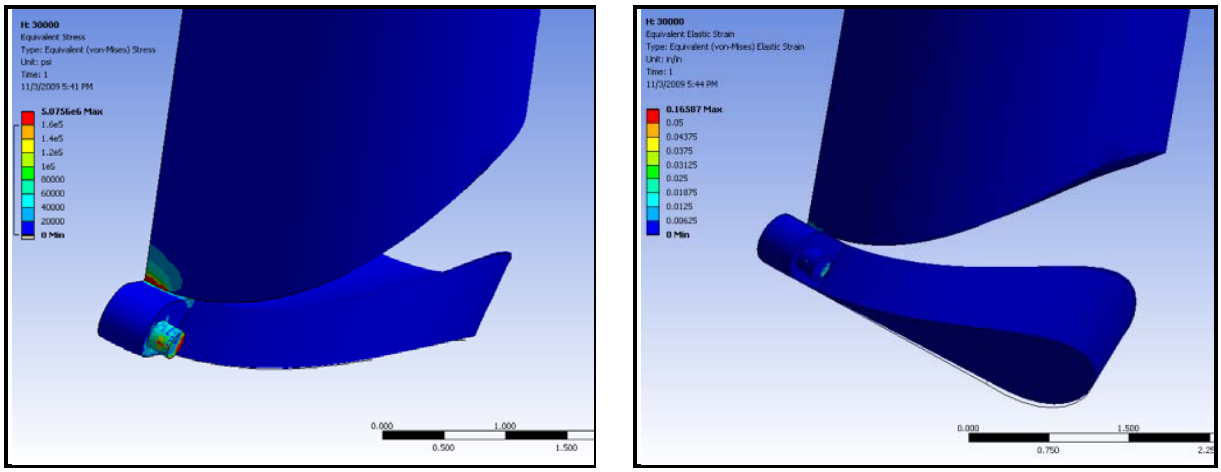


**(d) 35 degree open**

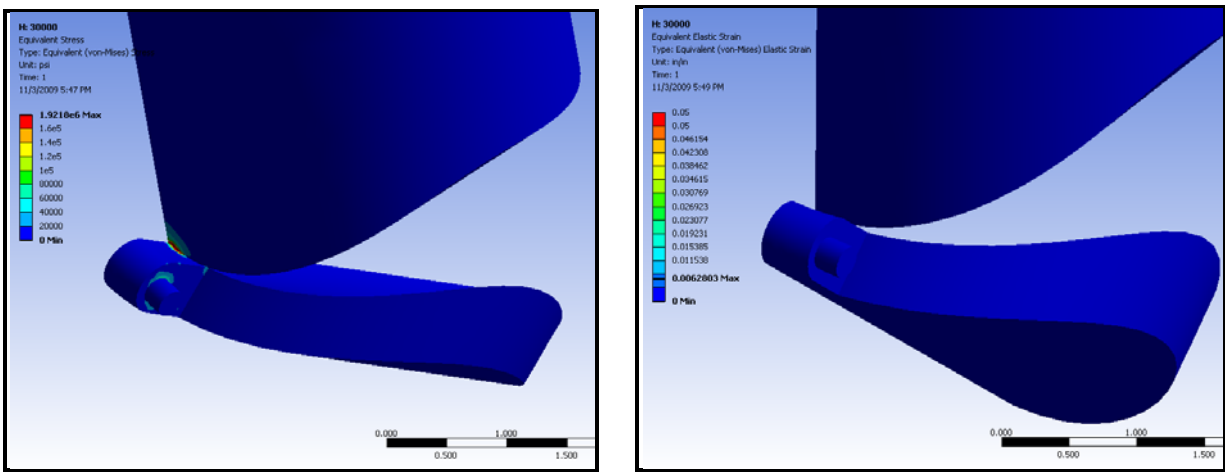


**(e) 45 degree open**

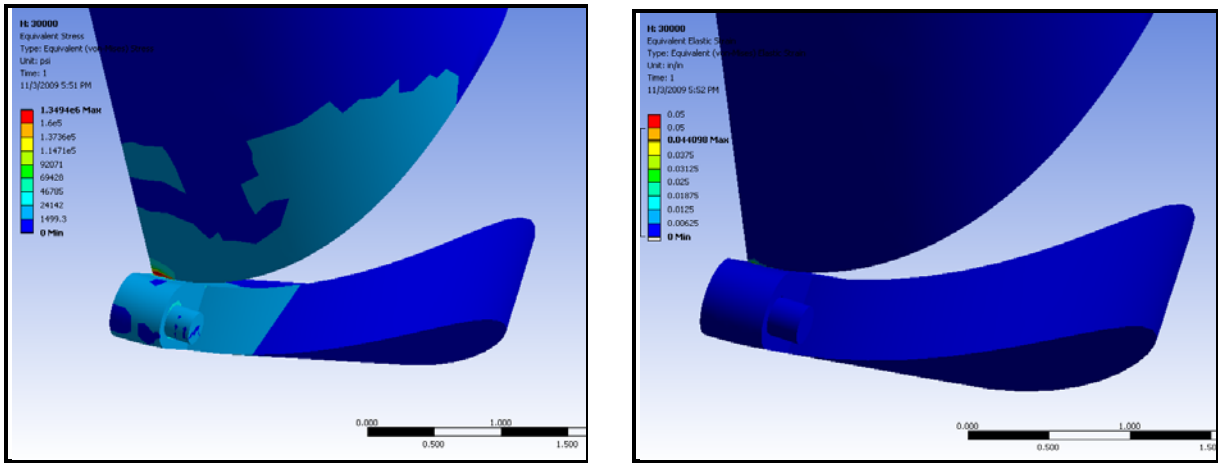


**(f) 55 degree open**

**Figure 5.9 Stress and strain plot for different opening angles (Inconel® 718) (continued)**

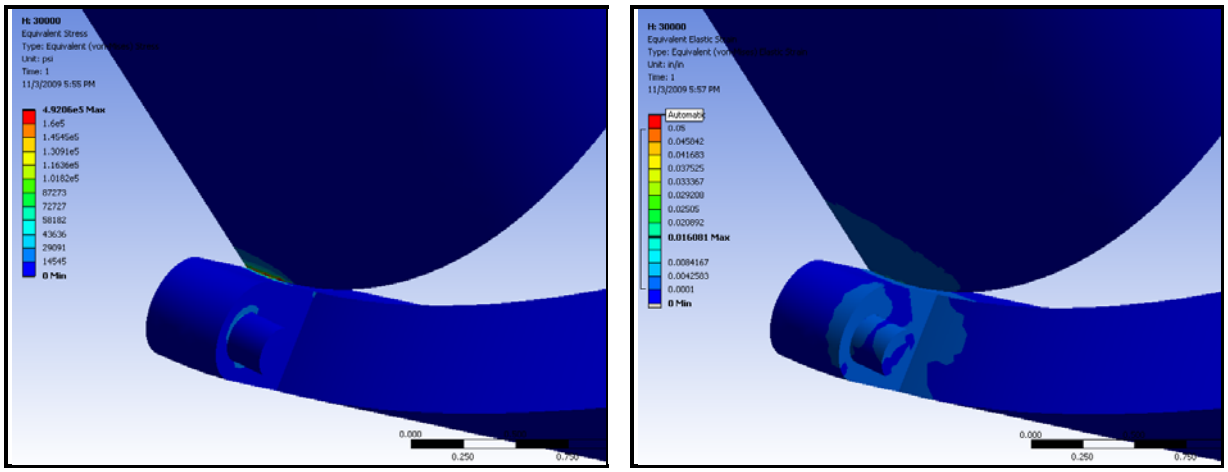


**(g) 65 degree open**

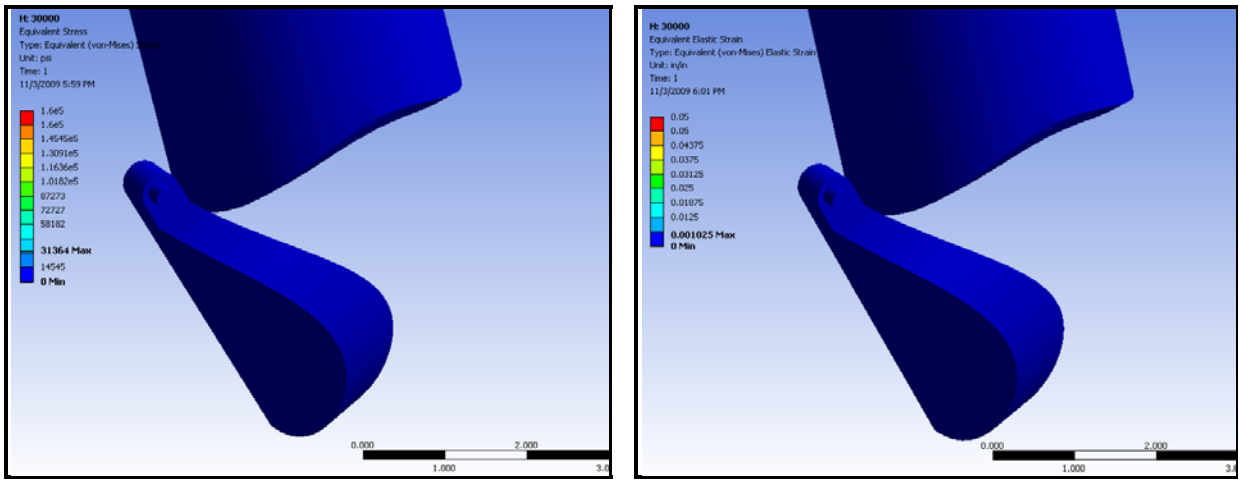


**(h) 75 degree open**

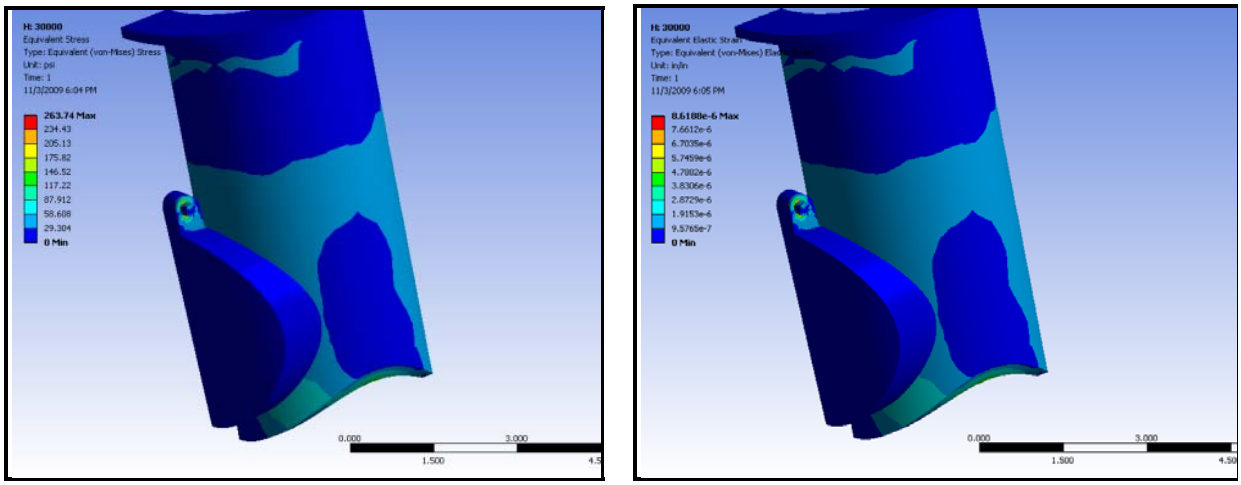


**(i) 87 degree open (Fully Open)**

**Figure 5.9 Stress and strain plot for different opening angles (Inconel® 718) (continued)**

## (2)Results for Fully-Closed Situation

The flapper valve has shown a good sealing ability at the fully-closed position. Figure 5.10 shows the displacement contour of the flapper under the assumed loadings (impact, water hammer, hydrostatic).

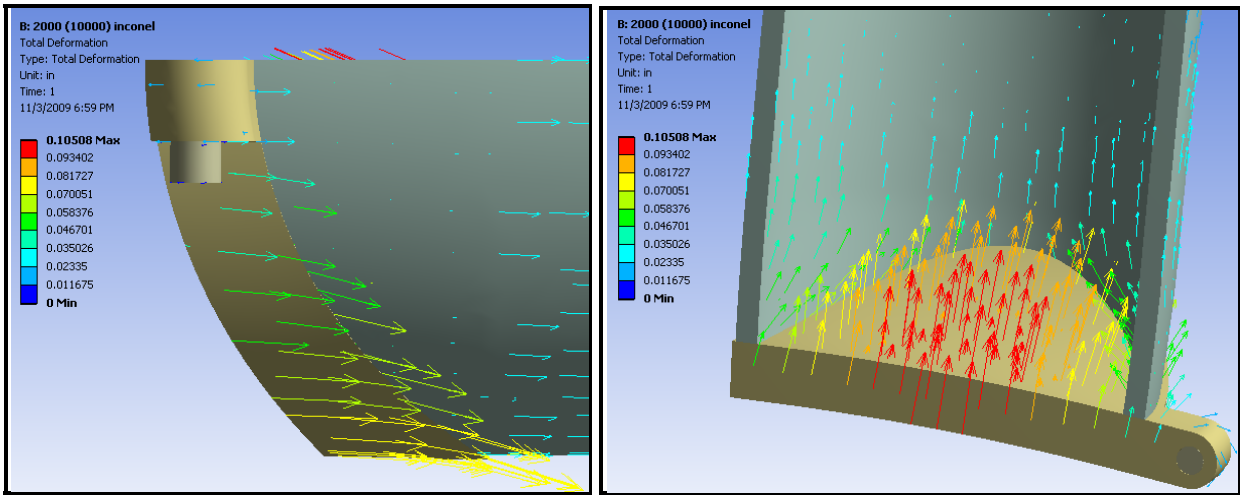


**Figure 5.10 Displacement contour of flapper at fully-closed position**

Figure 5.11 shows the stress contour of flapper valve at *5,000 ft* deep and reservoirs at *10,000 ft*, *20,000 ft,* and *30,000 ft,* deep respectively. Stress levels over the yield point are discovered on both the sleeve tube and flapper. Basically, the deeper the reservoir, the less stress discovered on flapper. Therefore, the subsurface safety valve should be placed as far above the reservoir as possible but below the mud line.

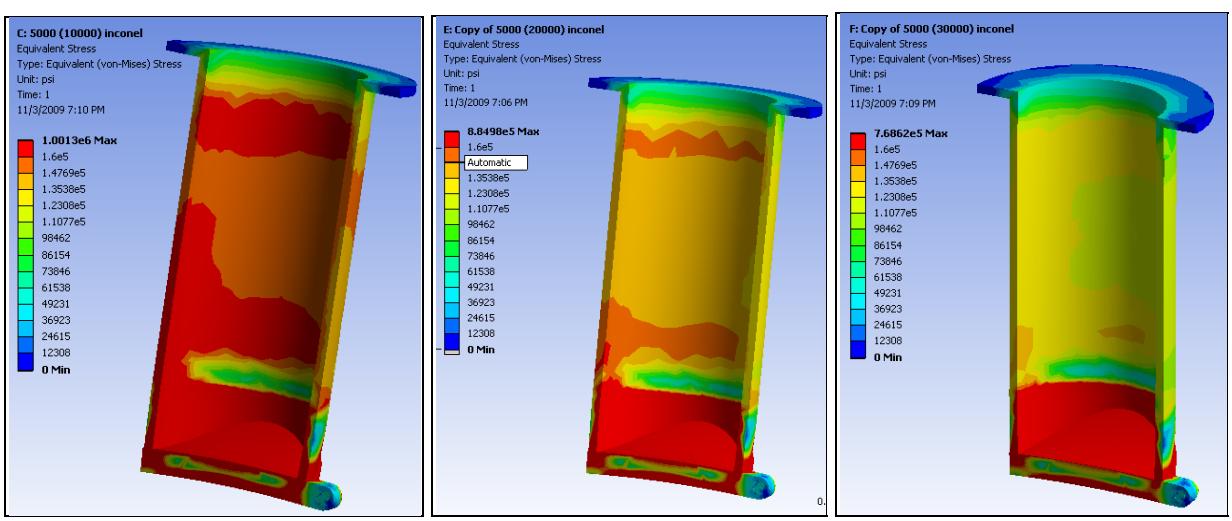


**(a) 10,000 ft** **(b) 20,000 ft** **(c) 30,000 ft**

**Figure 5.11 Flapper valve at 5,000 ft for various reservoir depth**

### (3) Contact Analysis Discussion

For the linear elastic contact analysis, the following conclusions are obtained.

- Highly localized plastic deformation is observed on the flapper. Further elasto-plastic FEM analysis of the stress and strain is needed.

- During the reopening process of the flapper, the most difficult moment happens at the beginning of the process. This conclusion is obtained without a pressure self-equalizing mechanism on the flapper.

- The SSSV should be placed at as far above the reservoir as possible but below the mud line.

- The maximum stress and strain occur when the flapper valve slam shuts off the pipeline, considering a combined fluid static pressure, water hammer pressure surge, and the impact between the flapper and the sleeve tube.

## 5.3 Parametric Study in SolidWorks 2009

From the previous linear elastic contact analysis, it is shown that the flapper valve experiences highly localized plastic deformation during its rotational movement. Therefore, a elasto-plastic parametric study should be carried out to lower the stress and strain level to an acceptable level. For this parametric study, we assume that the reservoir at *30,000 ft* with *30,000 psi* and the SSSV is placed *2,000 ft* below the sea level. We will consider, a situation when the flapper slam shuts the pipeline, since it is the worst scenario.

### 5.3.1 Estimation of Impact Angular Acceleration and Velocity

The typical closing procedure for a subsurface safety valve is achieved by removing the hydraulic pressure applied on the sleeve from the surface, i.e., production platform. Then the sleeve is retrieved either by the reaction force from the compressed spring or the magnetic force offered by the magnetic coupling. Hence, the flapper is driven by the fluid pressures to rotate almost 90 degrees to shut off the production pipe. During this whole slam-shut process, the contact between the sleeve tube and flapper is not as serious as the last impact contact. Therefore, we will only look at the last impact moment for the parametric study.

To obtain the final acceleration and the angular velocity at impact, it is assumed that the closure motion of the flapper could be assumed as a planar rigid body rotation around a fixed axis with fluid pressure loading on both surfaces of the flapper, which is sketched as follows,

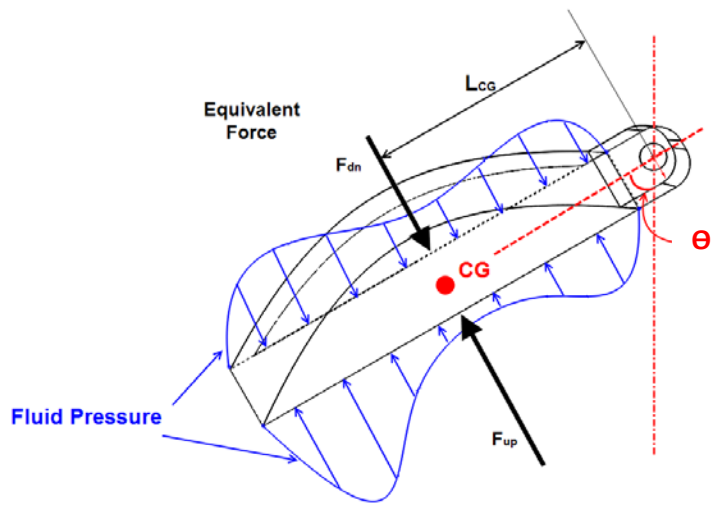


**Figure 5.12 Free body diagram sketch of a flapper SSSV**

The fluid pressures on both sides of the flapper are obtained from the quasi-static computational fluid dynamics results in Chapter 3, a further post processing to integrate the fluid pressure over the flapper surfaces are also conducted to obtain the loading forces. The angular motion equation of the flapper, about a fixed axis, is as follows,

$$M = J\ddot{\theta} \tag{5.1}$$

Where the resultant moment from the pressures is, $M = (F_{up} - F_{dn})L_{CG}$, $J$ is the inertia of momentum around the fixed axis. The center of the force, $F$, is assumed to be the center of gravity of the flapper. Therefore, the resulting angular accelerations from the CFD analysis are interpolated. The evaluated acceleration upon closure is extrapolated by the polynomial obtained. The extrapolated acceleration result varies with respect to the polynomial degrees. The 8$^{th}$ degree polynomials were used to piecewise interpolate the nine data points in this study. That will give us a relatively accurate acceleration estimate, and that estimated acceleration should be larger than the actual one for the sake of looking at some worst-case scenarios. The extrapolated results are shown in Figure 5.13.

Figure 5.13 shows that the flapper is fully open when $\theta = 5^{\circ}$and fully closed when $\theta = 90^{\circ}$. The circles are calculated from the results at eight equally spaced instances (between $5^{\circ}$ and $90^{\circ}$) from the CFD results. The flapper is accelerated consistently during its closing motion, and the acceleration increased dramatically at the end, which reflects the dramatic pressure change from an opening pipe to a closed pipe. The maximum angular acceleration is obtained from the fitted curve. The area below the fitting curve is proportional to the square of the final angular velocity from Eq. (5.2):

$$\boldsymbol{A = \int \alpha d\theta = \frac{1}{2}\omega_{final}^{2}} \tag{5.2}$$

Therefore, the final acceleration and angular velocity is obtained as

$$\boldsymbol{\alpha_{final} = 30,198\ rad/s^2} \qquad (5.3)$$
$$\boldsymbol{\omega_{final} = 75.5\ rad/s.}$$

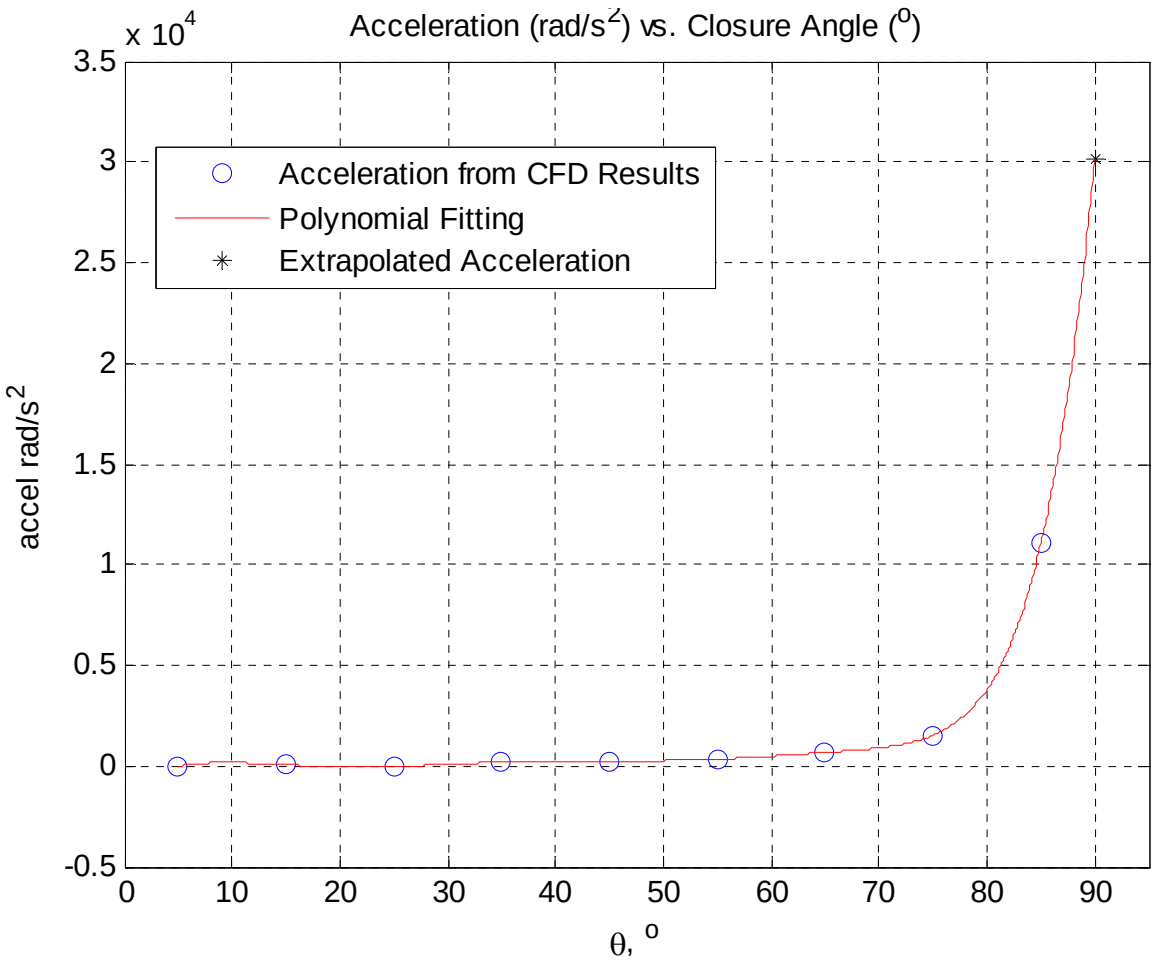


**Figure 5.13 Acceleration extrapolation from quasi-static FSI analysis**

## 5.3.2 FEM Preprocessing for Impact Analysis

### (1) Geometry and Mesh

Considering the symmetry of the flapper valve as shown in Figure 5.14, only half of the flapper geometry is used for the elasto-plastic analysis. The mesh results are also shown in Figure 5.14.

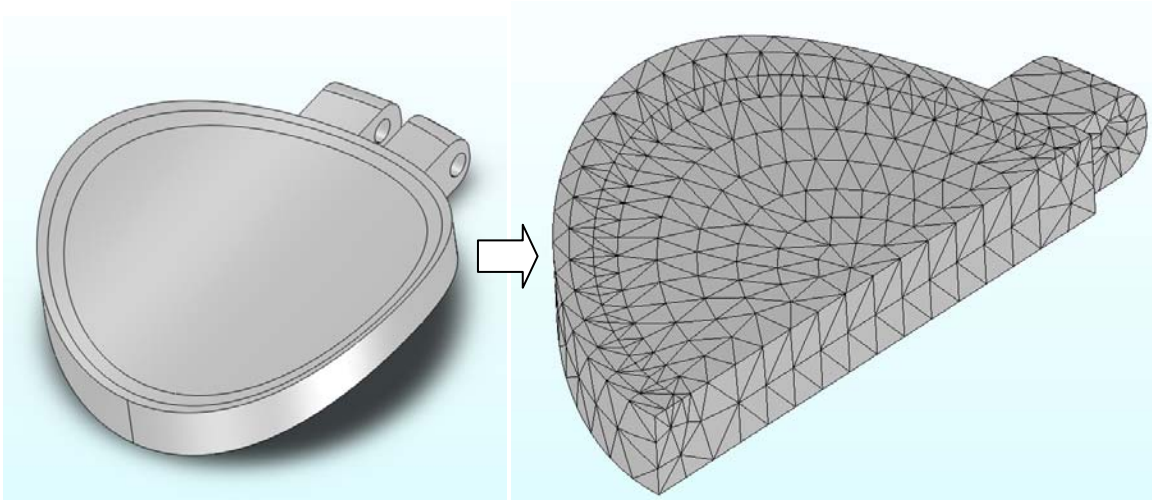

**Figure 5.14 A full flapper geometry and its half size mesh results**

The total element number shown in Figure 5.14 is *2,842*, with *4,808* nodes. The element used is a 10-node tetrahedral element.

## (2) Boundary Conditions

The boundary conditions and displacement restraints applied to the flapper are as follows and as shown in Figure 5.15, the corresponding boundaries are as follows:

**I.** Symmetric boundary
**II.** No vertical displacement for the contact area
**III.** No radial and axial displacement for the hinge-pin surface.

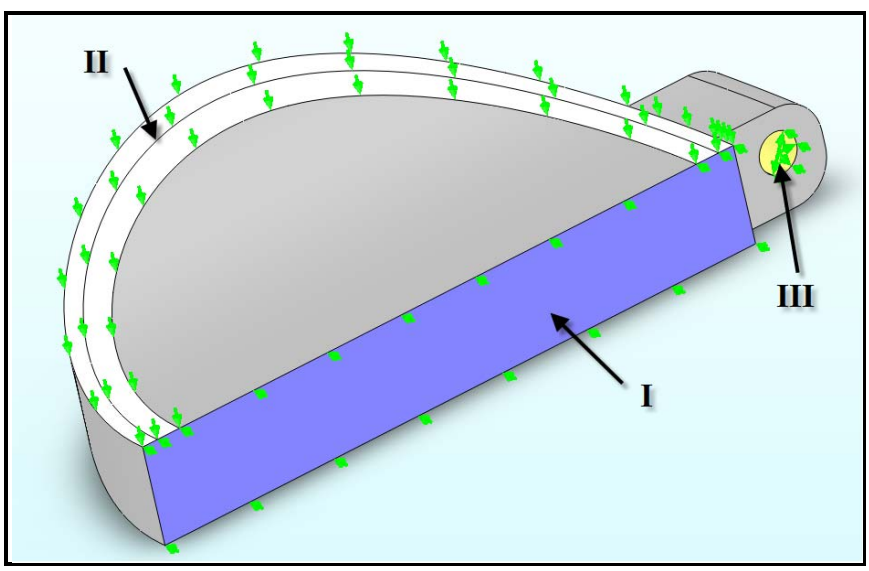


**Figure 5.15 boundary locations of a half flapper model**

## (3) Material Properties

The solid material used for the elasto-plastic FEM analysis is *Inconel* 718. The results of the elasto-plastic analysis will be further used to define the cyclic strain history for low cycle fatigue analysis. Therefore, according to *BPVC Sect VIII, Vol.2*, a twice-yielded method should be implemented such that the material behavior is defined by a cyclic stress-strain curve. The parameters of the Ramberg-Osgood model defining the cyclic stress-strain curve for *Inconel* 718 are obtained (from Dowling 1998) and are listed in Table 5.5. The stress strain curve is defined using Ramberg-Osgood model as in (5.4) with parameters in Table 1.

$$\boldsymbol{\varepsilon} = \frac{\boldsymbol{\sigma}}{\boldsymbol{E}} + \left(\frac{\boldsymbol{\sigma}}{\boldsymbol{H}}\right)^{\frac{1}{n}} \tag{5.4}$$

**Table 5.5 Material Fatigue Properties for Inconel X**

| **Inconel 718** | | | | | | |
|---|---|---|---|---|---|---|
| Cyclic stress – strain curve | | | Strain-life curve | | | |
| $E(ksi)$ | $H(ksi)$ | $n$ | $\sigma'_f(ksi)$ | $b$ | $\varepsilon'_f$ | $c$ |
| 31,000 | 269 | 0.120 | 327 | -0.117 | 1.16 | -0.749 |

The cyclic stress-strain curve is obtained from (5.4) and is plotted in Figure 5.16 as follows,

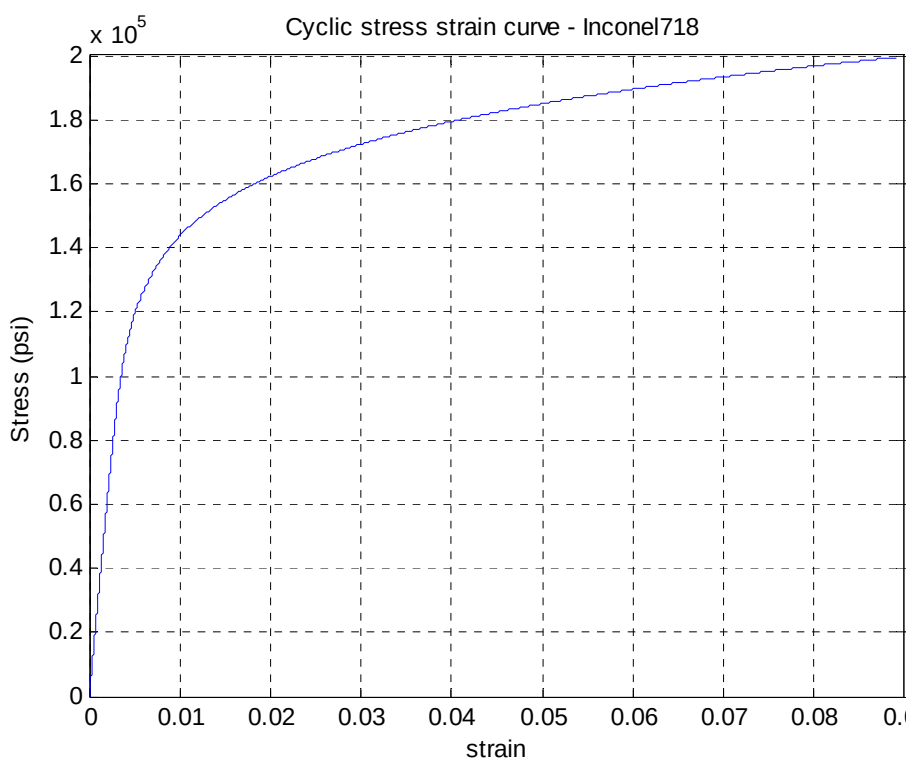


**Figure 5.16 Cyclic stress-strin curve of Inconel 718**

## (4) Slam Loadings

When the flapper slam-shuts the pipeline, two loadings are considered. The first one is the angular acceleration and angular velocity, in *SolidWorks*, they are added as a centrifugal force. The second part is the pressure loading, which combines the static pressure from the reservoir side and the water hammer pressure surge.

### I. Centrifugal and Tangential Forces

In *SolidWorks* (Akin 2010), the angular acceleration and angular velocity can be added as a centrifugal force as shown in the Figure 5.17,

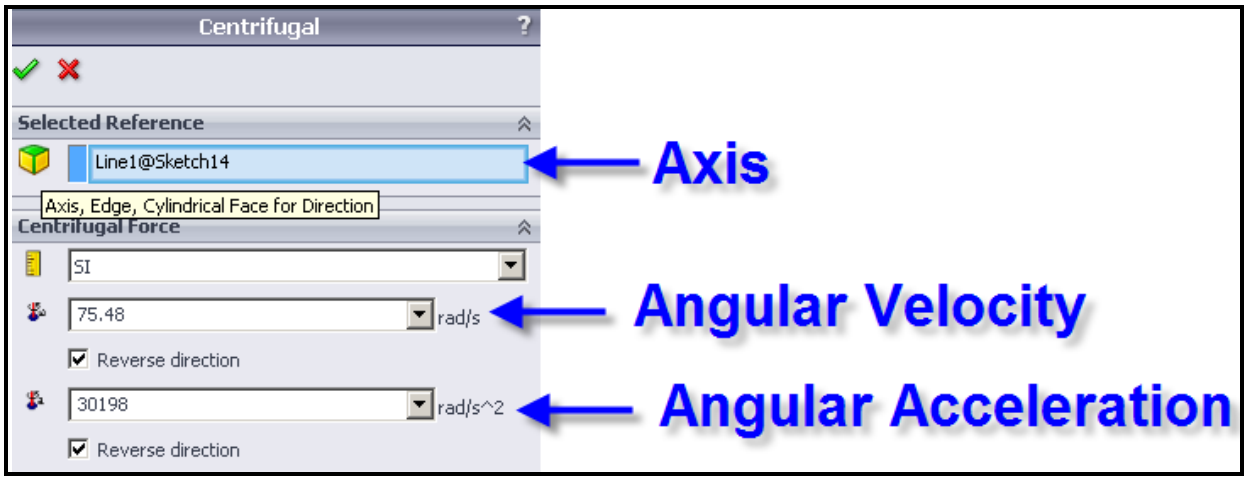


**Figure 5.17 Centrifugal force settings in Solidworks 2009**

### II. Static Pressure and Water Hammer Pressure

The pressure loadings are applied to the upstream side of the flapper. For the reservoir assumptions, the static pressure is *20,380 psi* from table 3.6 and the water hammer pressure is estimated to add another *3,000 psi*. Therefore, a combined pressure (named Ups_flap) of *23,380 psi* is applied to the upstream side of the flapper, as shown in Figure 5.18.

## 5.3.3 Definition of Key Parametric Dimensions

The parametric study of the flapper to lower the stress level focuses on four key geometric parameters, i.e., flapper thickness, flapper outer radius, flapper inner radius, and hinge pin diameter. The geometric parameters are shown and defined in Figure 5.19.

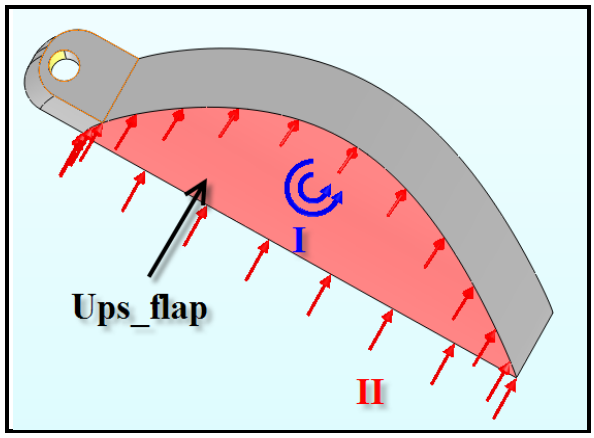


**Figure 5.18 Flapper upstream pressure location**

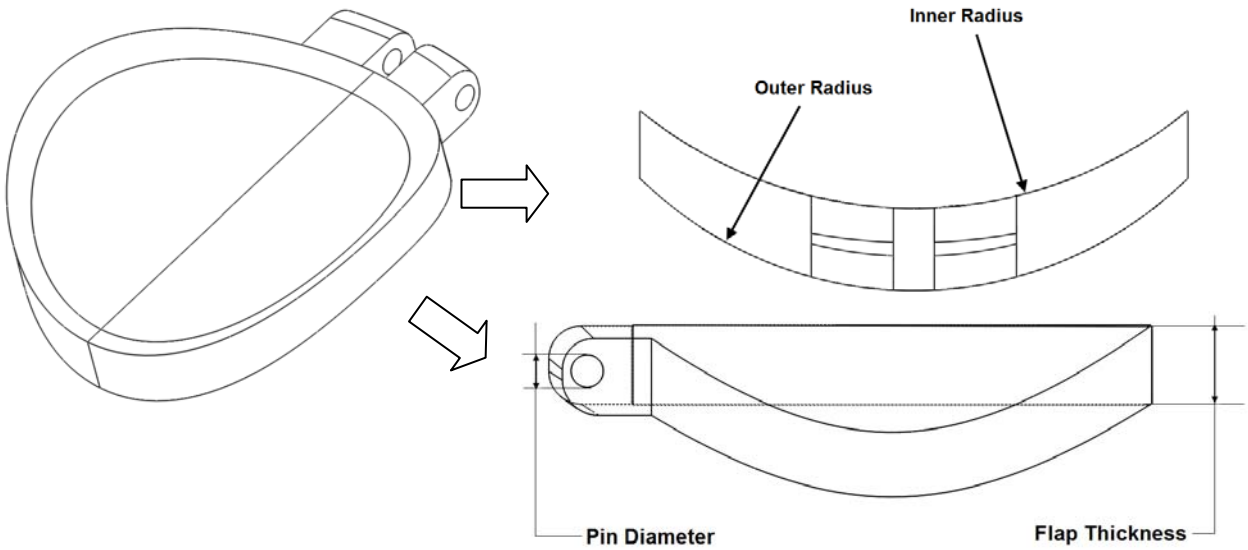


**Figure 5.19 Geometric parameters defined for the parametric study**

## 5.3.4 Parametric Study Results

The elasto-plastic FEM analysis has been conducted with respect to different geometrical parameters defined in the last section.

### (1) Flapper Thickness Variation

Figure 5.20 and Figure 5.21 show the maximum total von-Mises equivalent strain, maximum von-Mises equivalent plastic strain, maximum von-Mises equivalent stress, and stress intensity against different flapper thickness. It is shown that the stress and strain level can be reduced within the yield surface with an increase of the flapper thickness by about 42% (from *0.6 in* to *0.85 in*).

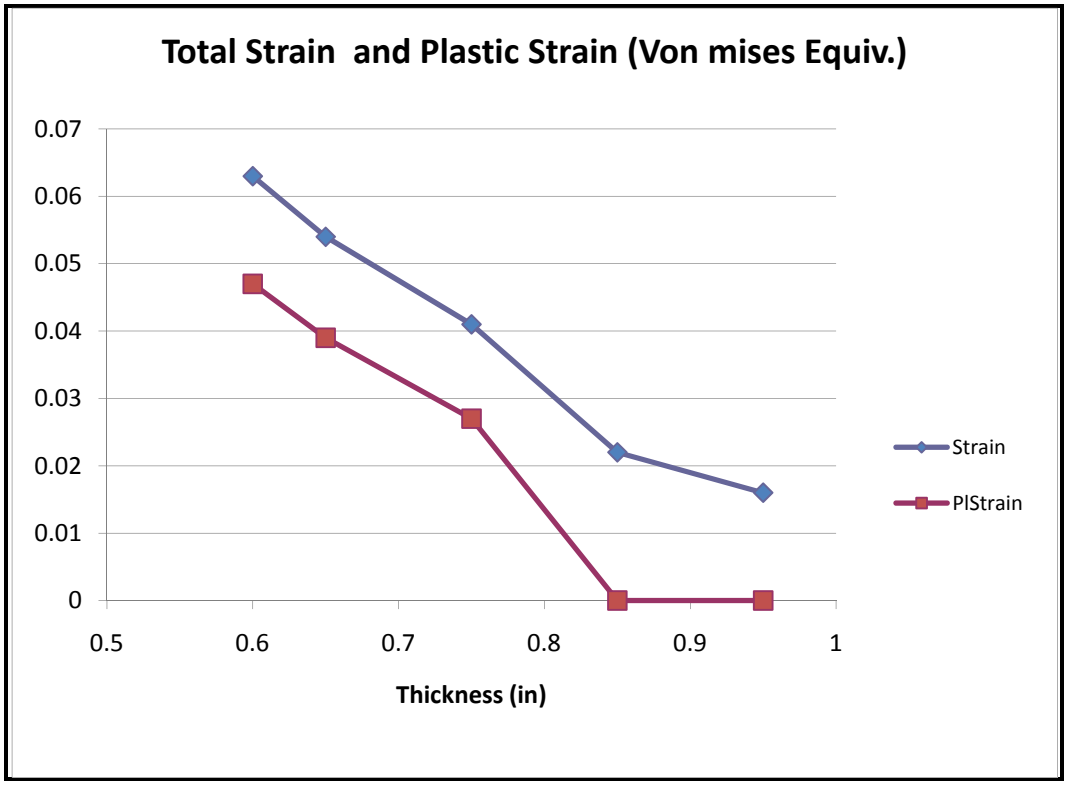


**Figure 5.20 Total equivalent strain, plastic strain vs. flapper thickness**

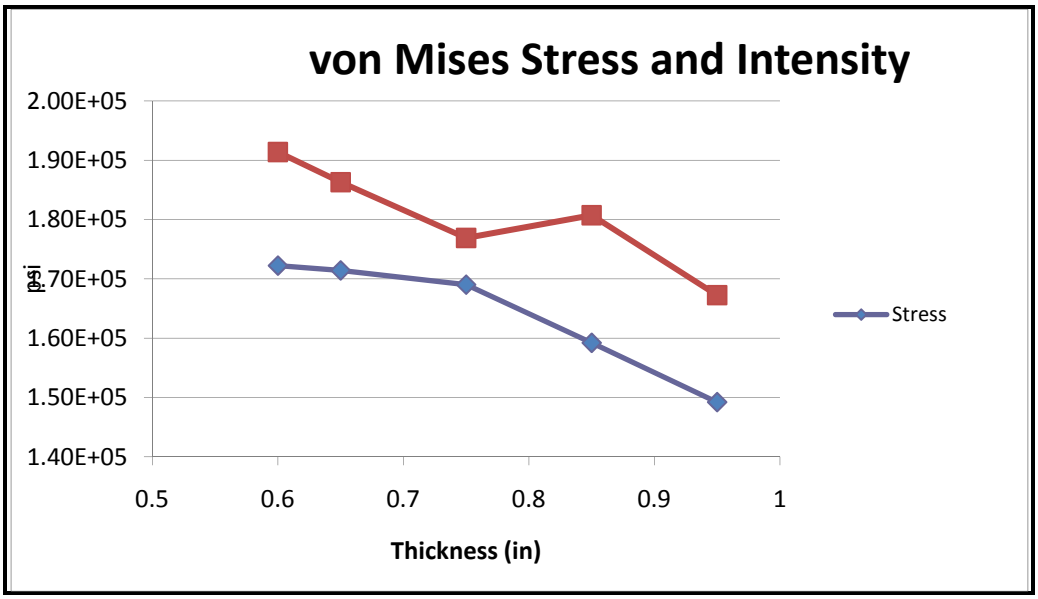


**Figure 5.21 Equivalent stress, stress intensity vs. flapper thickness**

### (2) Inner Radius and Outer Radius Results

Figure 5.22 through Figure 5.25 show the maximum total von-Mises equivalent strain, the maximum von-Mises equivalent plastic strains, the maximum von-Mises equivalent stress, and the stress intensity, respectively against various inner radius and outer radius of the flapper surface. The parametric study does not show an obvious reduction of the stress and strain level with respect to the change of the two parameters.

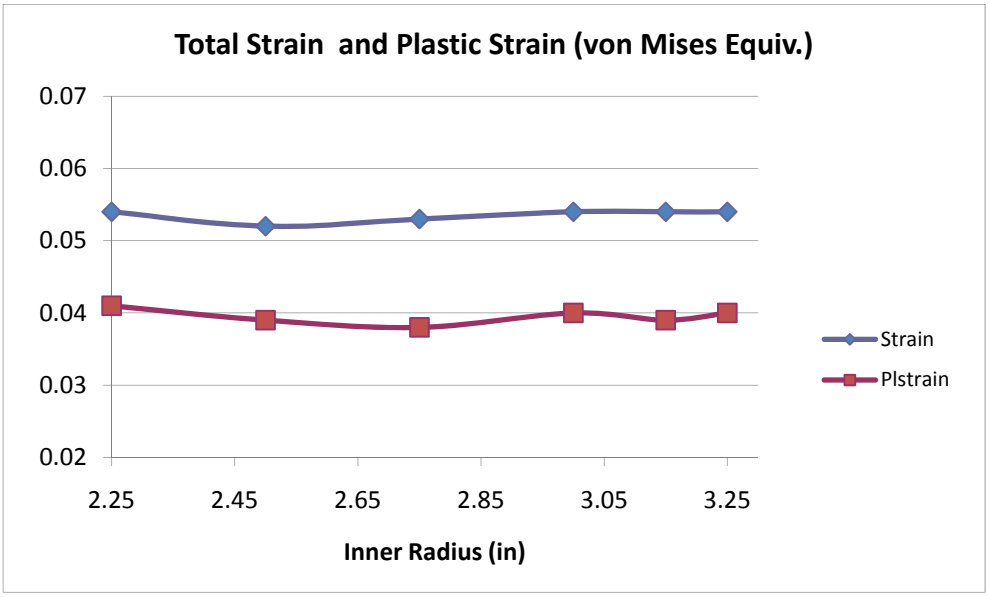


**Figure 5.22 Total equivalent strain, plastic strain vs. flapper inner radius**

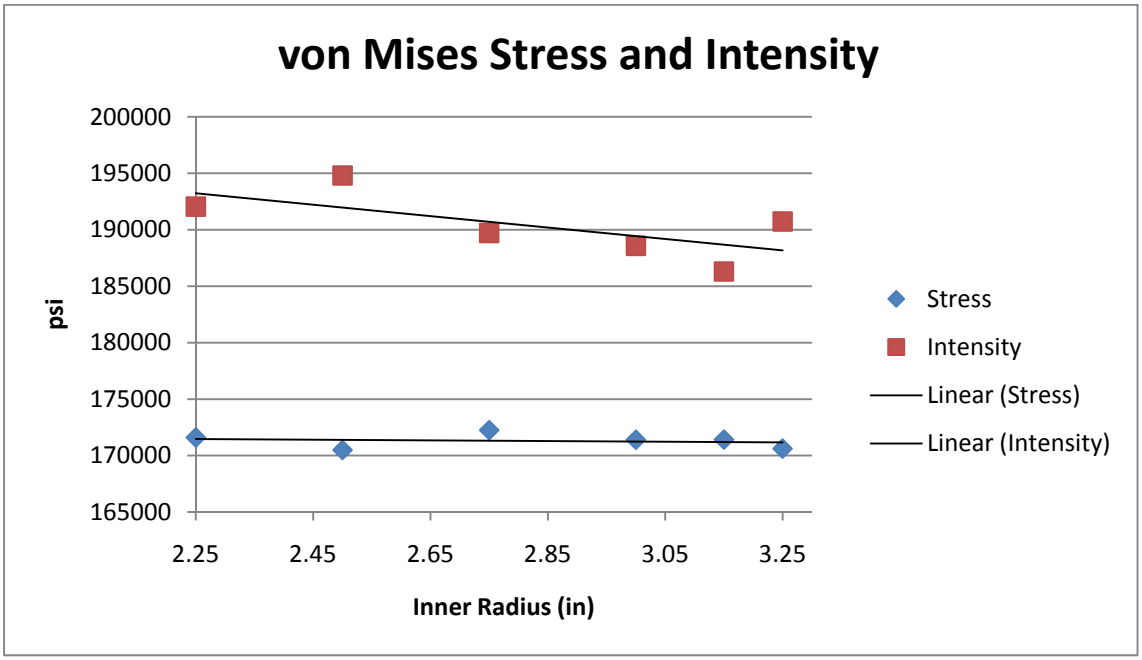


**Figure 5.23 Equivalent stress, stress intensity vs. flapper inner radius**

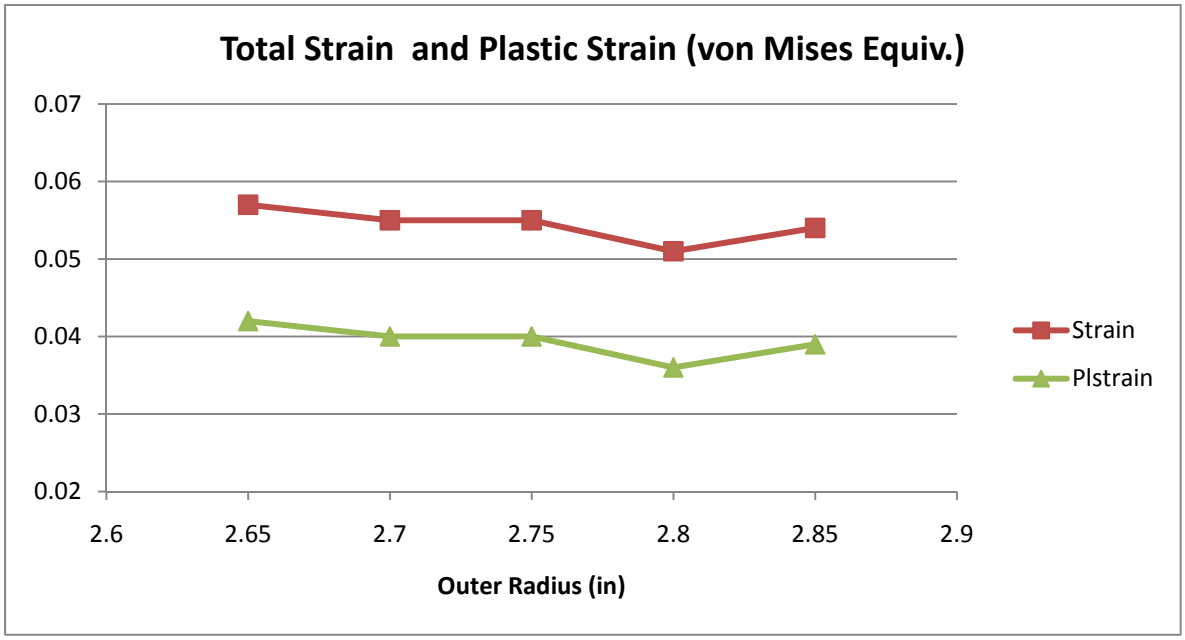


**Figure 5.24 Total equivalent strain, plastic strain vs. flapper outer radius**

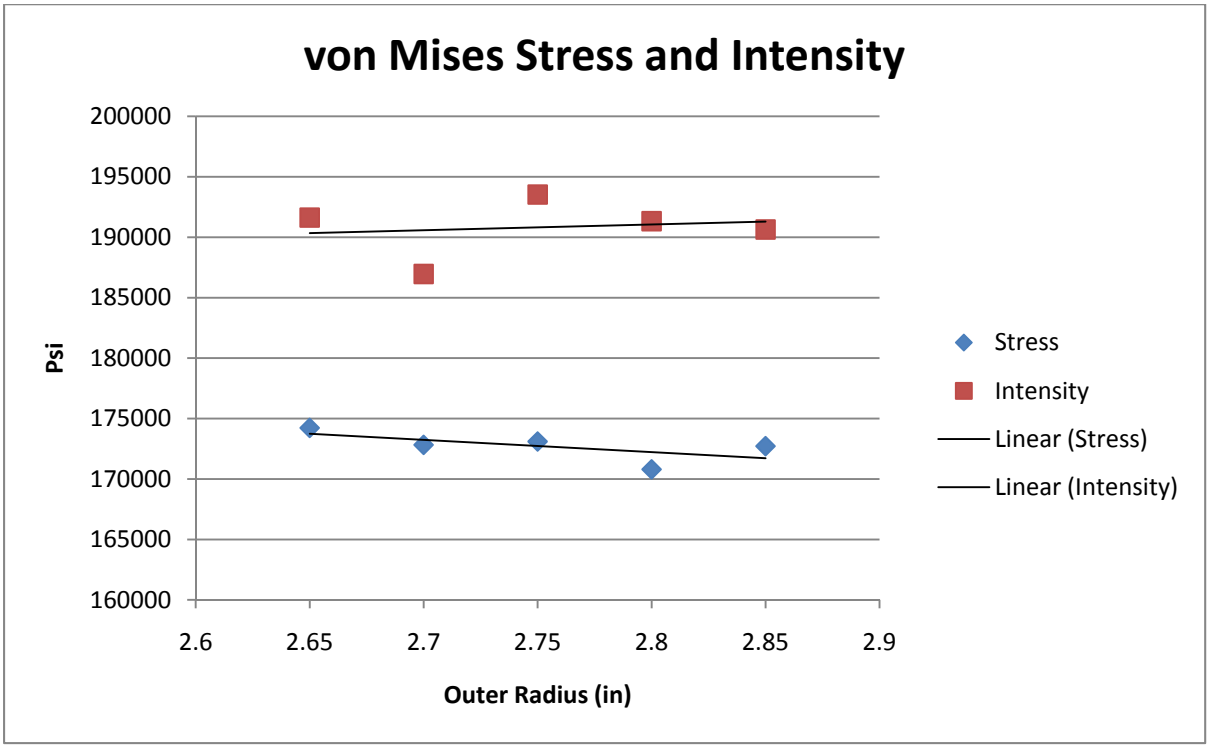


**Figure 5.25 Equivalent stress, stress intensity vs. flapper outer radius**

### (3) Pin Diameter Variations

The reaction force, *P*, on the hinge pin's bearing surfaces is obtained by *SolidWorks*. Figure 5.26 plots the resultant forces against various thicknesses. It is shown that the resultant forces decrease linearly with the increase of the flapper thickness.

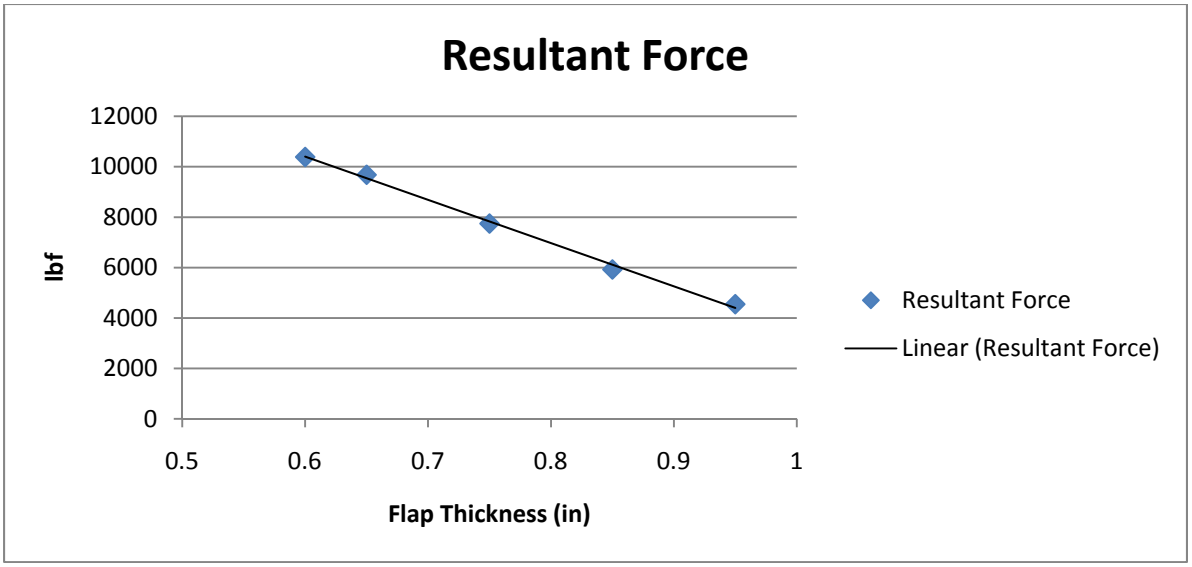


**Figure 5.26 Resultant force on the pin hole of the flapper vs. flapper thickness**

The flapper's hinge pin mainly suffers from a pure shear deformation. According to BPVC, maximum shear stress across a section loaded in pure shear should be limited to 0.4 times the initial yield stress. Then, assuming the cross section area of the hinge pin is circular with diameter *D*, the maximum shear stress is

$$\boldsymbol{\tau_{MAX}} = \frac{\mathbf{16}\boldsymbol{P}}{\mathbf{3}\boldsymbol{\pi D^2}} \tag{5. 5}$$

The material used is *Inconel* 718, whose yield stress is *16,000 psi*. Therefore, the maximum shear stress $\tau_{MAX}$ should be limited to *6,400 psi*. The minimum pin diameters against different flapper thicknesses are obtained and plotted in Figure 5.27,

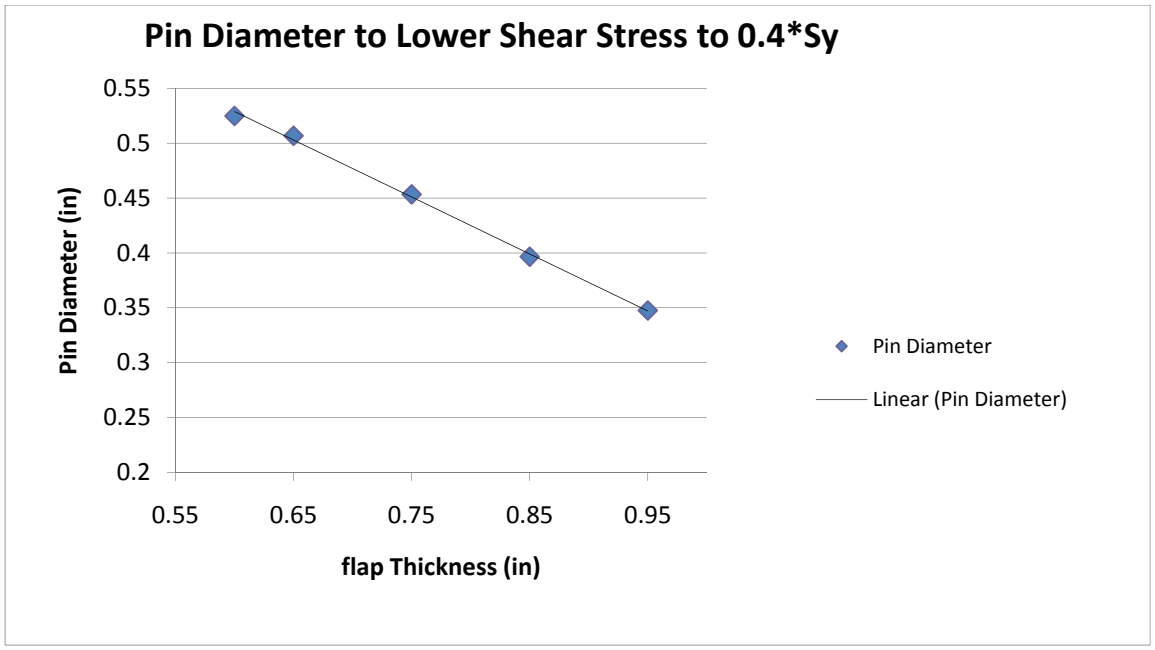


**Figure 5.27 Minimum pin diameter vs. flapper thickness**

## 5.4 Modified Flapper Results and Discussion

A modified flapper SSSV is obtained from the parametric study. The stress and strain levels are reduced to the acceptable range. The plastic deformation only occurs at the situation when the flapper just slam-shuts the pipeline. The modified CAD model of the flapper is shown in Appendix A. The stress contour plots are shown for different opening angles in Figure 5.28. It is shown that the maximum stress level occurs at the closure of the flapper as expected. The maximum equivalent stress is around *1.61E5 psi*. Highly concentrated stress also occurs at the contact region and the neighborhood of the hinge pin.

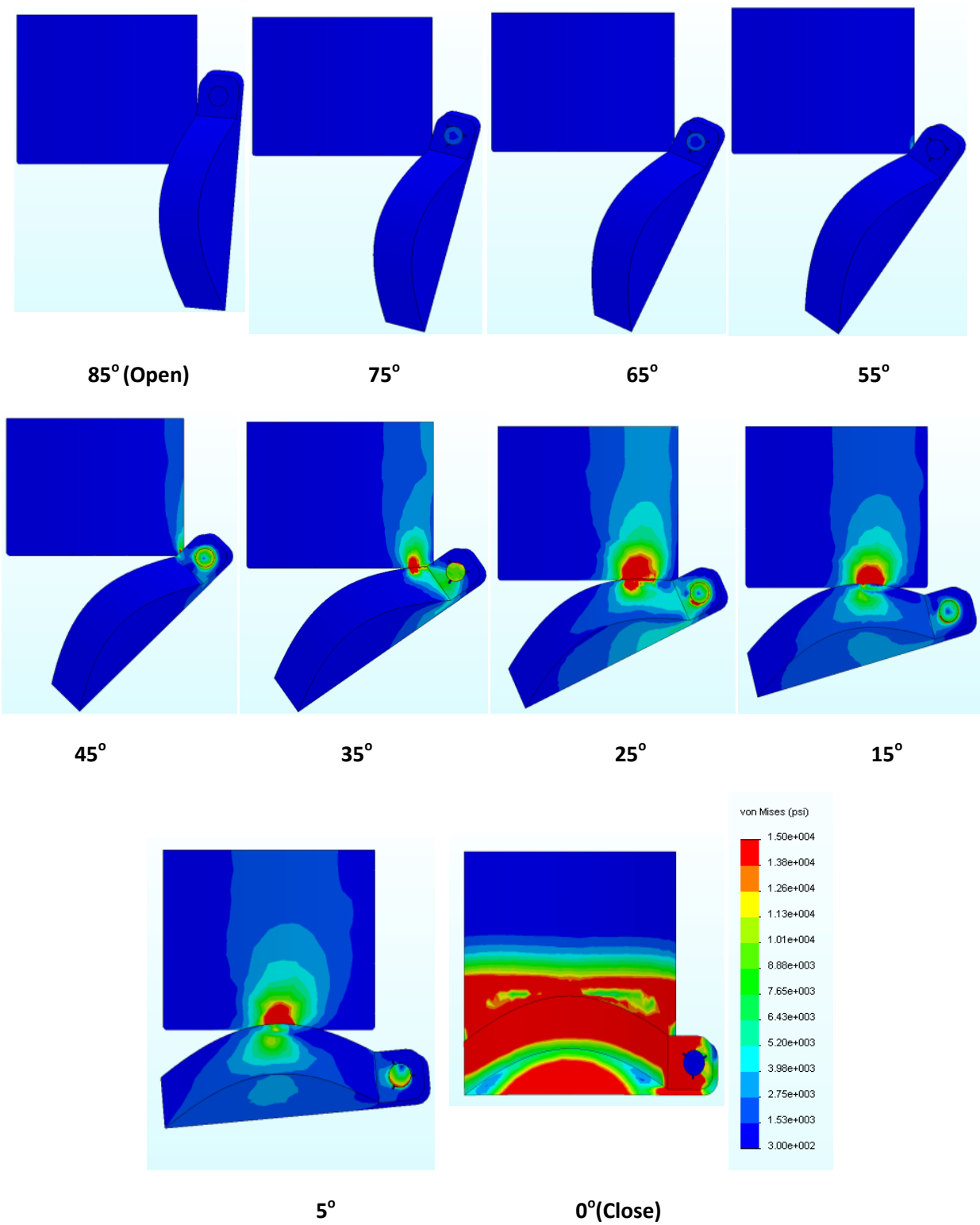


**Figure 5.28 Stress contour plots for a parametric optimized flapper**

# Chapter 6

# Low Cycle Fatigue

*In this Chapter, a low cycle fatigue analysis is conducted on the flapper SSSV obtained from the parametric study from the last Chapter. Two LCF models have been used and their results are compared.*

## 6.1 Problem Definition

From the previous finite element analysis results, it is evident that the subsurface safety valve experiences a high level of stress and localized plastic deformation due to the fluid pressure loadings during its opening and closing process. Through a parametric study, the shape of the flapper has been optimized and the stress level has been reduced close or within the yield surface. The step is to analysis the SSSV performance under cyclic loadings.

As introduced before, during the twenty-year life expectation of the subsurface safety valveSSSV's closing and reopening operations will be executed for at least biannual checks plus other emergency shut-off operations. Therefore, the subsurface safety valve should stand high pressure impact loadings cyclically for around *100 - 200* times. A highly possible failure mode caused by the cyclic loading, or the low cycle fatigue (LCF) of the material should be taken care of for its design.

Typically, fatigue can be classified into high cycle (> 100,000 cycles) and low cycle fatigue (*10-100,000* cycles). The fatigue issue of the subsurface safety valves is a low cycle fatigue problem. Research has shown that the main factor causing a lower cycle fatigue failure is the plastic strain rather than the elastic strain. Plastic strain becomes the predominant reason for the failure of the SSSV design. However, the current API standards for the design of SSSV only covers high cycle fatigue. W-e think it is also necessary to include guidelines on LCF designs.

For time and software licensing considerations, the cyclic strain history is obtained from the previous quasi-static process to estimate the low cycle fatigue life of a flapper shaped SSSV. Our assumptions for the LCF analysis are kept the same- a 30,000 psi reservoir at 30,000 ft deep and the SSSV is placed at 2,000 ft below the sea level. The LCF is analyzed through both a continuum damage mechanics model and a strain life approach for comparison. This process could be extended to LCF design of the other components served at XHPHT environments.

## 6.2 Cyclic Strain History by FEA

The stress-life approaches adopted for high cycle fatigue analysis are not suitable for low cycle fatigue analysis, since they do not address the plastic deformations. Therefore, we need to use

strain-based approaches. The first step is to obtain the cyclic strain history for the flapper. A cycle refers to the flapper closing and the subsequent reopening.

## 2.1 Preprocessing and Mesh Facts

The LCF fatigue analysis is based on the stress and strain results from the elasto-plastic finite element analysis. The CFD fluid pressures are calculated from ANSYS CFX v12.0 and mapped onto the flapper surfaces as loadings for the static stress calculation. The maximum von Mises equivalent strain and plastic strain are recorded for each opening angle as defined in the quasi-static analysis in Figure 3.3. Figure 6.1 shows finite element mesh of the simplified half model of the SSSV obtained from parametric study. The elements used are 10-node tetrahedral elements. A no penetration contact is set between the flapper and the sleeve tube. A hinge pin connection is established between the flapper and the pin.

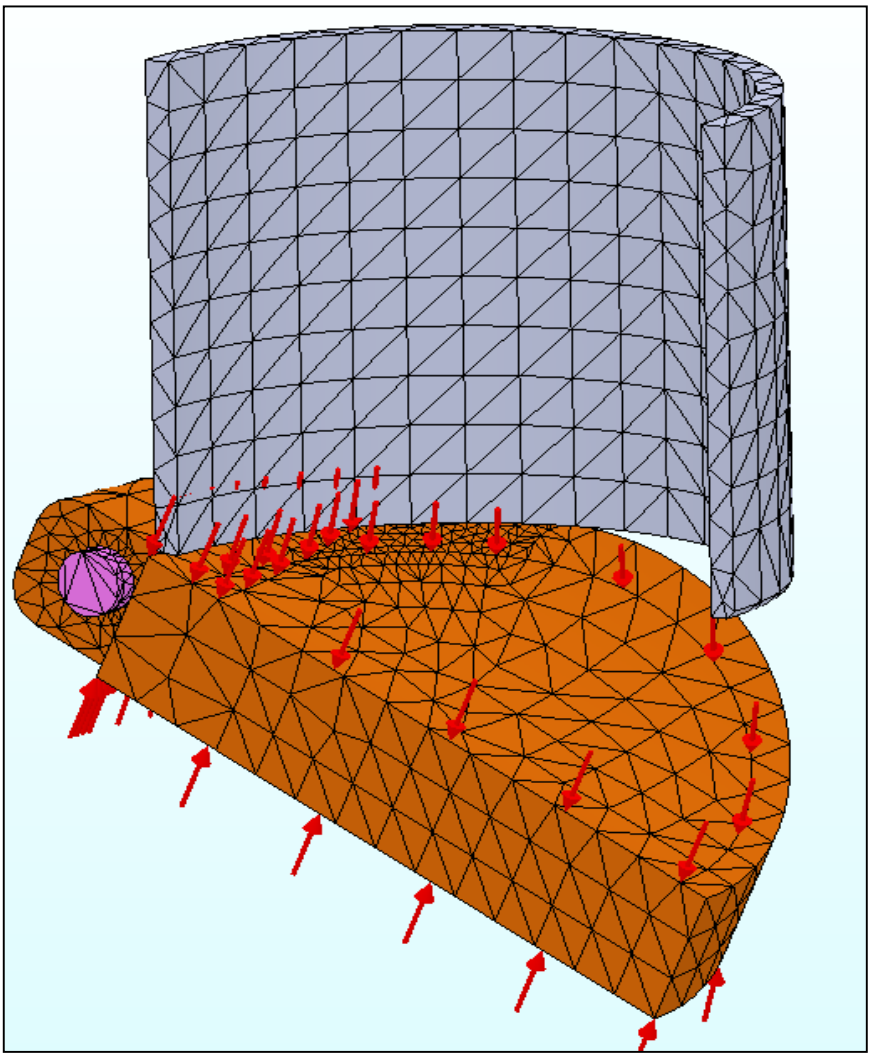

**Figure 6.1 Solid mesh for a flapper SSSV**

Because of the extreme high pressure from the reservoir side, the flapper suffers a high contact force from the sleeve tube to overcome the high fluid pressure, and the fluid pressure surge caused by the sudden closure of the flapper valve. For this study, the flow region diameter is set to be *3.5in*, which is the minimum acceptable value. The typical life span of a SSSV is expected to be *20* years and experience some consistent cycles of loadings.

### 6.2.2 Material Selection

*Inconel* 718 is a precipitation-hardenable nickel-chromium alloy with other amounts of iron and niobium. It is selected for this study because of its wide oil and gas industry acceptance. Its properties are shown in Table 5.5. The cyclic stress-strain curve is defined as in Figure 5.16.

### 6.2.3 LCF Results and Discussion

For LCF, we care more about the equivalent strain, especially the plastic strain. Figure 6.2 shows the equivalent total strain plot of the case when the flapper slam shuts. The maximum stress and strain occurs at the neighborhood of the contact area between the flapper and the sleeve tube. The maximum strain and stress components are listed in Table 6.1.

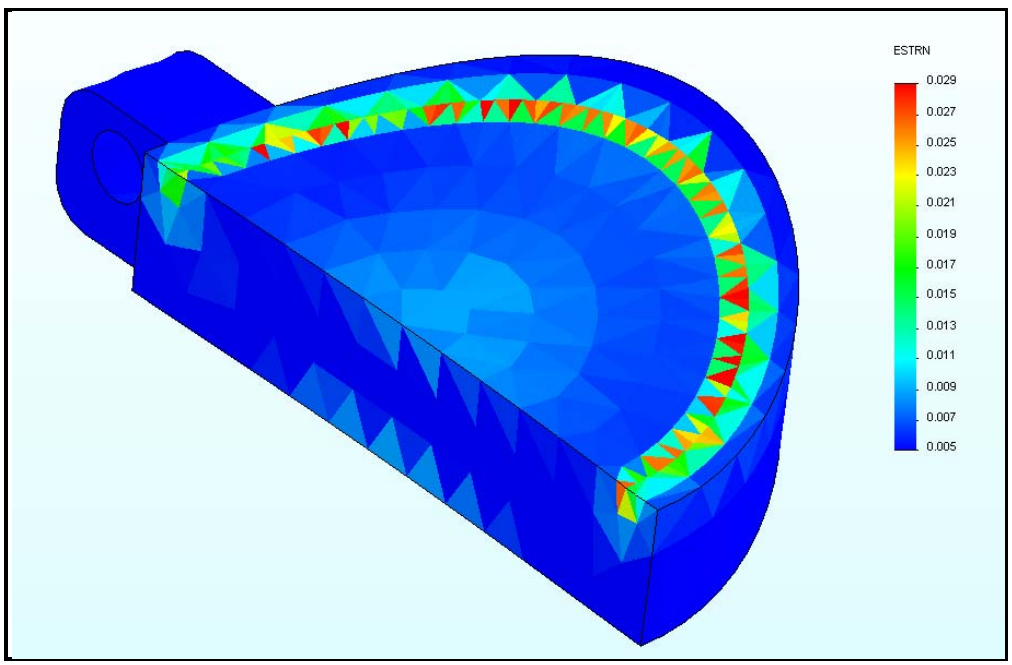


**Figure 6.2 Equivalent Strain and stress of flapper at closure**

| | XX | YY | ZZ | XY | XZ | YZ | Von Mises |
|---|---|---|---|---|---|---|---|
| Strain | 6.94E-03 | -3.16E-02 | 8.98E-03 | 4.88E-03 | 3.07E-04 | 2.02E-02 | 2.90E-02 |
| Stress*(psi)* | -3.00E+04 | -1.78E+05 | -1.20E+04 | 1.99E+02 | 7.98E+03 | 2.21E+04 | 1.61E+05 |

**Table 6.1 Maximum stress and strain during the flapper cyclic loadings**

Figure 6.3 shows the second largest equivalent total strain discovered at the fixed end of the pin when the flapper is *35 degree* open. As the opening degree increases, the contact region move towards the hinge pin.

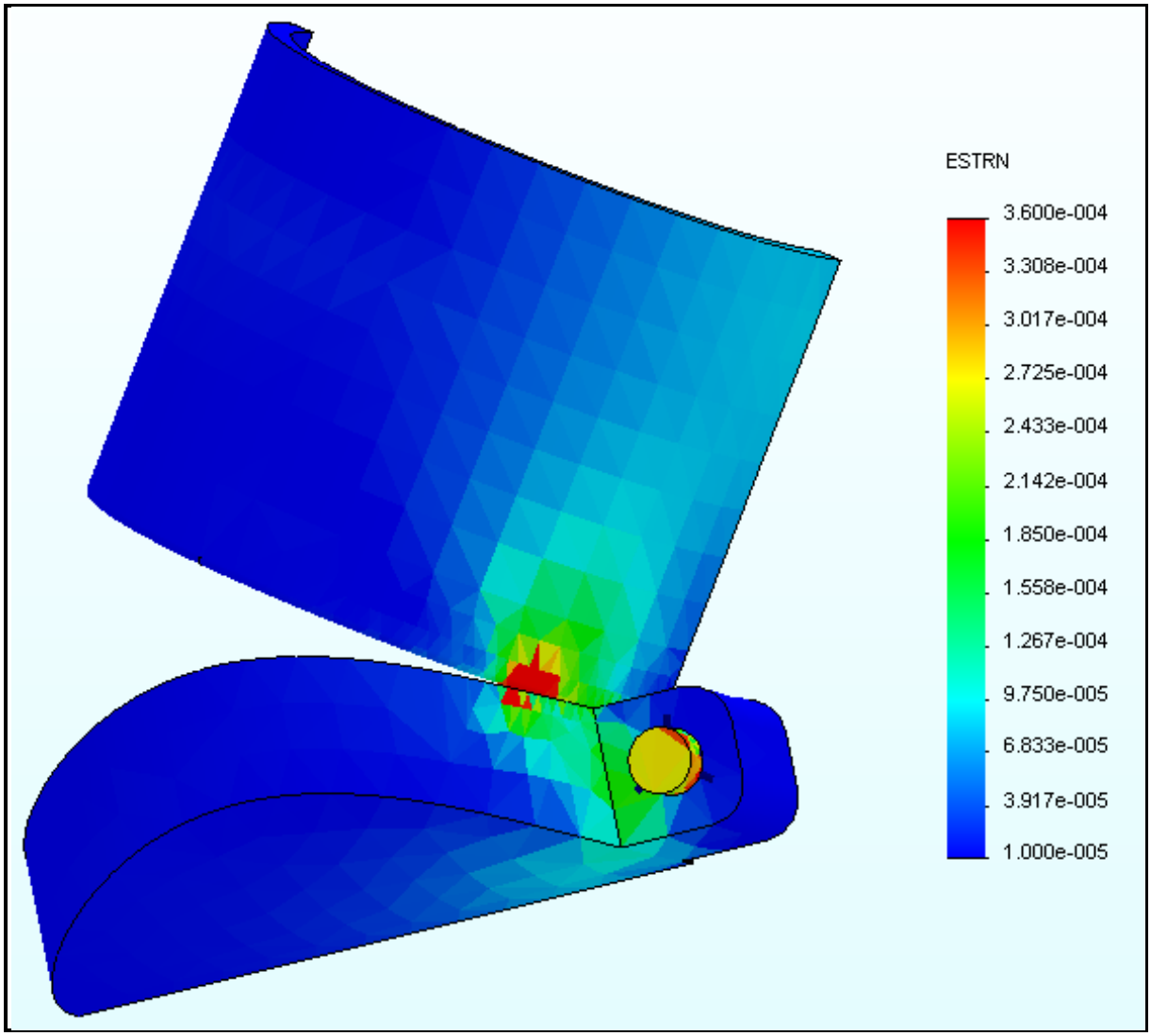


**Figure 6.3 Equivalent Strain of flapper at 35 degree open**

Finally, the maximum equivalent total strain history of the flapper during its rotation is shown in Figure 6.4. The maximum equivalent total strain decreases as the flapper opens and largest strain is about 2.9%.

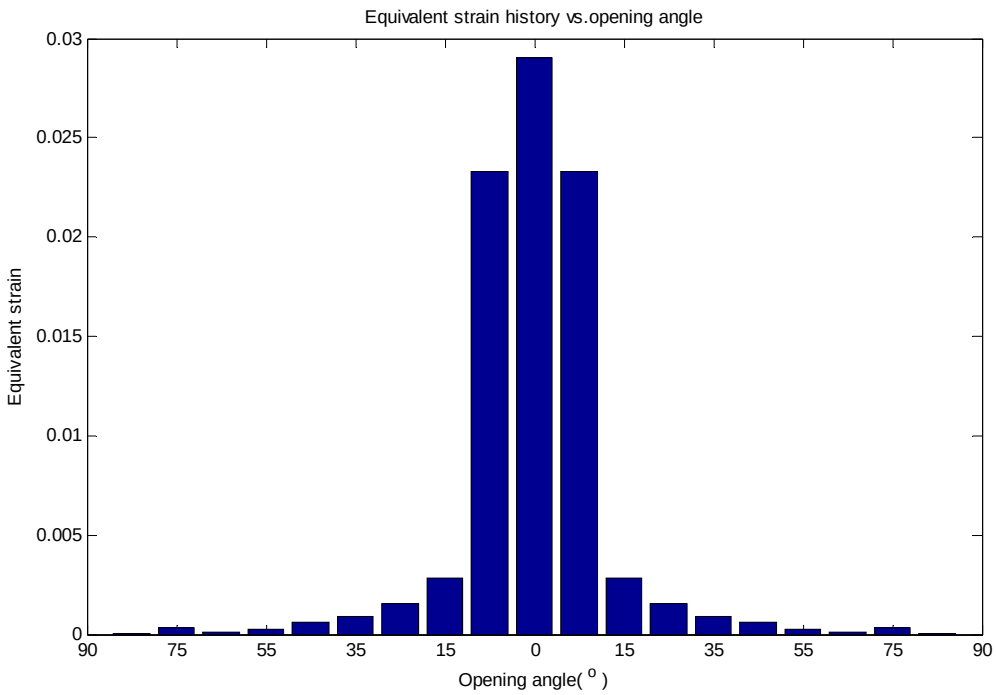


**Figure 6.4 Equivalent strain history of the flapper at various opening angles**

## 6.2.4 LCF Analysis by Continuum Damage Mechanics Model

Continuum damage mechanics (CDM) has been successfully applied in various realms of engineering design. CDM has been accepted as an efficient tool to access various fatigue problems, including steam turbine rotor (Jing 2001), steel structure for earthquake resistant design (Kvinde 2005), human cortical bone fatigue (Taylor 1999), etc. CDM can accurately describe the damage accumulation according to the cyclic plastic strain, which shows a decline of the stress amplitude during the strain loaded cycles.

This study utilizes Lemaitre's continuum damage mechanics model for low cycle fatigue analysis of the flapper valve. The general one-dimensional kinematic damage law is developed by Lemaitre (1992), Lemaitre and Desmorat (2005) follows,

$$\dot{D} = \frac{Y}{S}\dot{p} \cdot H(p - p_D), \dot{p} = \left|\dot{\varepsilon}_p\right|$$

$$\boldsymbol{Y} = \frac{\boldsymbol{\sigma_{eq}^2 R_v}}{\boldsymbol{2E(1-D)^2}} = \frac{\boldsymbol{\sigma^2}}{\boldsymbol{2E(1-D)^2}} \tag{6.1}$$

$$\dot{D} = \frac{\sigma^2}{2E(1-D)^2}\left|\dot{\varepsilon}_p\right|, if\ \varepsilon_p > p_D$$

Where $D$ is the damage variable, which represents the effective surface density of microdefects in the material. $H(p\text{-}p_D)$ is a step function. $Y$ is the strain energy release rate, and $R_v$ is the triaxiality ratio. $S$ is the energy strength of damage as expressed in Eq.6.2,

$$S = \frac{\sigma_y^2}{2E}\left(\frac{\varepsilon_{PR}-\varepsilon_{PD}}{D_C}\right)^{1/p} \tag{6.2}$$

which can be identified from the tensile curve shown in Figure 6.5 (ASM International 2002). The $\varepsilon_{PR}$ and $\varepsilon_{PD}$ terms are estimated in Figure 6.5.

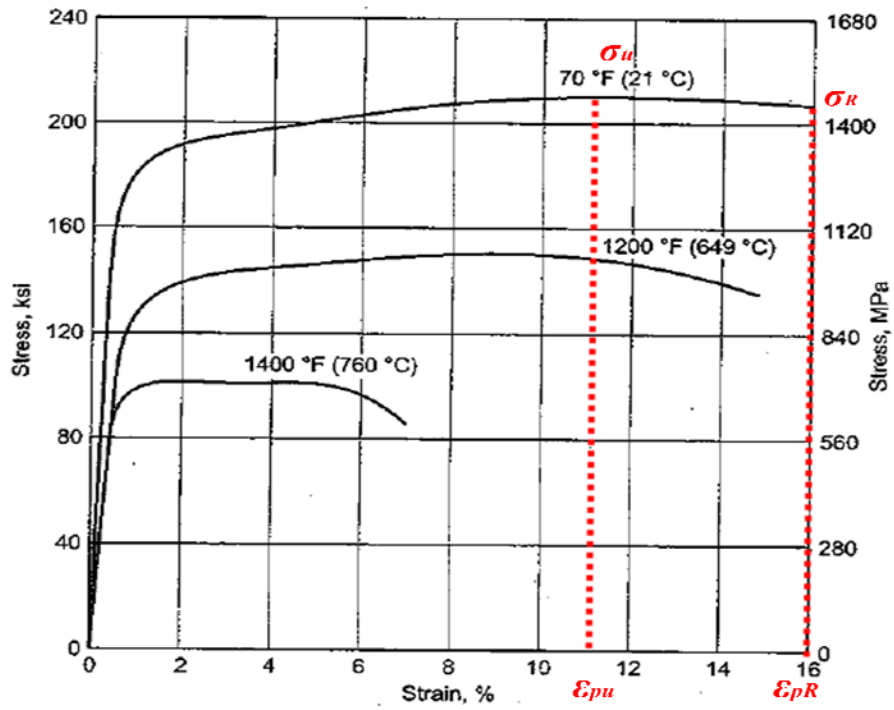


**Figure 6.5 Tensile curve for Inconel 718**

The cycles to low cycle failure, $N_f$, is expressed as in Eq.6.3,

$$N_f = N_o + N_D \tag{6.3}$$

$N_o$ is the number of cycles to reach the damage threshold, $p_D$, for micro-crack nucleation, and $N_D$ is the number of cycles during which the damage occurs. The damage threshold, $p_D$, is obtained from $\varepsilon_{pD}$, the plastic strain, when damage initiates, as shown in Eq. 6.4,

$$p_D = \varepsilon_{pD}\frac{\sigma_u-\sigma_f}{\sigma_{eq}-\sigma_f} \tag{6.4}$$

where $\sigma_u$ is the material ultimate stress, $\sigma_f$ is the fatigue limit stress, corresponding to a number of cycles to failure in a tension compression fatigue test of about $10^6$ to $10^7$. The integration of the kinematic damage law gives us the Manson-Coffin law of low cycle fatigue:

$$N_f = \frac{p_D}{2\Delta\varepsilon_p} + \frac{4ESD_c}{K_p^2}\Delta\varepsilon_p^{-\frac{M+2}{M}} \tag{6.5}$$

Where $D_C$ is the critical damage. The parameters for this study are given in Table 5.5. However, the damage parameters that are not available for *Inconel* 718 are taken from those of aluminum alloy. *(M+2)/M* is the order of *2* for metallic materials, assuming the ductility of *Inconel* 718.

As mentioned in Chapter 2, *ASME Boiler and Pressure Vessel Code (2007)* suggests that numerical elasto-plastic analysis should assume an ideal elastic-perfect-plastic model. Therefore, the stress-strain curve used for LCF is shown in Figure 6.5.

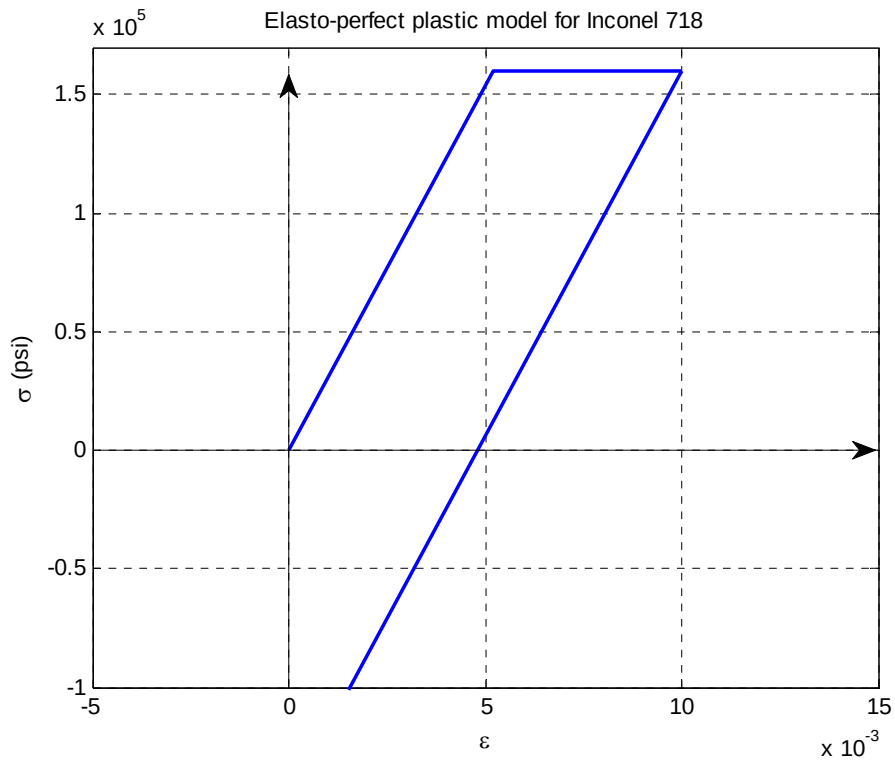


**Figure 6.6 Elasto-perfect plastic model for Inconel 718**

Eq. 6.5 is coded into an open source code DAMAGE90 with a elastic-perfect-plastic model shown in Figure 6.5, which is developed by Lemaitre and is utilized to do the LCF analysis in this study. The maximum equivalent strain discovered from Figure 6.5 is *2.90%*. The input damage parameters for the program are listed in Table 6.2. The maximum stress and strain amplitudes are calculated from Table 6.1.

**Table 6.2 Damage Parameter Inputs**

| Parameters | Definition |
|---|---|
| $S = 9\ MPa$ | Energy strength of damage |
| $\sigma_f = 1100\ MPa$ | Fatigue limit stress |
| $\varepsilon_{pD} = 11\%$ | Damage threshold plastic strain |
| $\varepsilon_{pR} = 21\%$ | Rupture plastic strain |

The results calculated from the CDM model is shown in Figure 6.7 and Figure 6.8.

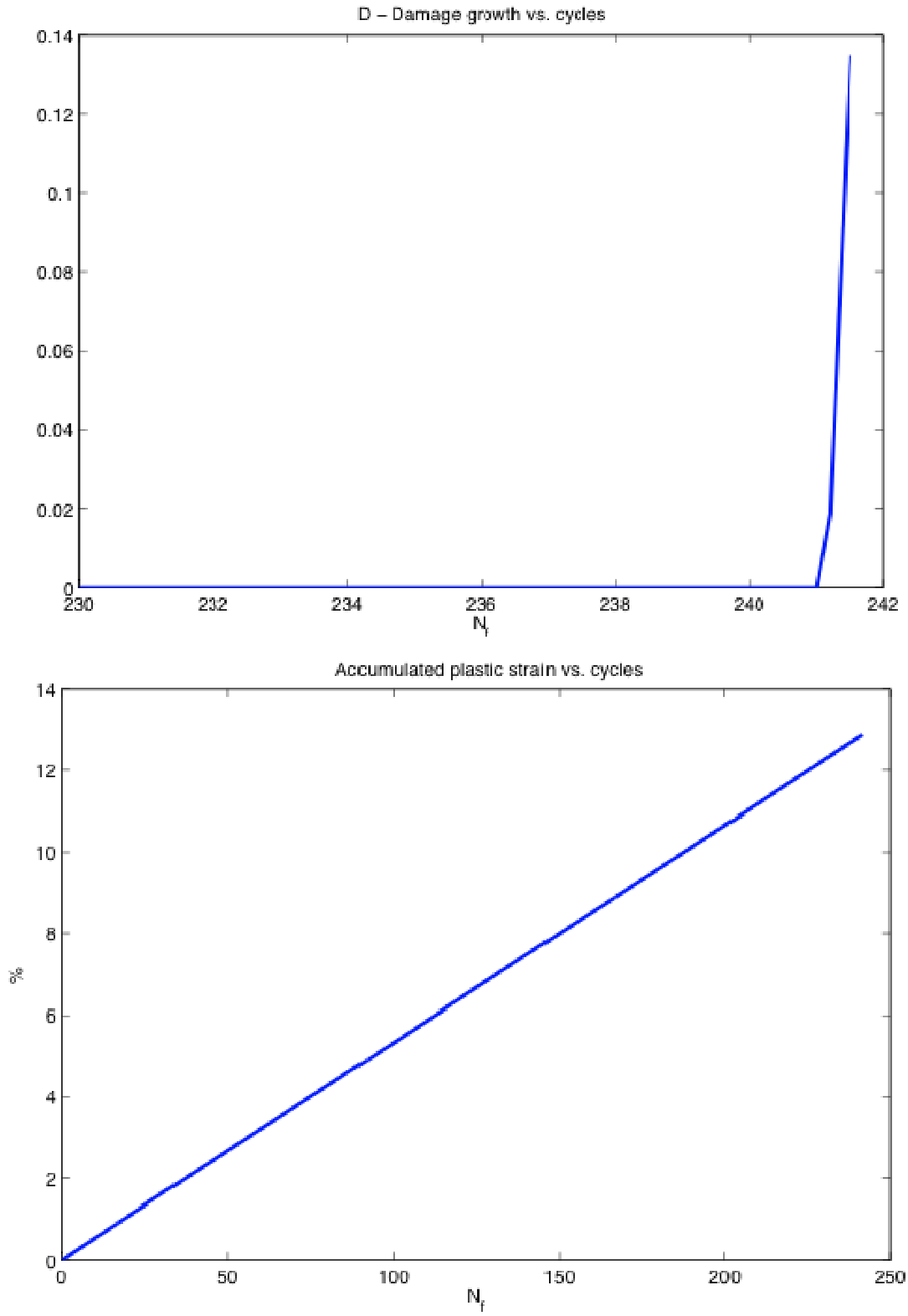


**Figure 6.7 Accumulated plastic strain and damage vs. cycles**

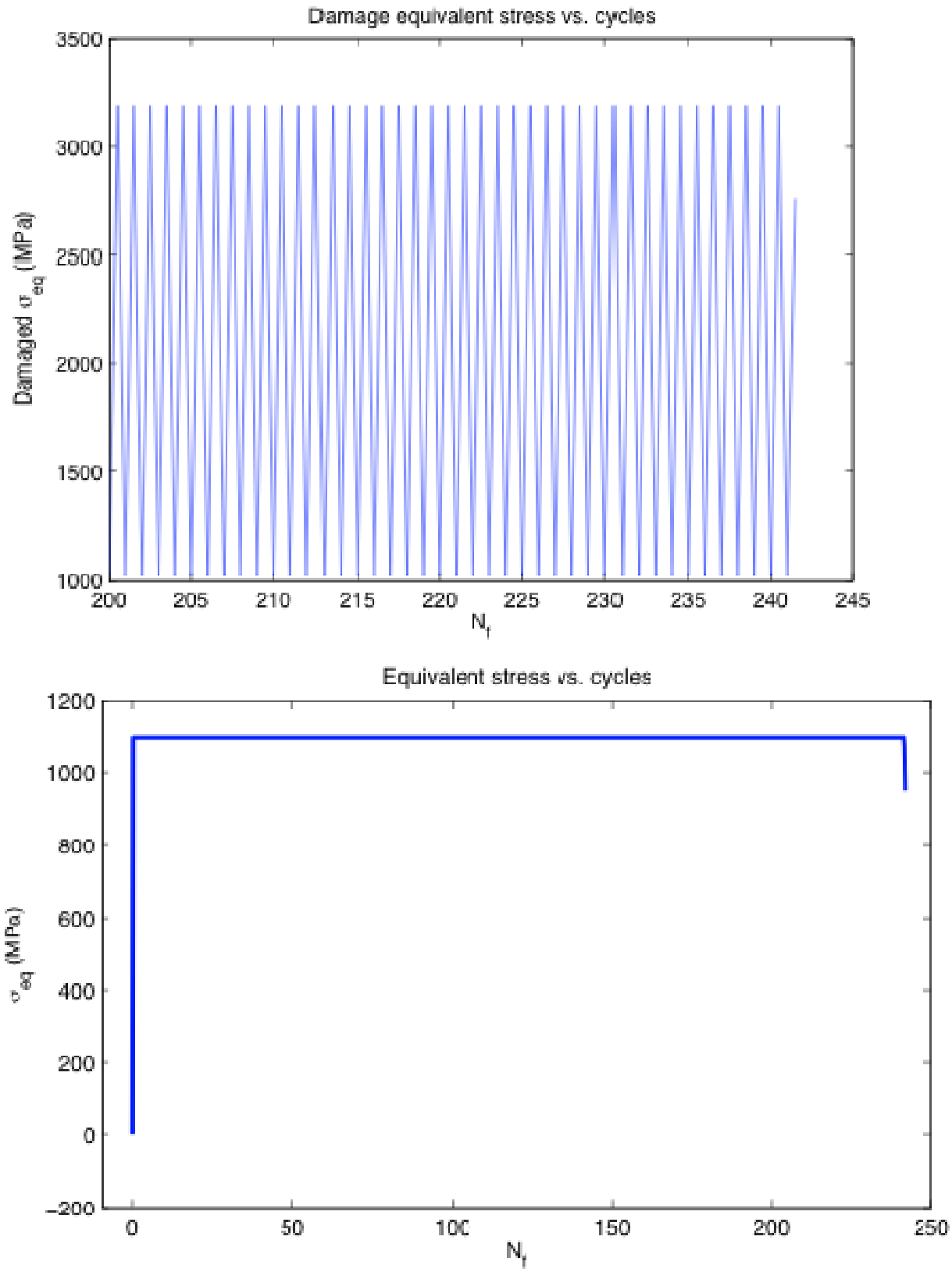


**Figure 6.8 Equivalent and damage equivalent stress vs. cycles**

It is shown in Figure 6.7 that the number of cycles to failure, $N_f$, is estimated to be around 242 cycles, which is higher than the upper design range. The damage and plastic strain accumulation history is obtained. The damage occurs during the last several cycles and causes the ultimate LCF failure.

### 6.2.5 LCF Analysis by Strain-life Fatigue Model

In comparison, the classical strain-life based approach is also applied to estimate the life of the subsurface safety valve (SSSV) in this study. Plastic deformation occurs during the slam-shut of the flapper. Local yielding happens at the neighborhood of the contact area between flapper and the sleeve tube. Therefore, the plastic strain becomes the predominant cause the failure of the design, usually resulting in a shorter life. The strain-life equation (Dowling 1998) is expressed as

$$\boldsymbol{\varepsilon_a = \frac{\sigma_f'}{E}\left(2N_f\right)^b + \varepsilon_f'\left(2N_f\right)^c} \tag{6.6}$$

Where $\varepsilon_a$ is the strain amplitude, for multi-axial stress loadings and $\varepsilon_a$ represents the equivalent strain. The strain-life plot of *Inconel* 718 is shown in Figure 6.9; it is shown that low cycle fatigue is more related to plastic strain, while higher cycle fatigue is more related to elastic strain.

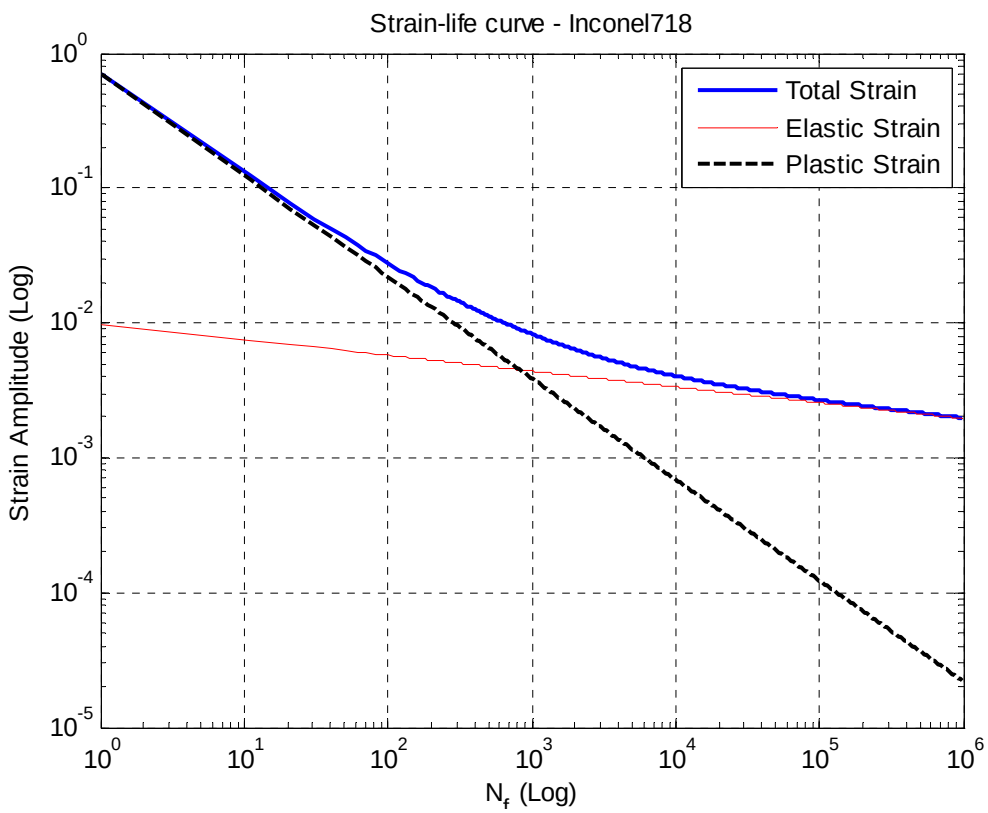

**Figure 6.9 Strain-life curve of Inconel 718**

The material properties list for *Inconel* 718 is found in Table 5.5.

Eq. 6.5 does not consider the mean stress effects. It is shown in Figure 6.4 that cyclic strain history of the flapper has a non-zero mean. The mean stress, $\sigma_m$, should be half of the maximum equivalent stress recorded in this cycle. Therefore, $\sigma_m = 80{,}500\, psi$. Raske and Morrow (1969) has modified the Eq. 6.5 to include the mean stress for complete reversed stress case as follows,

$$\boldsymbol{\varepsilon_a = \frac{\sigma_f'}{E}\left(1 - \frac{\sigma_m}{\sigma_f'}\right)\left(2N_f\right)^b + \varepsilon_f'\left(2N_f\right)^c} \tag{6.7}$$

Another widely used method to consider mean stress effects is the SWT (Smith et al. 1970) model. The SWT model assumes the mean stress depending on the product $\sigma_{max}\varepsilon_a$, where $\sigma_{max} = \sigma_m + \sigma_a$. For the flapper, $\sigma_{max}$ is the maximum stress recorded in a cycle of loadings. The SWT model is as in Eq. 6.7,

$$\boldsymbol{\sigma_{max}\varepsilon_a = \frac{\left(\sigma_f'\right)^2}{E}\left(2N_f\right)^{2b} + \sigma_f'\varepsilon_f'\left(2N_f\right)^{b+c}} \tag{6.8}$$

The results of the strain-life based approaches are listed in Table 6.3.

**Table 6.3 Low Cycle Fatigue Estimates for SSSV**

| Method | Life Span Estimation (Cycles) |
|---|---|
| Continuum damage model (Eq.6.5) | *242* |
| Strain-life (Eq.6.6) | *305* |
| Modified Morrow Approach (Eq.6.7) | *261* |
| SWT approach (Eq. 6.8) | *287* |

From Table 6.1, it is shown that all the approaches implemented result in a life span higher than the design life span requirement of 200. Continuum damage model gives more conservative estimation compared to the life span approaches.

## 6.3 LCF Conclusion and Discussions

(1) In this project, we have presented the low cycle fatigue life estimation of a subsurface safety valve for extreme high pressure and high temperature applications. This part of the work was presented at Material Science and Technology 2010 Conference in Houston. (Gan and Akin 2010). Two LCF models, the continuum damage mechanics approach and the strain-life approaches are utilized and their results are compared. The damage mechanics model gives us a more conservative estimation of the SSSV LCF life span. Several discussions need to be clarified: The FEA stress analysis conducted to define the cyclic strain history does not consider the pressure self-equalizing mechanism, though the strain level obtained will be lower if such a mechanism is considered.

(2) For the damage model, some of the damage parameters for *Inconel* 718 are difficult to obtain. However, in order to complete the analysis, we estimate several parameters based on the known parameters from stainless steel and aluminum alloy. An estimation of the LCF parameter can be derived with the knowledge of all the damage parameters.

(3) It is highly suggested that a LCF process should be added to complete the standards on the design of the components for ultra-deep water applications to prevent failure and increase reliability.

# Chapter 7

# Thermal Stress Analysis

*In this Chapter, the thermal stresses have been analyzed for an opened flapper subsurface safety valve. A temperature study is conducted based on the assumed convection coefficients and fluid temperatures. Then the thermal stresses are obtained from a finite element analysis based on the temperature results.*

## 7.1 Geometry and Assumptions

During the oil production from an extreme high pressure and high temperature reservoir, the SSSV and the pipeline in general experience thermal stresses caused by the high temperature gradient through the radius of the pipe. Considering a reservoir at *30,000 ft* with a temperature of *450°F*, also assuming that the SSSV is installed at *200 ft* below the mud line, the fluid flowing through the SSSV is estimated to have a temperature of *350°F*. However, the temperature outside the pipeline is close to the freezing temperature, *32°F*, of the surrounding fluid and sea water. This large temperature difference causes a thermal effect on the SSSV system.

A typical flapper-shaped subsurface safety valve under consideration is shown in Figure 7.1. The space of the chamber where the flapper resides should be filled as much as possible to prevent unnecessary build-up sludge and other trash. Therefore, a pocket structured chamber is preferred as shown in Figure 7.2.

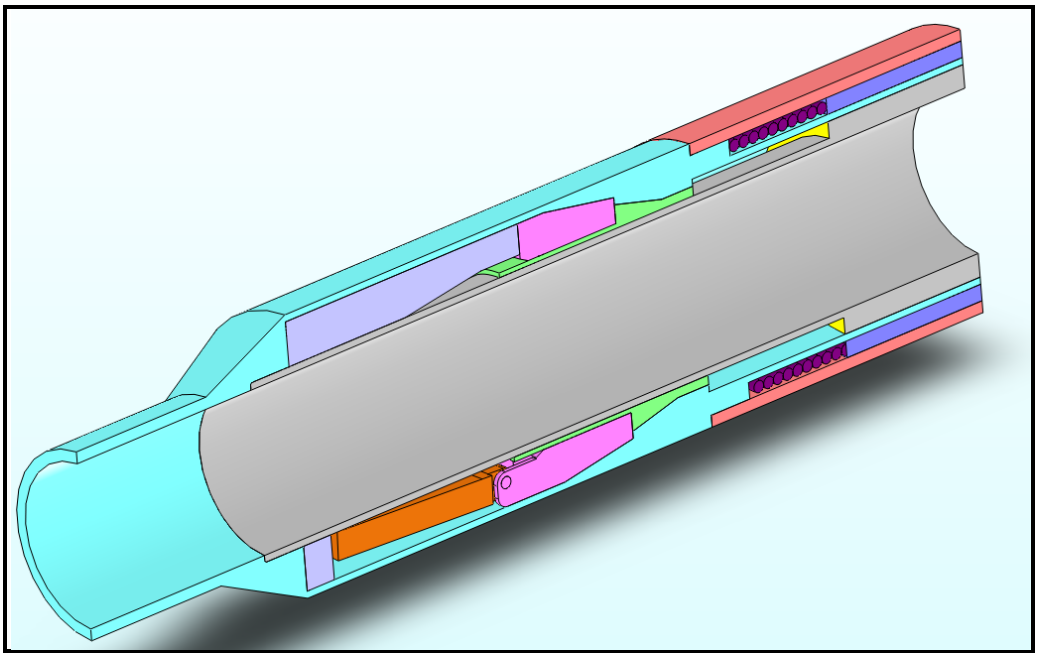

**Figure 7.1 CAD of a flapper SSSV (mid-plane section view)**

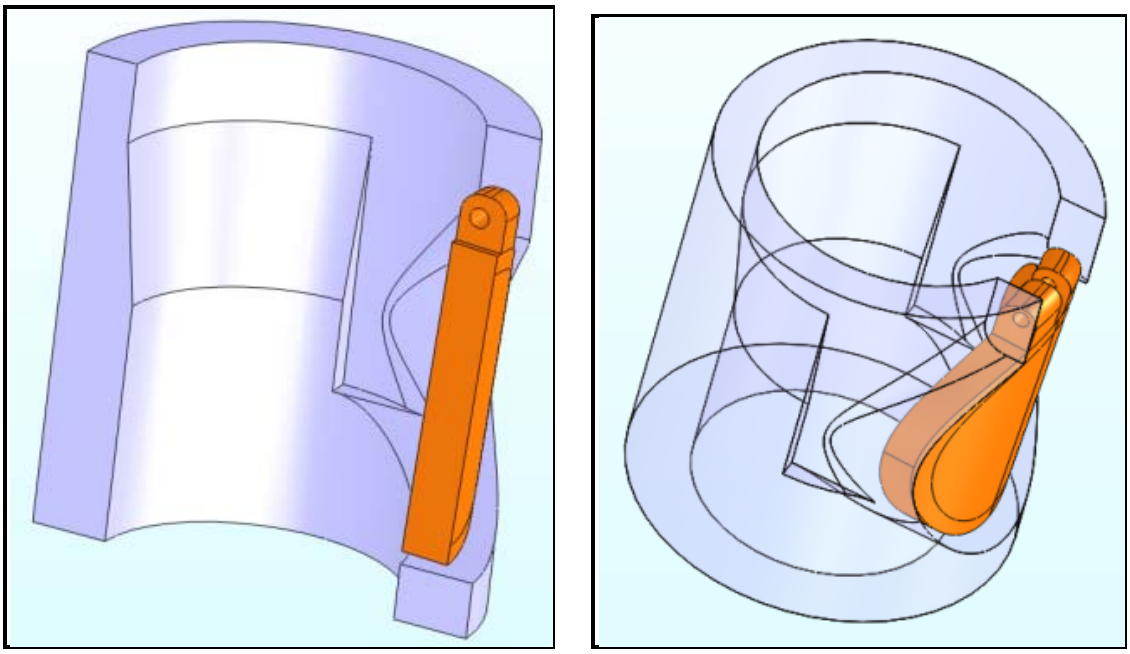

**Figure 7.2 A pocket structured chamber for a flapper valve**

## 7.2 Material Properties and Thermal Boundary Conditions

### 7.2.1 Material

The material used for the study is *Inconel®718*, the thermal properties of the material is listed in Table 7.1.

**Table 7.1 Thermal Properties of Inconel®718**

| Thermal properties of *Inconel®718* | |
|---|---|
| Specific heat | *0.104 Btu/lb.F* |
| Thermal expansion coefficient | *8e-6 / Fahrenheit* |
| Thermal conductivity | *0.000153 Btu/in.s.F* |

### 7.2.2 Boundary Conditions

Two boundary conditions are considered for the thermal stress analysis. The first one is the fluid heat convection on both the inner and outer surfaces of the pipeline. The convection on the inner surface of the pipeline is a forced convection caused by the flowing oil. The average speed of the flowing oil under our assumption is $V_{avg} = 56.53\ ft/s$ as shown in Table 3.3 (Chapter 3). The friction number *f* is about *0.01122*. The convection coefficient of the oil is estimated to be *1,200 W/m*$^2$*.K*. The outer surface of the pipeline is basically assumed to be in the near freezing

sea water; therefore, a nature convection coefficient of *100 W/m²K* is assumed there. They are listed in Table 7.2 below.

**Table 7.2 Average Velocity, Re and Friction Number Estimations**

| Reservoir Depth | Vavg (ft/s) | Friction No. |
|---|---|---|
| *30,000* | *56.53* | *0.01122* |

The second boundary condition is the hydraulic pressure loading of the oil flowing through the pipe. The hydraulic pressure of the flowing oil at the SSSV is obtained from the pipeline hydraulics (*Eq.3.3-3.4 in Chapter 3*). The pipeline diameter, $D = 3.5\ in$. The reservoir is at $z_1 = 30{,}000\ ft$ deep and SSSV is set at $z_2 = 2{,}000\ ft$ deep. Therefore, the height between the reservoir and the SSSV is $L = z_1 - z_2 = 28{,}000\ ft$. The reservoir pressure is denoted as $P_1 = 30{,}000\ psi$ and the estimated hydraulic pressure at the mud line SSSV is obtained as $P_2 = 3{,}450\ psi$.

The analysis is conducted in two steps. First, a finite element analysis of the temperature is conducted and the temperature distribution of the SSSV is obtained. Then the temperature distribution results are used as the temperature inputs with other pressure loadings for the finite element analysis of the stresses. All the contacts are assumed perfectly thermally bonded. The boundary conditions are applied as shown in Figure 7.3. Convection conditions shown in Figure 7.3(a) and Figure 7.3(b) are applied in the temperature study and the pressure loading in Figure 7.3(c) are used in the subsequent stress analysis.

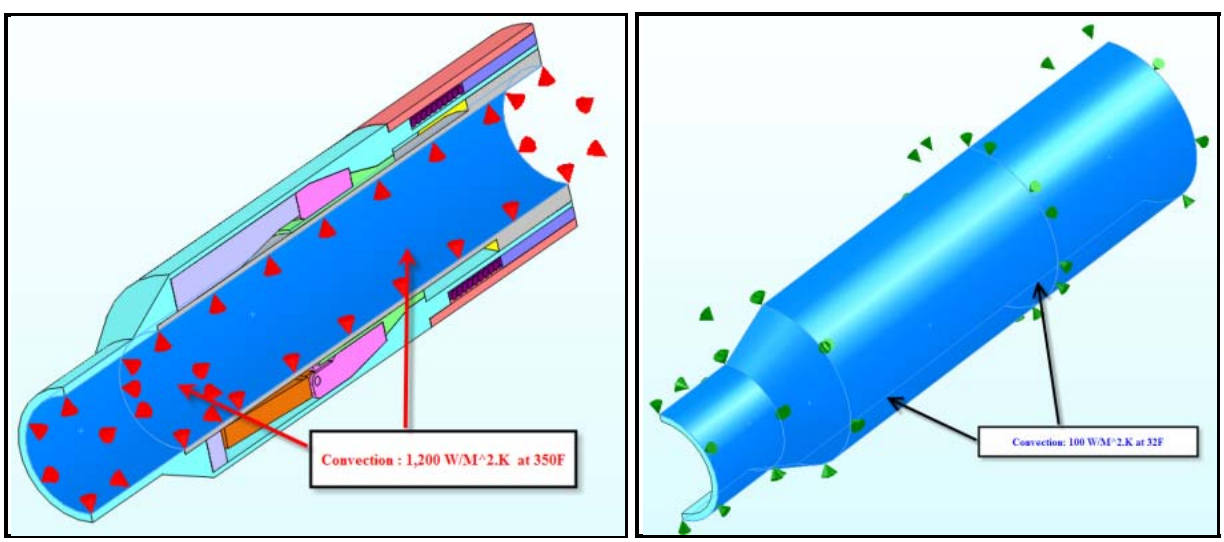


**(a) Inner convection surfaces** **(b) Outer convection surfaces**

**Figure 7.3 Boundary conditions (mid-plane section view)**

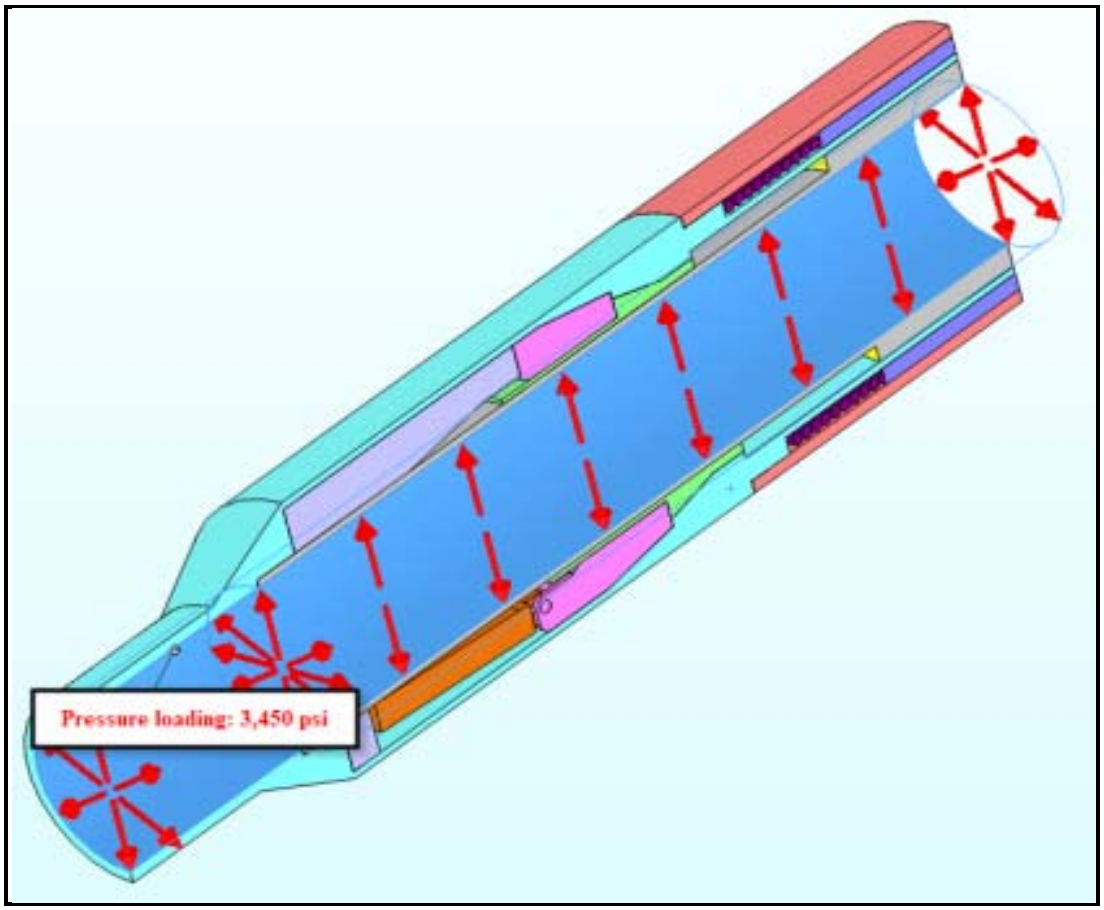


**(c) Hydraulic pressures**

**Figure 7.3 Boundary conditions (mid-plane section view)**

## 7.3 Thermal Results

### 7.3.1 Temperature Results

The temperature contours are shown in Figure 7.4. The temperature of the inner surface is same as the flow temperature *350°F*. That result often implies that the convection coefficient is too high. However, in this case a high convection value maximizes the radial temperature gradient and thus should give conservative thermal stress results. Likewise, replacing bonded interfaces with a thermal resistance will lower the thermal gradient and the related stresses. That is the way that the model should be run for maximum accuracy, but the thermal resistance values would then have to be determined by physical measurement. The temperature at the outer surface is raised to around *57°F,* caused by the heat transferred from the flowing oil inside.

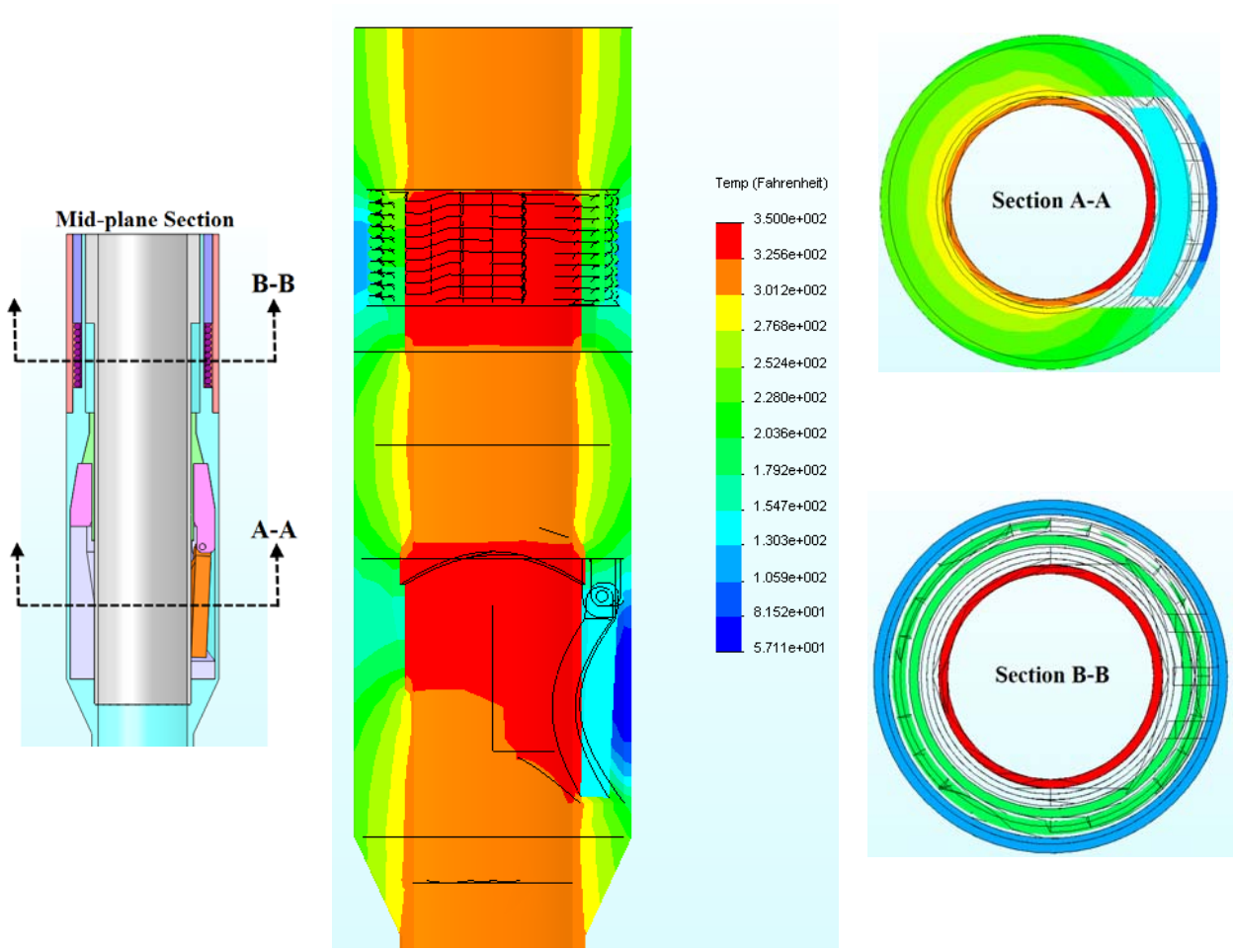


**Figure 7.4 Boundary conditions (mid-plane section view)**

### 7.3.2 Effective Stress Results

The (von Mises) effective stress contour is plotted in Figure 7.5. The maximum stress is on the sleeve tube with a value of *7.84E4* psi, which is way below the yield point of the material (*1.6E5 psi*). Stress level is lower in areas with larger radial thickness. Actually, the pocket structured chamber does not only prevent sludge build-up, but also gives more support to the sleeve tube which lowers the peak stress level on the tube. In Figure 7.6, different pocket structures are compared and their stress results are shown. Figure 7.6(c) shows a pocket structure with least free space for the tube while Figure 7.6(a) gives the most free space for the tube. Figure 7.6(c) shows a lower stress level than in Figure 7.6(a).

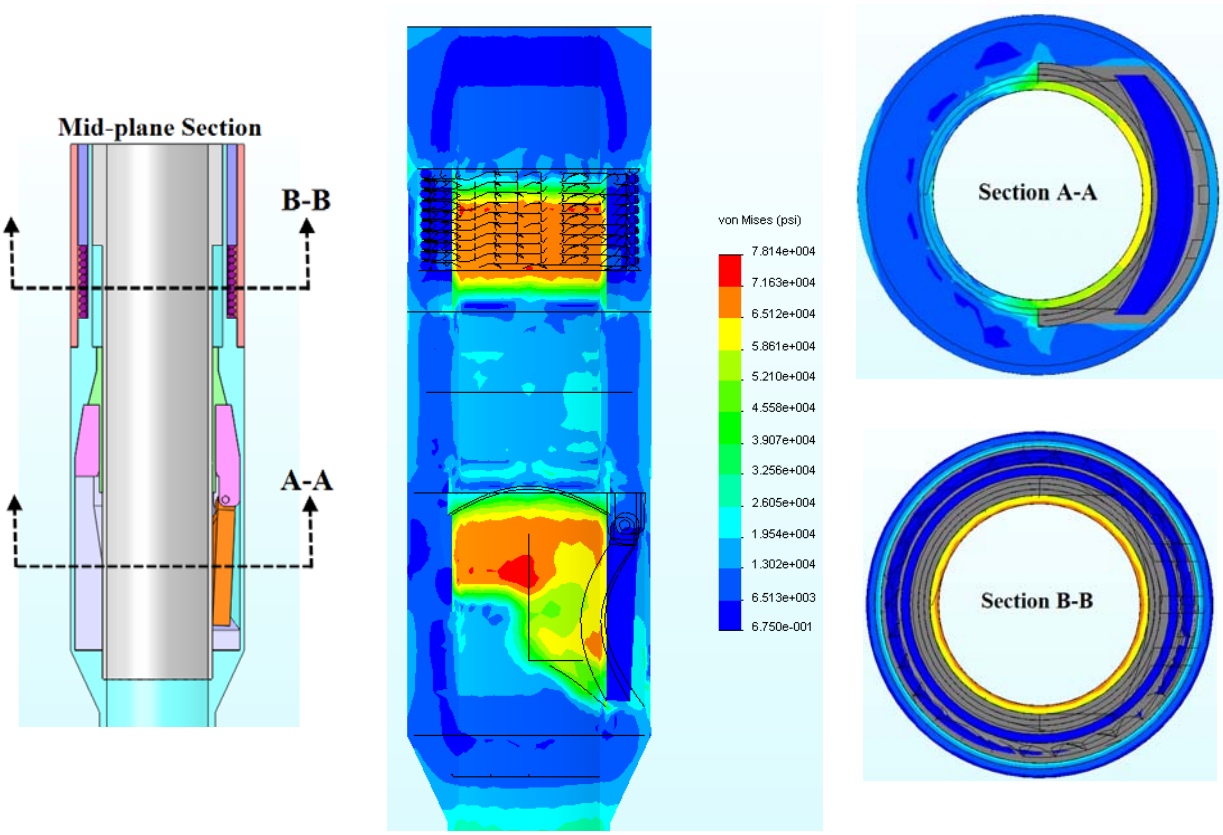


**Figure 7.5 Stress contours of a opened SSSV**

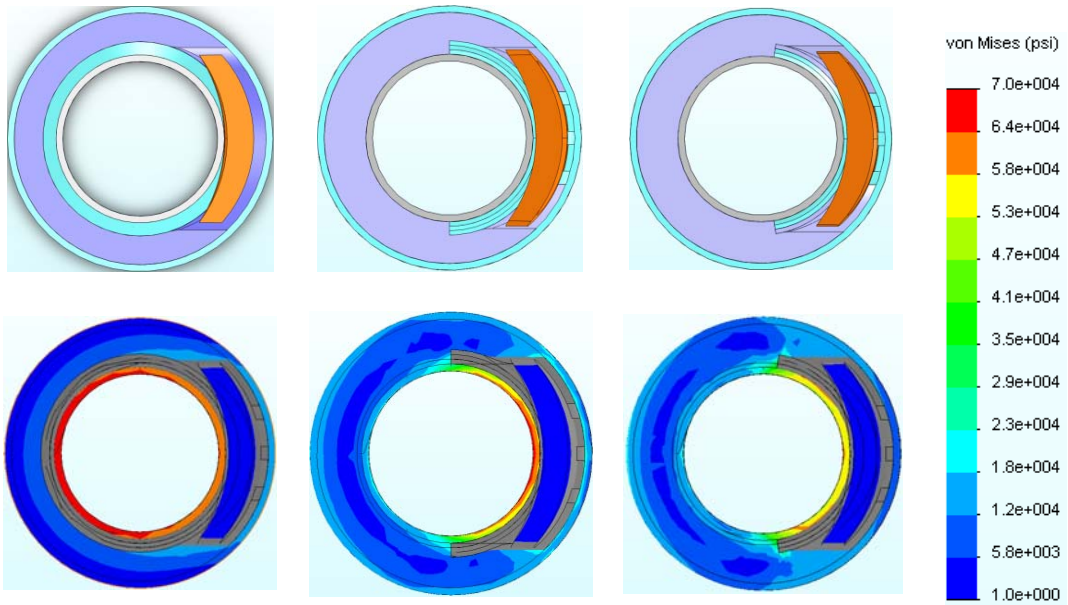


(a) (b) (c)

**Figure 7.6 Stress contours of a opened SSSV with different pocket structures**

## 7.4 Thermal Study Conclusions

The thermal study shows that for XHPHT applications the SSSV system suffers from thermal stresses caused by the high temperature difference between the inner hot flowing oil and the outer near freezing environment. However, the highest effective stress level discovered is much lower than the yield point of the selected material.

Secondly, the chamber where the flapper valve is stored should eliminate free space as much as possible, not only to prevent build-up of the sludge and other trash, but also to give radial support to the sleeve tube to lower stress levels. The flapper valve should be stored in the eccentric side of the pocket structure to minimize the free space for the tube. However, this might leave stringent space for the actuator and hydraulic line installations.

The convection coefficients of the extra high temperature oil are not known. The fluid thermal properties used are from estimation. Likewise, the true thermal resistance values will have to be measured for the expected surface contact pressure.

# Chapter 8

# Study Conclusions and Recommendations

*The project was undertaken, supervised, and sponsored in part by the Research Partnership to the Secure Energy for America (RPSEA) to help the design of the subsurface safety valves for extreme high pressure and high temperature applications. One of RPSEA's main tasks is to facilitate academic efforts to identify and develop new methods and integrated systems for exploring, producing, and transporting-to-market energy or other derivative products from ultra-deepwater natural gas and oil resources.*

This two-year project focused on the new design methods for the subsurface safety valves for extreme high pressure and high temperature applications. Historically, the SSSV is among the subsurface components which have the highest failure rates. An extensive survey has been conducted on the current SSSV technologies and high strength materials (Gan 2009, Martin 2009). The defection of the current industrial standards on SSSV designs has been addressed and possible remedies have been suggested based on ASME BPVC Sect. VIII. Although a robust subsurface safety valve is difficult to design considering the time and cost for this graduate project, a prototype of the flapper valve design is achieved through the parametric study and went through the design process as shown in the Figure 8.1.

It is clear that the design of a SSSV is a complicated fluid structure interacted low cycle fatigue issue. Therefore, incorporating the design guidelines on low cycle fatigue into the current API standards is strongly recommended.

We also faced with several difficulties in this project which prevented us a further study. It has been proven that the critical information on XHPHT fluid properties are difficult to obtain, Information used in this project was supplied by our RPSEA contacts. Secondly, finding high strength material temperature-related properties, especially cyclic stress strain relations, was another difficulty we faced in this project, which prevented us from conducting a further thermal analysis. Thirdly, the full fluid structure interaction could not be performed in this project due to time considerations and lack of software availability. However, based on our study, we provide the following recommendations,

(1) Reference to ASME Boiler and Pressure Vessel Code Sect. VIII for guidelines on elasto-plastic analysis is necessary.

(2) CFD analysis has shown the pressure self-equalizing mechanism can significantly help reopen the flapper valve after slam-shut by reducing 40% - 80% pressure difference.

(3) The parametric study shows that the stress level at slam shut impact can be reduced within the elastic range by a 42% increment of the flapper thickness.

(4) Low cycle fatigue analysis should be included in the design guidelines for safety components such as SSSV.

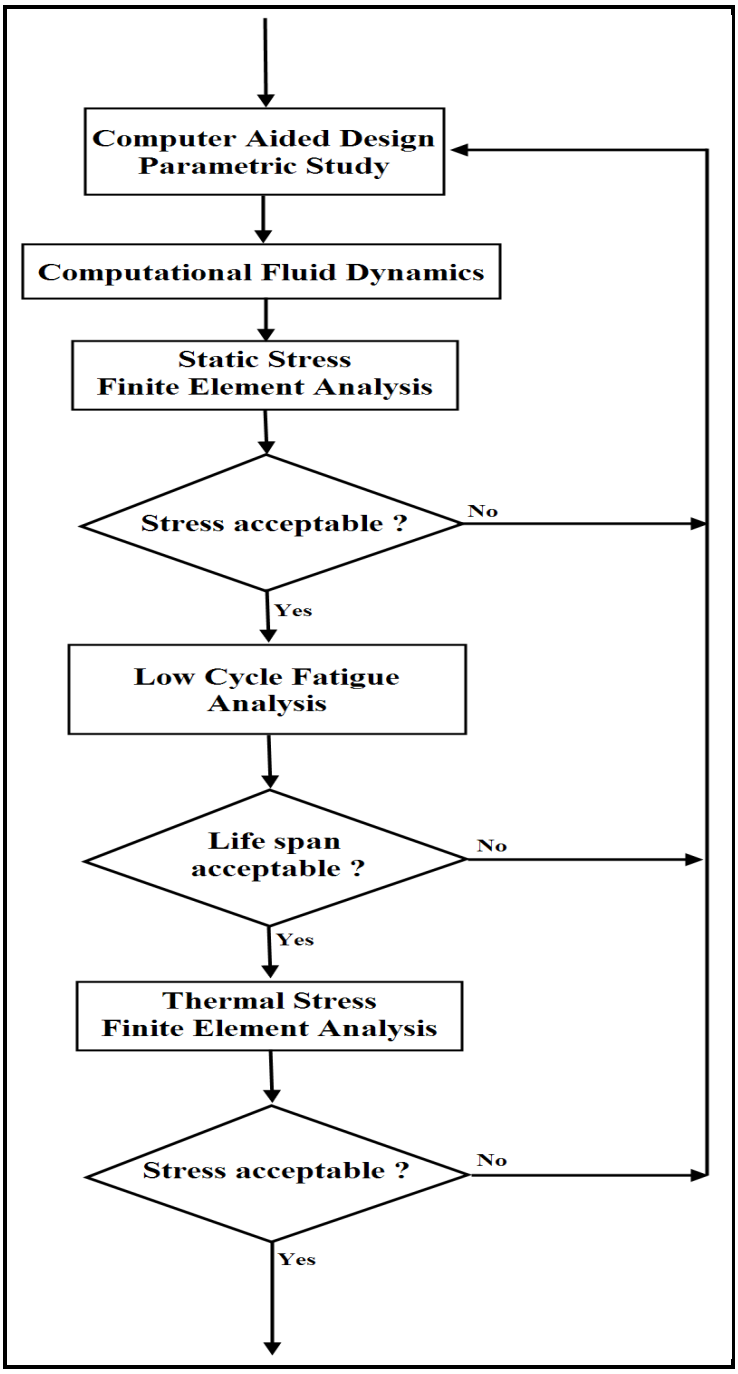


**Figure 8.1 Suggested design-by-analysis process for XHPHT components**

## Closure

This study has validated the concept that it would be practical to design a SSSV for operations at a pressure of 30,000 psi while at a temperature of 400F. Two high strength structural materials have been identified for such a design. However, that conclusion is based on a very narrow set

of fluid and structural properties. It will be critical to vastly increase the range of those critical data. The cyclic stress-strain curve data for the high strength materials will probably be the easiest to obtain or create. The XHPHT reservoir fluid/gas properties will probably be the most difficult design data to obtain. Those data seem to be treated as proprietary to reservoir owner. The interests of public safety suggest that such data should be made public. Hopefully, the SPE, API, or RPSEA organizations can coordinate such an effort.

In addition to this report, two master degree studies of detailed fluid-structure valve interactions have been placed on the RPSEA web site. One study addressed a flapper geometry, while the other dealt with the hemi-wedge geometry. All the electronic input and output from those studys are stored on a computer hard drive physically retained at the RPSEA offices in Sugar Land, TX. A summary of this report will also be submitted for publication as an SPE paper, so as to aid in the transfer of technology.

This study has not specifically addressed how a new design would be experimentally tested for validation. Clearly, the valve should be at least tested at the design pressure and temperature. It is difficult to justify an incremental pressure based on a fixed percentage or a fixed value, as current API standards suggest.

The authors feel that the proper and necessary high pressure valve design procedure should follow the ASME BPVC concept of design-by-analysis (DBA). The concept should be applied to each and every aspect of the design: CFD, water hammer, static stress, fluid-structure-interaction, low cycle fatigue, etc. However, the suggestion to replace proven API standards with using individual reservoir conditions and a DBA is meaningless by itself!

The API should consider setting, or adopting, a standard that defines who is qualified to conduct a proper “analysis” of each and every aspect of the valve design. Usually different experts are be required to certify different design aspects. In the relatively mature area of linear and non-linear stress analysis, commercial software tools are often misused by persons without many years of experience. The authors feel, and have witnessed, that there are numerous examples of computer-aided-negligence. Fortunately, there already exists an international organization, nafems.org, that educates, tests, and certifies individuals as qualified analysts in computational mechanics. That organization supports many areas of knowledge including: static stress analysis, dynamic stress analysis, CFD, heat transfer, fracture mechanics, fatigue, etc. It is strongly recommended that a person conducting any aspect of a SSSV DBA be certified by NAFEMS. Failing that, it is recommended that API set a standard that any DBA must be conducted by a person with at least ten years of experience in the area that they will certify as being a safe design.

# References


[1] Ahmed, T. H. 2006. *Reservoir Engineering Handbook*. 3rd ed. Burlington, MA: Gulf Professional Publishing.

[2] Akin, J. E., 1994. *Finite Elements for Analysis and Design*, London: Academic Press.

[3] Akin, J. E., 2010. *Finite Element Analysis Concepts via SolidWorks*, Singapore: World Scientific Press.

[4] *An International Code 2007 ASME Boiler & Pressure Vessel Code*, Vol. VIII, 2007. New York, New York: American Society of Mechanical Engineers.

[5] Ansys. 2009. *Ansys CFX-Solver Theory Guide, Release 12.0*.

[6] Ansys. 2009. *Ansys Workbench V12.0 Help*.

[7] *API Specification 14A*, 10th ed. 2000. Washington, DC: API.

[8] *API Specification 14A*, 11th ed. 2005. Washington, DC: API.

[9] *API RP 6HP, 1st Edition Draft 5.2.*, 2007. Washington, DC: API.

[10] Arrazola, A. and Maldonado, B. 2006. Ultra Deep HP/HT Completions: Classification, Design Methodologies, and Technical Challenges, *Offshore Technology Conference,* Houston, TX.

[11] *Atlas of stress-strain curves, 2nd ed.,* 2002. ASM International.

[12] Baker Oil Tools, *Onyx Series Safety Valves,* http://www.bakerhughesdirect.com/cgi/hello.cgi/BOT/Knowledgebase/Brochures/BOT-04-7824_Onyx_brochure.pdf. Downloaded November 2009.

[13] Baker Oil Tools, *Ultra Slimline T-Series Safety Valves,* 2001. http://www.bakerhughesdirect.com/cgi/hello.cgi/BOT/Knowledgebase/Brochures/20002737_Slimline-T-Series_brochure.pdf. Downloaded November 2009.

[14] Bergman, D. F. and Sutton, R. P. 2009. A Consistent and Accurate Dead-Oil-Viscosity Method, *SPE Res. Eval. & Eng.* **12**: 815-840. SPE-110194-PA. doi: 10.2118/110194-PA.

[15] Bourgoyne, A. T. Jr., 2002. *Study of Drill String Safety Valves,* Minerals Management Service.

[16] *BP's Tiber Find May Signal Oil Revival in U.S. Gulf of Mexico*, 2009. http://www.bloomberg.com/apps/news?pid=20601087&sid=aNrwOK1CUmMA (accessed 2009).

[17] *Carpenter Aermet 340,* http://cartech.ides.com/datasheet.aspx?i=101&e=338&c=TechArt&FMT=PRINT (accessed 2009).

[18] Cengel, Y. A. and Cimbala, J. M. 2004. *Fluid Mechanics Fundamentals and Applications,* New York: McGraw Hill.

[19] del Coz Díaz, J. J., García Nieto, P. J., Ordieres Mere, J., and Bello García, A., 2007. Computer simulation of the laminar nozzle flow of a non-Newtonian fluid in a rubber extrusion process by the finite volume method and experimental comparison. *J. Non-Cryst. solids* **353**: 981-983.

[20] Dowling, N. E., 1998. *Mechanical behavior of materials: engineering methods for deformation, fracture, and fatigue 2nd ed.*, Upper Saddle River, NJ: Prentice-Hall, Inc..

[21] Gan X. and Akin, J. E., 2010. Low-cycle Fatigue Life Estimation of a Subsurface Safety. *Proc. Failure Analysis and Prevention, Materials Science & Technology Conference*, Houston, Texas.

[22] Gerner, J., Martin, K., McCalvin, D., and McDanniel, D., 2002. At the Ready: Subsurface Safety Valves, *Oilfield Review*: 52-84.

[23] Gusler, W., Pless, M., Maxey, J., Grover, P., Perez, J., Moon, J., and Boaz, T., 2007. A New Extreme-HP/HT Viscometer for New Drilling-Fluid Challenges. *SPE Drill.& Compl.* **22**(2): 81-89. SPE-99009-PA. doi: 10.2118/99009-PA.

[24] *Haynes International, Inc.*, http://www.haynesintl.com/cralloys.htm (accessed 2010).

[25] Houghtalen, R. J. and Hwang, N. H. C. 1996. *Fundamentals of Hydraulic Engineering Systems,* Upper Saddle River, NJ: Prentice Hall.

[26] Jing, J., Sun, Y., Xia, S., and Feng, G., 2001. A continuum damage mechanics model on low cycle fatigue life assessment of stream tubine roto, *International J. Pressure Vessels and Piping* **78**: 59-64.

[27] Kallaur, C. 2001. The Deep Water Gulf of Mexico-Lessons Learned, *Proc. Institute of Petroleum's International Conference on Deepwater Exploration and Production in Association with OGP.*, London, UK.

[28] Kanvinde, A. M. and Deierlein, G. G., 2005. Continuum based micro-models for ultra low cycle fatigue crack initiation in steel structures. *Proc. ASCE Structures Congress and Exposition*.

[29] LeBoeuf, G., Adams, S., Pittman, A., and Dodd, P., 2008. Case History: New Design in Surface-controlled Subsurface Safety Valves Resolves Valve Problems in Subsea Completions in Gulf of Mexico, *Offshore Technology Conference*, Houston, TX. SPE-19620-MS. doi: 10.4043/19620-MS.

[30] Lemaitre, J. 1992. *A course on damage mechanics*, Berlin: Springer-Verlag.

[31] Lemaitre, J. and Desmorat, R., 2005. *Engineering Damage Mechanics* Berlin: Springer, Berlin.

[32] Lester, C. B., 1994. *Hydraulics for Pipeliners*, *2nd ed., Vol. I*, Houston: Gulf Publishing Co..

[33] LMNO Engineering, Research, and Software, Ltd. 2009. *The fluid flow calculations website*, http://www.lmnoeng.com/ (accessed 2009)

[34] *MatWeb*, http://www.matweb.com/ (accessed 2009).

[35] McCrary, M. D., Panzer, D. E., and Pierson, M. O., 2003. Oil and Gas Operations Offshore California: Status, Riskes, and Safety, *Marine Ornithology* **31**: 43-49.

[36] Menter, F. R. 1993. Zonel Two Equation k-omega turbulence Models for Aerodynamics Flows, *AIAA Paper* : 93-2906.

[37] Menter, F. R. 1994. Two-equation Eddy-viscosity Turbulence Models for Engineering Applications, *J. AIAA* **32** (8): 269-289.

[38] Raske, D. and Morrow, J. 1969. Mechanics of materials in low-cycle fatigue testing, *Paper from manual on low-cycle fatigue testing, ASTM* : 1-26.

[39] Schmidt, K. A., 2005. Density and Viscosity behavior of a North Sea Crude Oil, Natural Gas Liquid, and Their Mixtures. *Energy Fuels* **19**(4): 1303–1313.

[40] Sharma, B. E., 1974. Application of the Energy Dissipation Model of Turbulence to the Calculation of Flow Near a Spinning Disc, *Letters in Heat and Mass Transfer* **1**:131-138.

[41] Smith, K. N., Topper, T. H., and Watson, P., 1970. A stress-strain function for the fatigue of metals. *J. of Materials* **5**: 767-778.

[42] Special Metal Corporation *Inconel 718*, http://www.specialmetals.com/documents/Inconel%20alloy%20718.pdf (accessed 2009).

[43] Taylor, M., Verdonschot, N., Huiskes, R., and Zioupos, P. 1999. A combined finite element method and continuum damage mechanics approach to sinulate the in vitro fatigue behaviour of human cortical bone, *J. Materials Science: Materials in Medicine* **10**: 841-846.

[44] Vick, J., Vinzant, M., and Parakka, A. 2005. Unique Safety Valve Design Using a Floating Magnetic Coupler and Metal to Metal Sealing Capability to Provide Step-Change Improvements in Reliability, Safety, and Cost, Offshore Technology Conference, Houston, Texas. SPE-17455-MS. doi: 10.4043/17455-MS.

[45] Vizant, M., Vick, J., and Parakka, A., 2004. A Unique Design for Deep-Set Tubing-Retrievable Safety Valves Increases Their Integrity in Ultra Deepwater Applications, SPE Annual Technical Conference and Exhibition, Houston, Texas. SPE-90721-MS. doi: 10.2118/90721-MS.

[46] Wilcox, D. C. 1988. Re-assessment of the scale-determining equation for advanced turbulence models, *AIAA Journal* **26**: 1299-1310.

# Appendix – Flapper SSSV Prototype Geometry

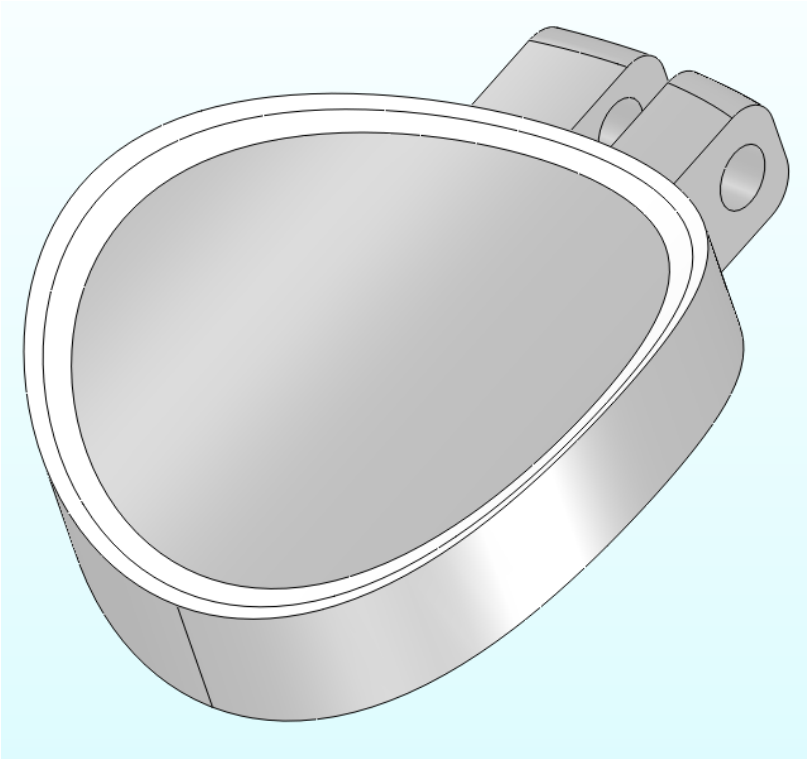

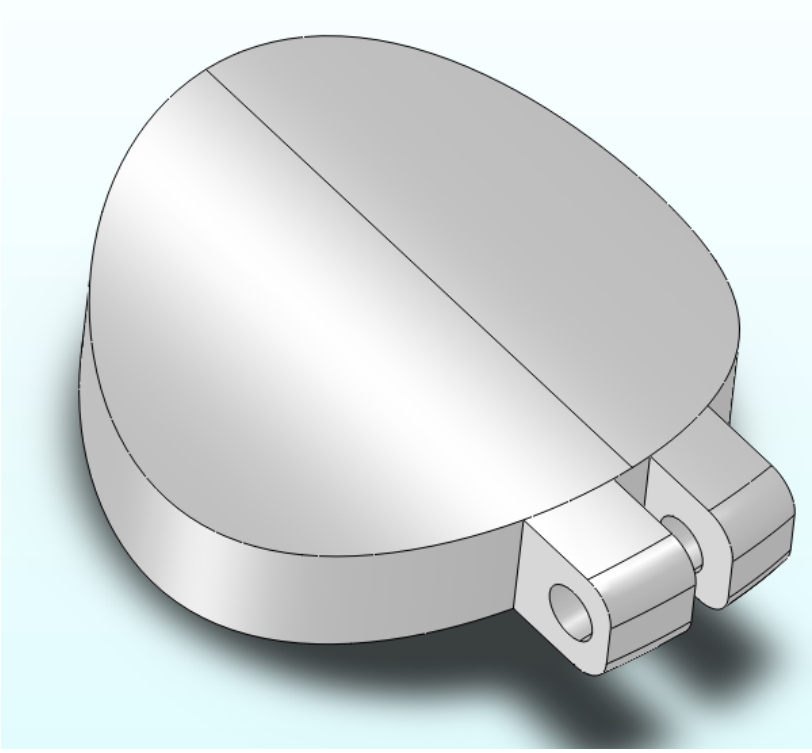

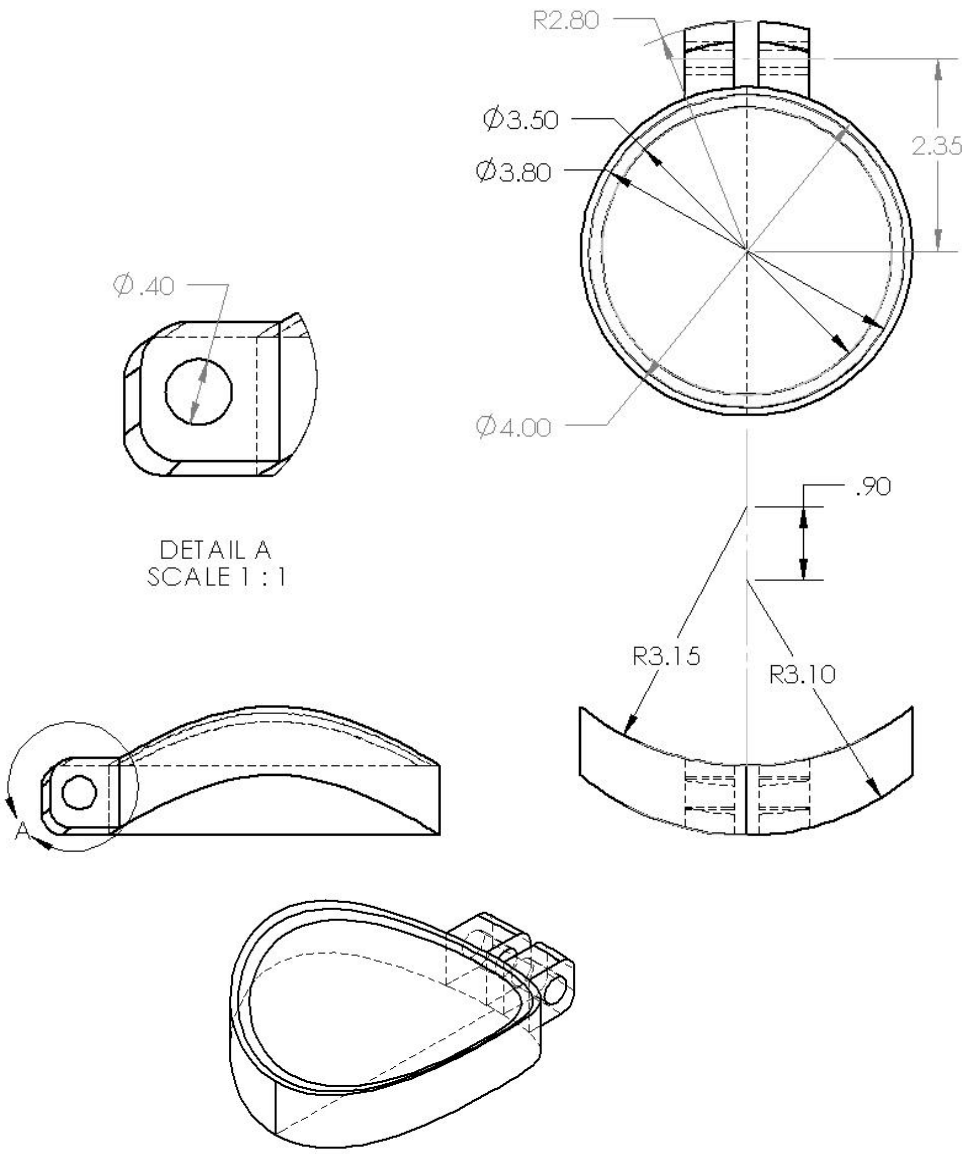


| | | | | NAME | DATE | |
|---|---|---|---|---|---|---|
| | | DIMENSIONS ARE IN **INCHES** | | | | **Appendix A** |
| | | MATERIAL | | | | RPSEA Graduate Project: Design Investigation on Subsurface Safety Valves for Extreme High Pressure and High Temperature Applications |
| NEXT ASSY | USED ON | FINISH | | | | SIZE A · DWG. NO. A flapper SSSV · REV. |
| APPLICATION | | DO NOT SCALE DRAWING | | | | SCALE:1:2 · EIGHT: · SHEET 1 OF 1 |